Institut für Physik
Fachbereich Theoretische Physik

KARL-FRANZENS-UNIVERSITÄT GRAZ
UNIVERSITY OF GRAZ

Dynamical Chiral Symmetry Breaking and Confinement: Its Interrelation and Effects on the Hadron Mass Spectrum

Dissertation
zur Erlangung des akademischen Grades
Doktor der Naturwissenschaften
(Dr. rer. nat.)

Eingereicht von
Mario Schröck

Juni 2013

Betreuer und Gutachter:
Prof. Dr. Christian B. Lang
(Karl-Franzens-Universität)

Zweitgutachter:
Prof. Dr. Mike J. Peardon
(Trinity College Dublin)

Eigenständigkeitserklärung

Hiermit versichere ich, dass ich die vorliegende kumulative Dissertation selbstständig, ohne unerlaubte Hilfe Dritter angefertigt und andere als die in der Dissertation angegebenen Hilfsmittel nicht benutzt habe. Alle Stellen, die wörtlich oder sinngemäß aus veröffentlichten oder unveröffentlichten Schriften entnommen sind, habe ich als solche kenntlich gemacht.

Graz, Juni 2013

Mario Schröck

List of publications this cumulative thesis is based on

This thesis includes the following publications *verbatim*:

- [1] C. B. Lang, Mario Schröck, *"Unbreaking chiral symmetry"*, Phys. Rev. D **84** (2011) 087704 (Chap. 2),
- [2] Mario Schröck, *"The chirally improved quark propagator and restoration of chiral symmetry"*, Phys. Lett. B **711** (2012) 217-224 (Chap. 3),
- [3] L. Ya. Glozman, C. B. Lang, M. Schröck, *"Symmetries of hadrons after unbreaking the chiral symmetry"*, Phys. Rev. D **86** (2012) 014507 (Chap. 4),
- [4] Mario Schröck, Hannes Vogt, *"Coulomb, Landau and maximally Abelian gauge fixing in lattice QCD with multi-GPUs"*, Comp. Phys. Commun. **184** (2013) 1907-1919 (Chap. 5).

Moreover, the underlying work has been presented at various international conferences and the corresponding conference proceedings are the following (not included in this thesis):

- [5] C. B. Lang, Mario Schröck, *"Effects of the low lying Dirac modes on the spectrum of ground state mesons"*, PoS **Lattice2011** (2011) 111,
- [6] L. Ya. Glozman, C. B. Lang, M. Schröck, *"Effects of the low lying Dirac modes on excited hadrons in lattice QCD"*, Acta Phys. Polon. Supp. B **5** (2012) 1001,
- [7] Mario Schröck, Hannes Vogt, *"Gauge fixing using overrelaxation and simulated annealing on GPUs"*, PoS **Lattice2012** (2012) 187,
- [8] Mario Schröck, *"Chiral restoration of the momentum space quark propagator through Dirac low-mode truncation"*, PoS **ConfinementX** (2013) 080,
- [9] L. Ya. Glozman, *"Confinement, chiral symmetry breaking and the mass generation of hadrons"*, Acta Phys. Polon. Supp. B **6** (2013) 245,
- [10] Mario Schröck, Hannes Vogt, *"Gauge fixing in lattice QCD with multi-GPUs"*, to appear in Acta Phys. Polon. Supp. B (2013).

Abstract

Within the framework of this thesis, the interrelation between the two characteristic phenomena of quantum chromodynamics (QCD), i.e., dynamical chiral symmetry breaking and confinement, is investigated. To this end, we apply lattice gauge field theory techniques and adopt a method to artificially restore the dynamically broken chiral symmetry. The low-mode part of the Dirac eigenspectrum is tied to the dynamical breaking of the chiral symmetry according to the Banks–Casher relation. Utilizing two-flavor dynamical lattice gauge field configurations, we construct valence quark propagators that exclude a variable sized part of the low-mode Dirac spectrum, with the aim of using these as an input for meson and baryon interpolating fields. Subsequently, we explore the behavior of ground and excited states of the low-mode truncated hadrons using the variational analysis method. We look for the existence of confined hadron states and extract effective masses where applicable.

The pion is dominated by the Dirac low-mode sector, and as a consequence, we destroy its existence upon removal of that part of the spectrum. On the contrary, all other light isovector mesons, and the nucleon and Delta as representatives of the baryon sector, survive the aforementioned truncation and, moreover, the signals of their exponentially decaying correlator functions improve significantly. An effective mass analysis of the particles allows for the display of the masses as a function of the truncation level. The latter reveals the restoration of the chiral symmetry by means of matching the particle masses of would-be chiral partners. The fact that higher lying hadrons (e.g. the tensor meson b_1 and the Delta baryon) retain a higher mass compared with the other states, strengthens our interpretation that confinement persists in our setup. Surprisingly, the masses of all surviving particles are rather large compared with the naive expectation which is based on the assumption that the dynamical breaking of the chiral symmetry accounts for the main mass contribution in light hadrons.

Moreover, we explore the evolution of the quark wavefunction renormalization function and the renormalization point invariant mass function of the quark propagator in a gauge fixed setting. As expected, vanishing of the dynamically generated mass in the infrared of the mass function is found upon Dirac low-mode removal. Consequently, the mass of the “constituent quarks” of low-mode truncated hadrons cannot account for the rather large hadron masses.

However, we also find infrared suppression of the quark wavefunction renormalization function, which implies that low-momentum quarks are prevented from propagating. Therefore, we conclude that the "constituent quarks" attain higher momenta compared with the full theory and thus the energy of the hadrons increases. This picture is supported by the fact that the lowest Dirac eigenmodes, which we remove from the spectrum, are directly related to the lowest quark momenta.

Motivated by the necessity of fixing the gauge in the aforementioned study of the quark propagator, we developed a flexible high performance code for lattice gauge fixing, accelerated by graphic processing units (GPUs) using NVIDIA® CUDA™ (Compute Unified Device Architecture). Code highlights are a sustained performance of 380 Gflops on the NVIDIA GeForce GTX 580 and linear weak scaling on multiple GPUs.

Lastly, more related but unpublished work on the topic is presented. This includes a study of the locality violation of low-mode truncated Dirac operators, a discussion of the possible extension of the low-mode truncation method to the sea quark sector based on a reweighting scheme, as well as the presentation of an alternative trail to restore the dynamically broken chiral symmetry. The latter is based on the partial removal of the interactions of the quark propagator in its Clifford algebra constituents.

Contents

Chapter 1

Introduction

Quantum chromodynamics (QCD) [11, 12] is widely accepted as the correct theory of the strong nuclear force. The strong nuclear force, or the strong interaction, is one of the four fundamental forces of nature along with the weak nuclear force, the electromagnetic force and the gravitational force. Whereas the long-range electromagnetic and gravitational forces are familiar, it is the weak nuclear force that is responsible for radioactive decays of elementary particles, and the strong nuclear force that binds the neutrons and protons in nuclei to allow the formation of atoms, molecules, and thereby all known matter.

The underlying degrees of freedom of the strong interaction are the quarks and gluons, which carry a so-called color charge. Hence, a quark can either be charged red, blue or green and the anti-quarks anti-red, anti-blue or anti-green respectively. The gluons are the gauge bosons of QCD and transmit the color charge between the quarks.

While gluons are, as opposed to quarks, massless and neutral with respect to electric charge, they are charged with color themselves and they come in an *eightfold way* which arises from the dimension of the underlying gauge group SU(3). The quarks, in contrast, are massive and come in six different *flavors*: up and down, charm and strange, and top and bottom. The flavors differ in their electric charge ($+2/3$ of the elementary charge for the up, charm and top quarks; $-1/3$ of the elementary charge for the down, strange and bottom quarks) and predominantly in their mass values which range from $2 - 3\,\mathrm{MeV/c^2}$ for the up quark to $\sim 171\,\mathrm{GeV/c^2}$ for the heaviest (top) quark.

Although the existence of the quarks, at first primarily introduced as a mathematical tool, has been confirmed by scattering experiments in the 1970s, individual quarks have never been observed in nature. Instead, the spectrum of elementary particles exhibits solely color-neutral states, like the hadrons, which consist of at least either three quarks (a baryon), three anti-quarks

(an anti-baryon), or one quark plus one anti-quark (a meson). In nature, only color-neutral states exist and this is known as *quark confinement*.

Besides confinement, the other characteristic phenomenon of QCD is *chiral symmetry* and its dynamical breaking. On the formal level of the Lagrangian, massless quarks can be classified into two groups: left-handed and right-handed quarks, and the Lagrangian for these can be split into two independent terms. The chiral symmetry is then a set of transformations that can be carried out independently for the two kinds of quarks. The interactions of the quarks with the gluon fields, however, break this symmetry dynamically and generate a non-vanishing chiral condensate $\langle\overline{\psi}\psi\rangle$.

It is yet to be understood to what extent these two phenomena, confinement and dynamical chiral symmetry breaking (DχSB), are interrelated. Can, for example, confinement persist in a world without DχSB? This is one of the questions that will be addressed in this thesis. Moreover, the importance of chiral symmetry breaking for the mass spectrum of light hadrons will be investigated. For example, it is often believed that DχSB accounts for the major part of the mass of the nucleon and the rho meson.

The *asymptotic freedom* of QCD validates the application of perturbative methods in the large momentum regime where interactions become weak. QCD's characteristic features confinement and DχSB, however, are large distance effects and thus cannot be tackled within perturbation theory. Therefore, nonperturbative *ab initio* methods are desirable in order to attack these problems. The most promising such method is lattice gauge field theory, and in particular *lattice QCD* [13] that is our tool of choice. In this context, one replaces the continuous space-time by a finite lattice, which serves as a regulator of the theory. The latter finite theory can then be simulated on a computer and the renormalizability of QCD ensures the independence of the results from the lattice cutoff once the continuum limit is performed a posteriori.

In studies relevant to our work [14, 15, 16, 17], one study [16] used truncations of quark propagators which include or exclude the lowest eigenmodes of the Dirac operator to study the influence of low eigenmodes on light-quark meson correlators. It was found that low eigenmodes make a large contribution to the long-distance part of the pion propagator, but a small contribution to the short-distance part, which is dominated by excited states. The dominance of the low eigenmodes on some meson correlation functions was used in Ref. [18] to improve the signal of correlators by averaging the contribution of the low lying eigenmodes over all positions of the source on the lattice. The author of another study [19] shows that, in Euclidean correlation functions, the zero virtuality modes contribute to effects that spontaneously break chiral symmetry, and only to such effects. Moreover, an explicit construction for correlation functions removing the effects of chiral symmetry breaking is presented. Our work follows the spirit of [16] but the motivation is different: we aim to study the interrelation between DχSB and confinement. To this end, we performed a hadron spectroscopy using correlation

functions that were constructed using Dirac low-mode truncated quark propagators.

The remainder of this work is structured as follows. Firstly, and within this introductory chapter, we briefly describe how to simulate QCD on a finite space-time lattice in order to extract hadron masses (Sec. 1.1). Furthermore, we discuss the properties of the chiral symmetry, and briefly review some definitions of confinement (Secs. 1.2 and 1.3 respectively). In Sec. 1.4, we present the connection of the low lying eigenvalues of the Dirac operator with the dynamical breaking of the chiral symmetry and, based on the latter, explain how we artificially restored the chiral symmetry within this work. The main part of this thesis (Chaps. 2, 3, 4 and 5) comprises of the original published work verbatim on the subject. In each of these chapters, a preface will relate each individual paper to the thesis as a whole. We collect additional unpublished research material on the topic in Chap. 6 and draw conclusions in Chap. 7.

1.1 Quantum chromodynamics on the lattice

In the present section we recall the structure of the continuum QCD Lagrangian, which we subsequently discretize on a finite space-time lattice. Thereafter, we discuss the quantization of QCD in terms of the path integral approach and, related thereto, the calculation of correlation functions on the lattice with Monte Carlo techniques. The discussion of the basics of lattice QCD will be closed by the demonstration of the extraction of hadron masses of ground and excited states from Euclidean correlation functions.

1.1.1 The QCD Lagrangian

Before we discretize QCD, we list the Euclidean continuum Lagrangian of QCD and its gauge symmetries. The QCD Lagrangian is the extension of the analog from quantum electrodynamics (QED) to N_f flavors of fermions, the quarks, and to the non-Abelian gauge group SU(3). For the sake of readability, we adopt a vector notation for the internal Dirac and color structure of the quark fields $\overline{\psi}(x), \psi(x)$ and accordingly a matrix notation for the 4×4 Dirac matrices γ_μ and the 3×3 color matrices $A_\mu(x) = \frac{1}{2} \sum_{i=1}^{8} A_\mu^{(i)}(x) \lambda_i$, which represent the gluon fields. The λ_i are the generators of the group SU(3) in the defining representation, the so-called Gell-Mann matrices. Then, the Lagrangian[1] of QCD reads

$$\mathscr{L}_{\mathrm{QCD}}(x) = \sum_{f=1}^{N_f} \overline{\psi}^{(f)}(x) \left(\gamma_\mu D_\mu(x) + m^{(f)} \right) \psi^{(f)}(x) + \frac{1}{2g^2} \operatorname{tr} \left[F_{\mu\nu}(x) F_{\mu\nu}(x) \right] . \tag{1.1}$$

1 We make use of the common practice to call $\mathscr{L}$ the Lagrangian, which is strictly speaking the Lagrangian density.

Here g denotes the gauge coupling and we introduced the covariant derivative

$$D_\mu(x) = \partial_\mu + iA_\mu(x)\,, \tag{1.2}$$

as well as the field strength tensor

$$F_{\mu\nu}(x) = -i\,[D_\mu(x), D_\nu(x)] = \partial_\mu A_\nu(x) - \partial_\nu A_\mu(x) + i\,[A_\mu(x), A_\nu(x)]\,. \tag{1.3}$$

The QCD Lagrangian is invariant under the following set of local gauge transformations of the fermion fields, let $g(x) \in \mathrm{SU}(3)$ for all x,

$$\overline{\psi}(x) \to \overline{\psi}'(x) = \overline{\psi}(x)g(x)^\dagger\,, \tag{1.4}$$

$$\psi(x) \to \psi'(x) = g(x)\psi(x)\,. \tag{1.5}$$

Furthermore, by construction, invariance is guaranteed for the following transformations that affect the gauge fields:

$$D_\mu(x) \to D'_\mu(x) = g(x)D_\mu(x)g(x)^\dagger\,, \tag{1.6}$$

$$F_{\mu\nu}(x) \to F'_{\mu\nu}(x) = g(x)F_{\mu\nu}(x)g(x)^\dagger\,. \tag{1.7}$$

1.1.2 Discretizing the QCD Lagrangian

In order to discretize QCD, we start off by replacing the continuous four dimensional space-time with a discrete lattice Λ of size $N_1 \times N_2 \times N_3 \times N_4 \equiv N_s^3 \times N_t$,

$$\Lambda = \{n \equiv (n_1, \ldots, n_4)\,|\,n_\mu = 0, \ldots, N_\mu - 1\}\,, \tag{1.8}$$

with periodic boundary conditions[1] and an isotropic lattice spacing a, such that the continuum coordinate x_μ is related to the dimensionless lattice coordinate n_μ via $x_\mu = an_\mu$.

Next, we consider the free fermionic part of the Lagrangian Eq. (1.1) for a single flavor (the generalization to N_f flavors is straightforward),

$$\mathscr{L}_F(x) = \overline{\psi}(x)\,(\gamma_\mu\partial_\mu + m)\,\psi(x)\,. \tag{1.9}$$

We substitute the partial derivative ∂_μ with the central finite difference discretization, which

1 To obtain the correct reconstruction of the Hilbert space for the Minkowskian theory, one imposes anti-periodic temporal boundary conditions for the fermions.

then yields

$$\mathscr{L}_F(n) = \overline{\psi}(n) \left(\sum_\mu \gamma_\mu \frac{\psi(n+\hat{\mu}) - \psi(n-\hat{\mu})}{2a} + m\,\psi(n) \right) , \tag{1.10}$$

where $n+\hat{\mu}$ and $n-\hat{\mu}$ denote the neighbor sites of n in positive and negative μ-direction, respectively. Eq. (1.10) can be rewritten as the bilinear form

$$\mathscr{L}_F(n) = \sum_{m\in\Lambda} \overline{\psi}(n)\, D(n,m)\, \psi(m) , \tag{1.11}$$

where the sum runs over all lattice sites m and D is the free naive lattice Dirac operator,

$$D(n,m) = \sum_\mu \gamma_\mu \frac{\delta_{m,n+\hat{\mu}} - \delta_{m,n-\hat{\mu}}}{2a} + m , \tag{1.12}$$

which is trivial in color space. The inverse of the massless naive Dirac operator in momentum space, i.e., the massless naive quark propagator, has not only a pole at $p = (0,0,0,0)$, like in the continuum, but has additional poles whenever all d components of p are either equal to zero or equal to π/a. Thus, the naive Dirac operator generates $2^d - 1$ unphysical fermions, the so-called *doublers*.

Nielsen and Ninomiya derived a no-go theorem [20, 21, 22], based on topology arguments, which states that it is impossible to have a (naively) chirally invariant, doubler-free, local and translational invariant discretization of fermions on the lattice.

Wilson suggested to remove the doublers by adding a term proportional to the inverse lattice spacing that assigns an additional mass to the unphysical doublers and ensures that these decouple from the theory in the continuum limit. The Wilson term, though, breaks chiral symmetry at finite lattice spacing explicitly. We will discuss chiral symmetry in Sec. 1.2 in more detail and then see how the Ginsparg–Wilson equation leads to a way out of this seeming dilemma.

For now we stick with the naive Dirac operator and proceed by implementing the most fundamental symmetry of gauge theories, the local gauge symmetry. We require the discretized Lagrangian to be in analog to its continuum counterpart invariant under local gauge transformations of the form (1.4) and (1.5). It is easy to see that the mass term of the free fermion Lagrangian (1.9) is trivially invariant under that set of transformations. Consequently, we require the terms of the central finite difference, i.e, $\overline{\psi}(n)\,\psi(n\pm\hat{\mu})$, to be invariant under (1.4) and (1.5), as well. Following the same line of arguments as in the continuum, one can achieve invariance by introducing an oriented field $U_{\pm\mu}(n) \in \mathrm{SU}(3)$ that transforms under gauge transformations according to

$$U_{\pm\mu}(n) \to g(n)\, U_{\pm\mu}(n)\, g(n\pm\hat{\mu})^\dagger . \tag{1.13}$$

Therewith, we dress the naive Dirac operator (1.12), such that

$$D(n,m) = \sum_{\mu} \gamma_\mu \frac{U_\mu(n)\,\delta_{m,n+\hat{\mu}} - U_{-\mu}(n)\,\delta_{m,n-\hat{\mu}}}{2a} + m\,. \tag{1.14}$$

Now it is straightforward to show that the first part of the kinetic term of (1.14) is, as required, invariant under local gauge transformations:

$$\begin{aligned} \overline{\psi}(n)\,U_\mu(n)\,\psi(n+\hat{\mu}) \;&\longrightarrow \overline{\psi}(n)\,g(n)^\dagger\,g(n)\,U_\mu(n)\,g(n+\hat{\mu})^\dagger\,g(n+\hat{\mu})\,\psi(n+\hat{\mu}) \\ &= \overline{\psi}(n)\,U_\mu(n)\,\psi(n+\hat{\mu}) \end{aligned} \tag{1.15}$$

and, equivalently, the second part,

$$\begin{aligned} \overline{\psi}(n)\,U_{-\mu}(n)\,\psi(n-\hat{\mu}) \;&\longrightarrow \overline{\psi}(n)\,g(n)^\dagger\,g(n)\,U_{-\mu}(n)\,g(n-\hat{\mu})^\dagger\,g(n-\hat{\mu})\,\psi(n-\hat{\mu}) \\ &= \overline{\psi}(n)\,U_{-\mu}(n)\,\psi(n-\hat{\mu})\,. \end{aligned} \tag{1.16}$$

The field $U_\mu(n)$ links neighboring lattice sites n and $n \pm \hat{\mu}$, therefore, the $U_\mu(n)$ are often referred to as link variables. Inverting the left hand side of (1.16) and subsequently shifting all sites $n \to n + \hat{\mu}$ yields

$$U_{-\mu}(n) = U_\mu(n-\hat{\mu})^{-1} = U_\mu(n-\hat{\mu})^\dagger\,. \tag{1.17}$$

Thus, the link variable in negative μ-direction is equal to the inverse link variable from the site $n - \hat{\mu}$ in positive μ-direction, see also Fig. 1.1.

Figure 1.1: Link variables in positive and negative μ-direction.

Using the fact that path ordered continuum gauge transporters reveal the same gauge transformation properties as the link variables that we have just introduced, one can interpret the link variables as a lattice version of the gauge transporter connecting two neighboring lattice sites. This connection allows to relate the link variables to the continuum gauge fields,[1]

$$U_\mu(n) = \mathrm{e}^{iaA_\mu(n)}\,. \tag{1.18}$$

1 Be aware that we implicitly rescaled the continuum gauge fields $gA_\mu \to A_\mu$ to obtain the inverse coupling prefactor of the gauge part in the Lagrangian (1.1).

Here it becomes obvious that, while the continuum gauge fields A_μ are elements of the algebra su(3), the link variables are elements of the corresponding group SU(3).

By expanding Eq. (1.18) in powers of the lattice spacing, it is possible to show that the naive lattice Dirac operator (1.14) (as well as the Wilson Dirac operator) agrees with its continuum counterpart up to order $\mathcal{O}(a)$. The Symanzik improvement program [23], however, offers a systematic way to reduce the errors of the fermionic Lagrangian to $\mathcal{O}(a^2)$. To this end, all terms that have the correct dimensionality and the symmetries of the QCD fermionic Lagrangian must be included. This procedure will be discussed in more detail in Sec. 3.3.6.

To complete the discretization of QCD, it remains to find a term that describes the pure gauge part of the Lagrangian. Naturally, we seek again a local expression that is invariant under local gauge transformations. Moreover, it is easy to see that the trace over a closed loop of link variables transforms trivially under gauge transformations due to the cyclic permutation property of the trace. The shortest such closed loop is the so-called plaquette, which is defined as

$$U_{\mu\nu}(n) = U_\mu(n)\, U_\nu(n+\hat{\mu})\, U_\mu(n+\hat{\nu})^\dagger\, U_\nu(n)^\dagger, \tag{1.19}$$

where we used identity (1.17) to convert the links in negative $\hat{\mu}, \hat{\nu}$ direction. See Fig. 1.2 for an illustration of the plaquette.

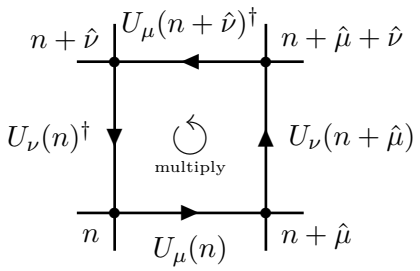

Figure 1.2: The gauge plaquette: the smallest closed loop of gauge links.

The simplest possible gauge Lagrangian, called after Wilson [13], is then constructed by summing locally over all six plaquettes in the four dimensions:

$$\mathscr{L}_G(n) = \frac{1}{3}\beta \sum_{\mu<\nu} \mathfrak{Re}\ \mathrm{tr}\left[\mathbb{1} - U_{\mu\nu}(n)\right]. \tag{1.20}$$

Here, $\beta = 6/g^2$ is the commonly used abbreviation for the inverse coupling. Wilson's gauge term approximates the continuum equivalent up to order $\mathcal{O}(a^2)$ and, similarly to the fermionic part of the Lagrangian, one can systematically improve the order of the errors [23, 24].

1.1.3 Simulating QCD

So far, our discussion of QCD omitted the fact that we target at describing a quantum theory. In the following discussion, which is partially based on [25, 26], we quantize the discrete theory and show how Euclidean correlation functions can be approximated by lattice Monte Carlo simulations. From the Lagrangian density, we can derive the classical equations of motion (Euler–Lagrange) whose solutions minimize the action. The action is a functional of the fields and given by the integral of the Lagrangian density over space-time, on the lattice,

$$S_{\mathrm{QCD}}[\overline{\psi},\psi,U] = S_F[\overline{\psi},\psi,U] + S_G\,[U] = a^4 \sum_{n\in\Lambda} \mathscr{L}_F(n) + a^4 \sum_{n\in\Lambda} \mathscr{L}_G(n)\,. \tag{1.21}$$

In the path integral approach to quantization, all possible field configurations contribute, as opposed to the classical theory where the minima are the only contributions. Each field configuration is weighted with the exponential of the negative Euclidean action $\exp(-S_{\mathrm{QCD}})$.

We are interested in the study of vacuum expectation values of observables $\mathcal{O}[\overline{\psi},\psi,U]$ or, as we will see in the next section, analogously in Euclidean correlators, which are, in general, functionals of the quark and/or gluon fields. These can be obtained in the path integral approach to quantization via

$$\langle\, \mathcal{O}[\overline{\psi},\psi,U]\,\rangle = \frac{\int \mathcal{D}U\,\mathcal{D}\overline{\psi}\,\mathcal{D}\psi\,\mathcal{O}[\overline{\psi},\psi,U]\;\mathrm{e}^{-S_{\mathrm{QCD}}[\overline{\psi},\psi,U]}}{\int \mathcal{D}U\,\mathcal{D}\overline{\psi}\,\mathcal{D}\psi\;\;\mathrm{e}^{-S_{\mathrm{QCD}}[\overline{\psi},\psi,U]}}\,, \tag{1.22}$$

where we integrate over all possible field configurations. It is important to stress that, while on the right hand side we face an integral over the *classical* fields, the left hand side makes the connection to quantum mechanical operators. Thus, the components of the gauge fields U_μ on the right hand side are simply complex numbers. The fermionic fields $\overline{\psi}$ and ψ, however, are anti-commuting Grassmann variables to account for Fermi–Dirac statistics. Note that we treat the fields $\overline{\psi}$ and ψ as independent integration variables, whereas in the Minkowskian operator formalism, these are related by $\overline{\psi} = \psi^\dagger\gamma_0$.

In particular, the integration measure for the gluon fields is defined as

$$\mathcal{D}U \;= \prod_{n\in\Lambda}\prod_{\mu} \mathrm{d}U_\mu(n)\,, \tag{1.23}$$

where each integration measure $\mathrm{d}U_\mu(n)$ for fixed n,μ is a gauge invariant measure over the continuous compact group SU(3), known as the Haar measure, which is normalized to

$$\int \mathrm{d}U_\mu(n) \;= 1, \quad n\in\Lambda, \mu = 1,\ldots,4. \tag{1.24}$$

The fermionic integration measures over the Grassmann variables are defined as

$$\mathcal{D}\overline{\psi}\,\mathcal{D}\psi \;=\; \prod_{n\in\Lambda}\prod_{a,\alpha} \mathrm{d}\overline{\psi}_{a,\alpha}(n)\,\mathrm{d}\psi_{a,\alpha}(n)\;. \tag{1.25}$$

Here, $a = 1,2,3$ denotes the color index, $\alpha = 1,\ldots,4$ stands for the Dirac index. When we include more than one flavor, we sum over the flavors as well.

Let us assume for the moment that our observable is a functional of the gauge fields only, $\mathcal{O}[U]$, hence the only dependence of the fermionic fields of Eq. (1.22) lies in the fermionic part of the action, which is a bilinear form in $\overline{\psi}$ and ψ, compare with (1.11). Then we can solve the Gaussian integral over the Grassmann variables, which yields [27, 28]

$$\int \mathcal{D}\overline{\psi}\,\mathcal{D}\psi\;\exp\left(-\sum_{n,m\in\Lambda}\overline{\psi}(n)D(n,m)\psi(m)\right) \;=\; \det\left[D\right]\;. \tag{1.26}$$

Here $\det\left[D\right]$ is referred to as the *fermion determinant*, which depends on the gauge fields only. As an example of a fermionic field dependent observable, we consider the integral

$$\int \mathcal{D}\overline{\psi}\,\mathcal{D}\psi\,\psi(n)\,\overline{\psi}(m)\;\exp\left(-\sum_{n,m\in\Lambda}\overline{\psi}(n)D(n,m)\psi(m)\right) \;=\; \det\left[D\right]D^{-1}(n,m)\,, \tag{1.27}$$

of the fermionic two-point function $\psi(n)\,\overline{\psi}(m)$, which will be of particular interest for hadron spectroscopy, see Sec. 1.1.4.

As we have seen, for the examples Eqs. (1.26) and (1.27) we were able to explicitly integrate out the fermion dependence of the path integral (1.22). Thereby, the fermionic part of the action transformed into the fermion determinant and the fermionic two-point function got contracted to the inverse Dirac operator – the *quark propagator*. In such cases, we can write the path integral (1.22) as

$$\langle\,\mathcal{O}[U]\,\rangle = \frac{1}{Z}\int \mathcal{D}U\;\mathcal{O}[U]\;\mathrm{e}^{-S_{\mathrm{eff}}[U]}\,, \tag{1.28}$$

where the *effective action* is given by

$$S_{\mathrm{eff}}[U] \equiv \ln\,\det\left[D\right] + S_G\left[U\right]\;. \tag{1.29}$$

In (1.28) we have introduced the partition function

$$Z = \int \mathcal{D}U\;\;\mathrm{e}^{-S_{\mathrm{eff}}}\,, \tag{1.30}$$

which inherits its name from the similarity of the Euclidean path integral with the sum over states in statistical physics.

At this point, we disposed of the Grassmann number dependence of the path integral, which simplifies the numerical integration of expression (1.28) significantly. Nevertheless, the path integral over the gauge fields contains way to many degrees of freedom to be tackled by direct numerical methods. Instead one relies, motivated by the similarity to a statistical system, on Monte Carlo techniques: a sequence of gauge field configurations $U_\mu(n)^{(i)}$, $i = 1, \ldots, N$, is generated with a Boltzmann weight given by the effective action (1.29). Thereby lie the main computational costs in the dependence of the weight factor on the fermion determinant. The costs can be reduced drastically by setting the fermion determinant equal to one and thereby neglecting the effects of dynamical quarks; this approximation is known as *quenching*. A widely used algorithm that does take the effects of dynamical quarks into account is the *hybrid Monte Carlo* (HMC) algorithm [29].

Once the Markov chain of gauge field configurations $U_\mu(n)^{(i)}$, $i = 1, \ldots, N$, has been generated, vacuum expectation values of observables can be approximated as

$$\langle\, \mathcal{O}[U] \,\rangle \approx \frac{1}{N} \sum_{i=1}^{N} \mathcal{O}[U^{(i)}] \,. \tag{1.31}$$

1.1.4 Hadron spectroscopy

The quarks and gluons are the degrees of freedom of QCD, however these are not the states we observe in nature. Instead, confinement binds quarks and gluons together to color neutral objects, the hadrons. Measuring hadron masses on the lattice is a powerful *ab initio* calculation to test the correctness of QCD. In the following discussion, we will denote the time index by t instead of n_4 or n_t. It has to be understood, though, that we still assume a finite space-time lattice, which has important consequences like discrete energy eigenstates. This discussion is based on [30].

The Euclidean correlation function is defined as

$$\langle\, \mathcal{O}_2(t)\, \mathcal{O}_1(0) \,\rangle_T = \frac{\mathrm{tr}\left[\mathrm{e}^{-(T-t)\hat{H}}\, \hat{\mathcal{O}}_2\, \mathrm{e}^{-t\hat{H}}\, \hat{\mathcal{O}}_1 \right]}{\mathrm{tr}\left[\mathrm{e}^{-T\hat{H}} \right]} \,, \tag{1.32}$$

where T is a formal maximum time that we will send to infinity in the later discussion. We can evaluate the trace in the basis of energy eigenstates and insert additionally a complete set of

energy eigenstates to obtain

$$\frac{\sum_{j,k} \langle k| \, \mathrm{e}^{-(T-t)\hat{H}} \, \hat{\mathcal{O}}_2 \, |j\rangle \, \langle j| \, \mathrm{e}^{-t\hat{H}} \, \hat{\mathcal{O}}_1 \, |k\rangle}{\sum_k \langle k| \, \mathrm{e}^{-T\hat{H}} \, |k\rangle} = \frac{\sum_k \mathrm{e}^{-(T-t)E_k} \, \langle k| \, \hat{\mathcal{O}}_2 \, |j\rangle \, \mathrm{e}^{-tE_j} \, \langle j| \, \hat{\mathcal{O}}_1 \, |k\rangle}{\sum_k \mathrm{e}^{-TE_k}} \, . \tag{1.33}$$

Next, we normalize the lowest energy E_0, i.e., the energy of the vacuum $|0\rangle$ to zero, thus the higher energies, $E_1 \leq E_2 \leq E_3 \leq \ldots$, will from now on correspond to the difference to the vacuum's energy. Moreover, we take the limit $T \to \infty$, which yields

$$\lim_{T\to\infty} \langle \, \mathcal{O}_2(t) \, \mathcal{O}_1(0) \, \rangle_T = \sum_j \langle 0| \, \hat{\mathcal{O}}_2 \, |j\rangle \, \langle j| \, \hat{\mathcal{O}}_1 \, |0\rangle \, \mathrm{e}^{-tE_j} \, . \tag{1.34}$$

In this context it is worth mentioning that it follows from Eq. (1.34) that the Euclidean correlator of one or more operators that all live at the same time t is equal to the vacuum expectation value of these operators. Therefore, the terms correlator and vacuum expectation value are often used synonymously. Furthermore, for the same reason, this holds for interpolators and operators.

From the foregoing discussion we know how to calculate Euclidean correlators, which are functionals of the quark and/or gluon fields, on the lattice. We are now in the position to study the correlator of an hadron O, created out of the vacuum at time $t = 0$, which travels through (Euclidean) time and gets annihilated at a later time $t > 0$,

$$\langle \, O(t) \, \overline{O}(0) \, \rangle = \sum_j \langle 0| \, \hat{O} \, |j\rangle \, \langle j| \, \hat{O}^\dagger \, |0\rangle \, \mathrm{e}^{-tE_j} \tag{1.35}$$

$$= A \, \mathrm{e}^{-tE_1} \left(1 + \mathcal{O}(\mathrm{e}^{-t\Delta E})\right) \, . \tag{1.36}$$

E_1 is the lowest (discrete) energy state and ΔE denotes the energy difference to the first excited state. The hadron interpolator O may consist of a quark and an anti-quark to build a meson, e.g., a pion

$$O_\pi(n) = \overline{\psi}^d(n) \gamma_5 \psi^u(n) \, , \tag{1.37}$$

where the u and d label the up and down quark flavors, respectively. Alternatively, O may consist of three quarks to build a baryon, e.g., the proton

$$O_P(n) = \varepsilon_{abc} \psi_a^u(n) \left(\psi_b^u(n)^T C \gamma_5 \psi_c^d(n)\right) \, . \tag{1.38}$$

Here, ε_{abc} is the totally antisymmetric tensor and C refers to the charge conjugation matrix.

With the aim of extracting information of higher lying states of the particles under investigation, one may study the cross correlation matrix instead of a single correlator of type (1.35).

The cross correlation matrix is given by

$$C_{ij}(t) \equiv \langle\, O_i(t)\, \overline{O}_j(0)\, \rangle \tag{1.39}$$

where all the interpolators O_i are required to have the correct quantum numbers of the state one is interested in. The interpolators can vary, e.g., in their Dirac structure or in the type of quark sources being used. To implement different quark sources, one can for example adopt Jacobi smeared sources [31, 32] of different width.

Solving the generalized eigenvalue problem of the cross correlation matrix Eq. (1.39),

$$C(t)\boldsymbol{v} = \lambda(t)C(t_0)\boldsymbol{v}\,, \tag{1.40}$$

gives an estimate for the different energy states by simply identifying the k-th eigenvalue $\lambda_k(t)$ with the exponential of the energy state E_k [33, 34, 35]. Moreover, the corresponding eigenvectors $\boldsymbol{v}$ indicate the overlap of different states. The above described method is in the literature known by the name *variational analysis*.

1.2 Chiral symmetry

This subsection discusses the very characteristic symmetry of QCD that is, in particular its dynamical breaking, responsible for the diverse hadron spectrum in nature – the chiral symmetry. We first list the symmetry for one and for two flavors before we discuss the explicit and spontaneous breaking of the chiral symmetry (this part is based on [36]). We finalize the discussion by presenting the Ginsparg–Wilson equation, which allows for a realization of exact chiral symmetry on the lattice. Furthermore, we give an example for an exact solution to it and present the approximate solution, the chirally improved Dirac operator, which will be adopted in the remainder of this work.

1.2.1 Chiral symmetry in the continuum

In the massless limit, the QCD Lagrangian (1.1) can be separated into two identical parts for the *left-handed* quarks ψ_L and the *right-handed* quarks ψ_R, which are obtained by the projections

$$\psi_L = \frac{1}{2}(\mathbb{1} - \gamma_5)\psi\,, \quad \psi_R = \frac{1}{2}(\mathbb{1} + \gamma_5)\psi\,, \tag{1.41}$$

and accordingly for the conjugate fields $\overline{\psi}$ where the projection acts from the right.

In the following we list a set of transformations of the left- and right-handed fields under which the Lagrangian remains invariant. Therefore, we start with one flavor of dynamical

quarks and then generalize to two flavors.

One flavor of quarks

For the moment we consider QCD with one single flavor of massless quarks. Then, the QCD Lagrangian is invariant under two independent global variations of phases

$$\begin{aligned} \psi_L &= \mathrm{e}^{i\theta_L}\,\psi_L\,, \\ \psi_R &= \mathrm{e}^{i\theta_R}\,\psi_R \end{aligned} \tag{1.42}$$

and hence the underlying symmetry group is

$$\mathrm{U}(1)_L \times \mathrm{U}(1)_R\,. \tag{1.43}$$

Note that the set of rotations (1.42), acting on the left- and right-handed quark fields, is equivalent to the following *vector* and *axial* transformations acting on the fields ψ,

$$\psi = \mathrm{e}^{i\theta_V}\,\psi\,, \tag{1.44}$$

$$\psi = \mathrm{e}^{i\theta_A\gamma_5}\,\psi\,, \tag{1.45}$$

which belong to the symmetry group

$$\mathrm{U}(1)_V \times \mathrm{U}(1)_A\,. \tag{1.46}$$

Two flavors of quarks

Now we generalize the symmetries of the QCD Lagrangian to more than one flavor. In particular, we set $N_f = 2$ but the discussion holds formally for arbitrary N_f. $\mathscr{L}_{\mathrm{QCD}}$ is insensitive to the specific flavors of quarks, one can substitute the two quark flavors by properly normalized orthogonal linear combinations of the latter, which corresponds to a rotation in isospin space. Moreover, since the left- and right-handed components are decoupled, two independent isospin rotations for the two components can be performed:

$$\begin{aligned} \psi_L &= \mathrm{e}^{\frac{i}{2}\theta_L^a\tau^a}\,\psi_L\,, \\ \psi_R &= \mathrm{e}^{\frac{i}{2}\theta_R^a\tau^a}\,\psi_R\,. \end{aligned} \tag{1.47}$$

Here, $\tau^a, a = 1,2,3$ are the Pauli-matrices that, multiplied by factors one half, act as the generators of the group SU(2). Accordingly, the symmetry group for the set of *chiral rotations* (1.47) is the *chiral symmetry*

$$\mathrm{SU}(2)_L \times \mathrm{SU}(2)_R\,. \tag{1.48}$$

Again, we can represent the independent left and right rotations equivalently by independent *isospin* and *axial* rotations

$$\psi = \mathrm{e}^{\frac{i}{2}\theta_V^a \tau^a}\,\psi\,, \tag{1.49}$$

$$\psi = \mathrm{e}^{\frac{i}{2}\gamma_5\theta_A^a \tau^a\gamma_5}\,\psi\,, \tag{1.50}$$

and the symmetry group can formally be denoted in the same fashion as in the one flavor case by

$$\mathrm{SU}(2)_V \times \mathrm{SU}(2)_A\,, \tag{1.51}$$

where it has to be stressed, though, that the axial set of rotations "$\mathrm{SU}(2)_A$" does not form a group.

Besides, the QCD Lagrangian for two quark flavors remains invariant under variations of the common phase of the left-handed and right-handed quarks of both flavors Eq. (1.42) and we can summarize the symmetries for the massless QCD Lagrangian as

$$\mathrm{SU}(2)_L \times \mathrm{SU}(2)_R \times \mathrm{U}(1)_A \times \mathrm{U}(1)_V\,. \tag{1.52}$$

1.2.2 Breaking of the chiral symmetry

Explicit breaking

The full set of symmetries (1.52) of the QCD Lagrangian (1.1) holds only in the classical theory with massless fermions. In the quantized theory, the noninvariance of the fermion determinant under $\mathrm{U}(1)_A$ renders the fermion integration measure noninvariant and thus breaks the flavor singlet axial symmetry. This explicit breaking of the $\mathrm{U}(1)_A$ symmetry is known as *axial anomaly*.

When we allow the two quark flavors to have nonvanishing degenerate masses, the mass term in the Lagrangian breaks the remaining symmetry down to

$$\mathrm{SU}(2)_V \times \mathrm{U}(1)_V\,. \tag{1.53}$$

$\mathrm{SU}(2)_V$ is the isospin symmetry, which is approximately preserved in nature for the up and down quarks and accounts for the almost degenerate masses of the proton and the neutron. The $\mathrm{U}(1)_V$ symmetry that, in contrast to $\mathrm{SU}(2)_V$, even survives nondegenerate quark masses, conserves the baryon number.

Dynamical breaking

The masses of the two lightest quark flavors in nature, the up and down quarks, are roughly three orders of magnitude smaller than the typical scale of QCD, which gives reason to expect the full symmetry (1.52), except for the singlet flavor axial symmetry that is broken explicitly by the anomaly, to be approximately conserved.

If the ground state of the theory is not invariant under the same set of transformations as the Lagrangian, one speaks of *spontaneous symmetry breaking* and the theory is said to be in the Nambu–Goldstone mode [37, 38, 39]. The latter is opposed to the Wigner–Weyl mode, which is expected to show excitations grouped into representations of the chiral group. In particular, parity doubling is expected, which is not seen in nature. Therefrom one can conclude that the isospin axial chiral symmetry (1.50) is broken spontaneously by the dynamics of QCD. In contrast, the vector part of the chiral symmetry cannot be broken spontaneously in accordance with the Vafa–Witten theorem [40].

The noninvariance of the vacuum with respect to the three axial transformations requires the existence of three massless isospin triplet pseudoscalar Goldstone bosons, which can be identified with the pions. The pions are not exactly massless in nature, which may be attributed to the explicit symmetry breaking by the small nonvanishing mass of the up and down quarks. Nevertheless, the pions are much lighter than the other quark bilinear excitations like, e.g., the rho.

A nonvanishing *chiral condensate* $\langle\, \overline{\psi}(x)\, \psi(x) \,\rangle$ indicates that the system is in the Nambu–Goldstone mode. The chiral condensate is not invariant with respect to both, the flavor singlet axial rotation and the axial rotation in isospin space.

1.2.3 The Ginsparg–Wilson equation

The essence of the chiral symmetry in the continuum can be condensed to the fact that the Dirac operator has to anti-commute with γ_5 in order to obtain a Lagrangian invariant under (1.52), i.e.,

$$\{D, \gamma_5\} = 0\,. \tag{1.54}$$

As stated above, the Nielsen–Ninomiya theorem [20, 21, 22] constrains the lattice action to be invariant under (1.52) *or* to maintain other crucial properties like locality and a theory free of fermion doublers. In this sense it is not possible to implement chiral symmetry on the lattice in the naive way (1.54).

However, Ginsparg and Wilson [41] proposed to replace the above continuum expression by a lattice version,

$$\{D, \gamma_5\} = aD\gamma_5 D\,, \tag{1.55}$$

which agrees with Eq. (1.54) in the continuum limit. Dirac operators D that fulfill the Ginsparg–Wilson (GW) equation (1.55) then allow for an exact chiral symmetry on the lattice. Therefore, the transformations of type (1.45) are replaced by a lattice version [42]

$$\psi = \mathrm{e}^{i\theta_A\gamma_5\left(\mathbb{1}-\frac{a}{2}D\right)}\,\psi\,, \tag{1.56}$$

and equivalently for the fields $\overline{\psi}$, which converge to the continuum transformations in the limit $a \to 0$.

Only many years after the discovery of the GW equation (1.55), two independent approaches succeeded to provide a solution to the nonlinear equation, the most prominent one being Neuberger's *overlap operator* [43, 44].

1.2.4 The chirally improved Dirac operator

The overlap operator, while yielding exact chiral symmetry on the lattice, is computationally very expensive. Another approach to tackle the problem of implementing chiral symmetry on the lattice is the chirally improved (CI) Dirac operator [45, 46], which we adopt as the fermion discretization of choice in the remainder of this work.

The CI Dirac operator solves the GW equation only approximately. It is obtained by expanding the most general Dirac operator in a basis of simple operators,

$$D_{\mathrm{CI}}\,(x,y) = \sum_{i=1}^{16} c_{xy}^{(i)}(U)\Gamma_i + m_0\mathbb{1}. \tag{1.57}$$

Here, the sum runs over all elements Γ_i of the Clifford algebra and the coefficients $c_{xy}^{(i)}(U)$ consist of path ordered products of the link variables U connecting lattice sites x and y. Inserting this expansion into the GW equation then turns into a system of coupled quadratic equations for the expansion coefficients of the D_{CI} . This expansion provides for a natural cutoff that turns the quadratic equations into a simple finite system.

The ansatz is constructed such that all symmetries of the fermionic action are maintained and moreover γ_5-hermiticity is imposed.

1.3 Confinement

This subsection is dedicated to a brief discussion of confinement, which is, besides the dynamical breaking of the chiral symmetry, the second characteristic phenomenon of QCD. A popular way of defining confinement, besides many possible choices, see [47] for a detailed discussion, is the existence of a linear rising potential between two static quarks. However, then, strictly

speaking, QCD is not confining since the separation of two static quarks will eventually create a quark anti-quark pair out of the vacuum as soon as it is energetically preferred, this is known as *string-breaking*.

Related with this is another symmetry of SU(N_c) Yang–Mills theories, i.e., pure gauge theory without quarks: the center symmetry. The center of a group consists of those group elements that commute with all other elements of the group. For SU(N_c), the center group is Z_{N_c} and is given by the elements $z_n \mathbb{1}$ with $z_n = \exp(2\pi i n/N_c)$ and $n = 0, \ldots, N_c - 1$. The pure gauge Lagrangian on the lattice (1.20) is invariant under the global transformation

$$U_0(\boldsymbol{x}, t_0) \to z U_0(\boldsymbol{x}, t_0) \quad \text{for all } \boldsymbol{x} \text{ and fixed } t_0. \tag{1.58}$$

Spontaneous breaking of this symmetry at high temperatures as well as explicit breaking by quark fields, occurs in conformity with the vanishing of the asymptotically linear rising potential between static color sources: if center symmetry is unbroken, the energy of an isolated color charge is infinite, while, on the contrary, if the symmetry is spontaneously broken, the energy of an isolated color charge is finite. The expectation value of the *Polyakov loop* serves as an order parameter for the breaking of the center symmetry.

For the later chapters it will be important to have a definition of confinement that does not rely on properties of the gauge background. Later we will modify the quark propagators, which stem from the inversion of the Dirac operator on given gauge field configurations, *a posteriori*. Thus, in order to check for confining properties, it does not make sense to investigate the underlying gauge fields that have not been touched.

Therefore, we will focus on *color-confinement* in the later discussion, which is to be understood as the absence of color-charged asymptotic particle states. In other words, this refers to the fact that free quarks are never observed in nature. In practice we will check for the persistence of bound particle states. In has to be stressed, however, that this does not necessarily imply a underlying linearly rising potential.

1.4 Eigenvalues of the Dirac operator

The eigenvalues of the Dirac operator, in particular the low lying eigenvalues, reflect several physical phenomena. Crucial properties of the Dirac eigenspectrum, as well as the connection between the low lying eigenvalues and the breaking of the chiral symmetry, will be covered below.

1.4.1 Topology

The following discussion is based on [48]. The γ_5-hermiticity of lattice Dirac operators (Sec. 1.4.2) ensures that its eigenvalues come either in complex conjugate pairs or are purely real. The overlap Dirac operator, which fulfills the GW equation in the form of (1.55), has all its eigenvalues lying on a circle[1] and thus maintains exact zero modes (in the chiral limit). Other operators which do not obey the GW equation, in contrast, exhibit a scattered spectrum and would-be zero modes are shifted along the real axis.

The Atiyah–Singer index theorem [49] relates the left- and right-handed zero modes

$$\gamma_5 v_0 = \pm v_0 \quad \text{with} \quad D v_0 = 0, \tag{1.59}$$

of the massless Dirac operator to the topological charge Q_{top}. Its lattice version [50] reads $Q_{\text{top}} = n_- - n_+$ where n_- and n_+ denote the left- and right-handed zero modes, i.e., the number of eigenmodes with eigenvalue zero for which (1.59) holds. In the picture of instanton liquids, the localized topological configurations, i.e., the *topological lumps* of different charges get mixed and one cannot assume that the zero eigenvalues survive unperturbed but move towards the imaginary axis. It can be shown that the topological charge that results from the would-be zero modes is responsible for the noninvariance of the fermion integration measure under flavor singlet axial rotations of the form (1.56).

The Banks–Casher relation [51] connects the emerging density of eigenvalues $\rho(0)$ *near the origin* to a nonvanishing chiral condensate,

$$\langle \overline{\psi}\psi \rangle = -\pi \rho(0). \tag{1.60}$$

Whereby it is crucial to first take the infinite volume limit at finite quark mass since strictly speaking, in a finite volume, spontaneous breaking of a symmetry cannot occur. Subsequently, the chiral limit $m \to 0$ is taken.

1.4.2 Spectral decomposition

Here we summarize important spectral properties of the Dirac operator and the *hermitian Dirac operator*. To this end we give formulas how these can be represented by their eigenvalues and -vectors. The Dirac operator of QCD on a four dimensional lattice has the dimensionality $N = 12\,|\Lambda|$ where the factor 12 is the product of color and Dirac index dimensions and $|\Lambda| = N_s^3 N_t$ is the number of lattice points.

1 There are more general GW fermions, where the eigenvalues lie between two circles.

In general, the Dirac operator with a finite cut-off is a non-normal operator, i.e., it does not commute with its hermitian conjugate,

$$[D, D^\dagger] \neq 0. \tag{1.61}$$

The normality of an operator $\tilde{D}$ ensures that the operator's eigenvectors build an orthogonal basis of the underlying (complex) vector space and thus the operator can be diagonalized by a unitary transformation U,

$$\Lambda = U^\dagger \tilde{D} U, \tag{1.62}$$

where now Λ denotes the diagonal matrix of the operator $\tilde{D}$ that consists of its eigenvalues. Non-normal operators, on the other hand, can – if at all – only be diagonalized by a non-unitary similarity transformation X,

$$\Lambda = X^{-1} D X. \tag{1.63}$$

Eq. (1.63) is equivalent to

$$DX = X\Lambda \iff X^{-1} D = \Lambda X^{-1} \tag{1.64}$$

from which it becomes apparent that the left and right eigenvectors, which are defined by

$$\langle L_i | D = \lambda_i \langle L_i | , \quad D | R_i \rangle = \lambda_i | R_i \rangle , \quad i = 1, \ldots, N, \tag{1.65}$$

i.e., the rows of X^{-1} and the columns of X, respectively, differ. The latter stems from the non-unitarity of the basis transformation: $X^{-1} \neq X^\dagger$. Despite the fact that the sets of left and right eigenvectors do not build an orthogonal basis by themselves,

$$\langle L_i | L_j \rangle \neq \delta_{ij}, \quad \langle R_i | R_j \rangle \neq \delta_{ij}, \tag{1.66}$$

the relation $X^{-1} X = \mathbb{1}$ yields the following *biorthogonality* condition

$$\langle L_i | R_j \rangle = \delta_{ij} . \tag{1.67}$$

The biorthogonality condition ensures that non-normal operators D can be expressed in a modified spectral representation that includes left and right eigenvectors,

$$D = \sum_{i=1}^{N} \lambda_i | R_i \rangle \langle L_i | . \tag{1.68}$$

It has to be stressed that when the eigenvectors are normalized according to

$$\langle L_i|L_i\rangle = 1, \quad \langle R_i|R_i\rangle = 1, \tag{1.69}$$

the biorthogonality (1.67) is only fulfilled up to a constant and (1.68) has to be normalized with factors $1/\langle L_i|R_i\rangle$, accordingly.

Wilson type Dirac operators are γ_5-hermitian,

$$D = \gamma_5 D^\dagger \gamma_5 \,, \tag{1.70}$$

thus the Dirac operator's eigenvalues are either real or come in complex conjugate pairs. The γ_5-hermiticity of D enables us to derive a relation between the left and right eigenvectors,

$$\begin{aligned} & \gamma_5 D^\dagger \gamma_5 \,|R_i\rangle = \lambda_i \,|R_i\rangle \\ \Longleftrightarrow \;& D^\dagger \gamma_5 \,|R_i\rangle = \lambda_i \gamma_5 \,|R_i\rangle \\ \Longleftrightarrow \;& \langle R_i|\,\gamma_5 D = \lambda_i^* \,\langle R_i|\,\gamma_5 \,. \end{aligned} \tag{1.71}$$

Hence, the left eigenvectors to eigenvalue λ_i equal the hermitian conjugate right eigenvectors, multiplied by γ_5 from the right, to the complex conjugate eigenvalue λ_i^*.

The inverse Dirac operator is then given by

$$D^{-1} = \sum_{i=1}^{N} \lambda_i^{-1} \,|R_i\rangle \,\langle L_i| \,. \tag{1.72}$$

The columns of D^{-1} build the quark propagators to different point-sources. An alternative way to represent the Dirac operator by a spectral decomposition is to use its γ_5-hermiticity (1.70). From the latter it follows that the hermitian Dirac operator $D_5 \equiv \gamma_5 D$ is a normal operator, i.e., there exists an orthogonal basis of eigenvectors $|w_i\rangle$ such that D_5 can be decomposed as

$$D_5 = \sum_{i=1}^{N} \mu_i \,|w_i\rangle \,\langle w_i| \tag{1.73}$$

with μ_i denoting the (real) eigenvalues of D_5. The inverse of (3.30) yields

$$D^{-1} = \sum_{i=1}^{N} \mu_i^{-1} \,|w_i\rangle \,\langle w_i|\,\gamma_5 \,. \tag{1.74}$$

1.4.3 Truncating the quark propagator

The main underlying idea of this thesis lies in the artificial restoration of the chiral symmetry by removal of the chiral condensate in the valence quark sector stepwise in the sense of eliminating the density of the near zero modes, see Eq. (1.60).

More precisely, we aim at constructing hadron correlators out of quark propagators that exclude the lowest part of the Dirac spectrum. Thus, we split the Dirac operator into a low-mode part and a *reduced* part,

$$D = \sum_{i=1}^{k} \lambda_i \left|R_i\right\rangle \left\langle L_i\right| + \sum_{i=k+1}^{N} \lambda_i \left|R_i\right\rangle \left\langle L_i\right| . \tag{1.75}$$

where k is a parameter that we will vary in the range from zero to a few hundred modes. In order to construct the reduced or *truncated* quark propagators,

$$S_{\mathrm{red}(k)} = \sum_{i=k+1}^{N} \lambda_i^{-1} \left|R_i\right\rangle \left\langle L_i\right| , \tag{1.76}$$

it is sufficient to calculate the lowest k eigenvalues and construct the low-mode part of the quark propagator according to

$$S_{\mathrm{lm}(k)} = \sum_{i=0}^{k} \lambda_i^{-1} \left|R_i\right\rangle \left\langle L_i\right| . \tag{1.77}$$

Subsequently, the low-mode part is subtracted from the full propagators in order to obtain the reduced propagators,

$$S_{\mathrm{red}(k)} = S - S_{\mathrm{lm}(k)} . \tag{1.78}$$

The full quark propagator is calculated in the standard way by inverting the Dirac matrix for all color and Dirac index combinations on a given source b,

$$\sum_{n\in\Lambda} D(m,n)\, S(n) = b(m) . \tag{1.79}$$

1.4.4 Connection to lattice momenta

Finally, we derive a relation between the eigenvalues of the free Dirac operator and the discrete momenta on the lattice.[1] To this end, we first stress that the eigenvalues of the Dirac operator

1 Thanks to Christof Gattringer for pointing this out.

$D(x,y)$ remain the same after a Fourier transform to momentum space since the Fourier transform is a unitary transformation. For the definition of the lattice momenta see (6.23).

Wilson-type Dirac operators consist of a Dirac scalar and a Dirac vector part,

$$D(p) = s\mathbb{1} + i\not{k}\,, \tag{1.80}$$

where $\not{k} = \sum_\mu \gamma_\mu k_\mu(p)$ are the lattice momenta in Feynman's slash notation. With s the mass term plus, e.g., a Wilson term, which depends on p as well, is denoted. Without gluon interactions, $D(p)$ is diagonal in color and momentum space and therefore the Dirac matrix is block-diagonal with the 4×4 blocks stemming from the internal Dirac structure.

In order to yield the eigenvalues λ of a block of $D(p)$ for fixed p (and thus fixed k) one demands the characteristic polynomial,

$$P(\lambda) = \det\left[\lambda\mathbb{1} - D(p)\right] = \det\left[(\lambda - s)\mathbb{1} - i\not{k}\right]\,, \tag{1.81}$$

to be equal to zero. From the latter we pull out a factor $(\lambda - s)$ to obtain

$$(\lambda - s)^4 \det\left[\mathbb{1} - \frac{1}{\lambda - s} i\not{k}\right] = (\lambda - s)^4 \exp\left(\operatorname{tr}\left[\ln\left(\mathbb{1} - \frac{i\not{k}}{\lambda - s}\right)\right]\right) \tag{1.82}$$

where we used a common trick to expand the determinant. The logarithm of a matrix is defined in terms of its power series which reads

$$(\lambda - s)^4 \exp\left(\operatorname{tr}\left[-\sum_{n=1}^{\infty} \frac{1}{n}\left(\frac{i\not{k}}{\lambda - s}\right)^n\right]\right)\,. \tag{1.83}$$

When evaluating the trace we use the fact that the trace over terms with odd n vanishes and moreover the identity $\not{k}^2 = k^2\mathbb{1}$,

$$(\lambda - s)^4 \exp\left(-\sum_{n=1}^{\infty} \frac{1}{2n}\left(\frac{1}{\lambda - s}\right)^{2n} \operatorname{tr}\left[(i\not{k})^{2n}\right]\right) \tag{1.84}$$

$$= (\lambda - s)^4 \exp\left(-\sum_{n=1}^{\infty} \frac{4}{2n}\left(\frac{-k^2}{(\lambda - s)^2}\right)^n\right) \tag{1.85}$$

where the factor of 4 stems from the trace over the identity. We substitute back the power

series with the logarithm and simplify

$$(\lambda - s)^4 \exp\left(-2 \sum_{n=1}^{\infty} \frac{1}{n} \left(\frac{-k^2}{(\lambda - s)^2}\right)^n\right) \tag{1.86}$$

$$= (\lambda - s)^4 \exp\left(2 \ln\left(1 + \frac{k^2}{(\lambda - s)^2}\right)\right) \tag{1.87}$$

$$= (\lambda - s)^4 \left(1 + \frac{k^2}{(\lambda - s)^2}\right)^2 \tag{1.88}$$

$$= \left((\lambda - s)^2 + k^2\right)^2 . \tag{1.89}$$

Requiring the characteristic polynomial to be equal to zero is then equivalent to

$$(\lambda - s)^2 + k^2 = 0 \iff \lambda = s \pm i\,|k| \ . \tag{1.90}$$

Note that each of the two eigenvalues is degenerate.

We see that (1.90) reveals a connection of the lowest eigenvalues of the free Dirac operator to the lowest momenta on the lattice. Turning on the interactions with the gluon fields can be formally accounted for by dressing the terms of (1.80) with momentum dependent dressing functions on each configuration. The difficulty is, though, that the interacting Dirac operator is no longer of block-diagonal form, which renders the derivation of an analog analytical connection impossible. Nevertheless, the similarity of the overall shape of the eigenspectrum of free fermions compared with interacting fermions, see e.g. [52], is a strong indication that the dynamics of QCD do not invalidate the main feature of (1.90) which is the relation of low lying Dirac eigenmodes to low momenta on the lattice.

Chapter 2

Unbreaking chiral symmetry

We have now collected all necessary basics so that we are in the position to continue with the presentation of the first publication which resulted from the work on the thesis' subject. This chapter consists of the article

- [1] C. B. Lang, Mario Schröck, *"Unbreaking chiral symmetry"*, Phys. Rev. D **84** (2011) 087704.

Here we studied ground states of isovector mesons under Dirac low-mode truncation. We explored the truncation range which is of physical interest and gained first insights in the consequences of Dirac low-mode removal on low lying mesons.

2.0 Abstract

In quantum chromodynamics (QCD) the eigenmodes of the Dirac operator with small absolute eigenvalues have a close relationship to the dynamical breaking of the chiral symmetry. In a simulation with two dynamical quarks, we study the behavior of meson propagators when removing increasingly more of those modes in the valence sector, thus partially removing effects of chiral symmetry breaking. We find that some of the symmetry aspects are restored (e.g., the masses of ρ and a_1 approach each other) while confining properties persist.

2.1 Motivation and introduction

Dynamical chiral symmetry breaking in QCD is associated with the low lying spectral modes of the Dirac operator D [51]. They affect the path integral weight of the gauge configurations

through the determinant of D. As indicated by the Atiyah-Singer index theorem [49], the exact zero modes are related to topological excitations, the instantons. For Dirac operators violating chiral symmetry these are real eigenmodes. The nearby nonreal modes are also thought to be related to composed structure of, e.g., overlapping instantons [53].[1]

In a series of papers [14, 15, 16] it was emphasized that low-modes saturate the pseudoscalar and axial vector correlators at large distances and do not affect the part where high lying states appear. In [16, 17] low-mode saturation and also effects of low-mode removal for mesons were studied for quenched configurations with the overlap Dirac operator [43, 44].

Subsequently low-modes were utilized to improve the convergence of the determination of hadron propagators [16, 17, 18, 54] (see also the recent study [55, 56] comparing the efficiency when using the low-modes of the Dirac operator or the hermitian Dirac operator, where strong dependence on the parity of the hadron states was presented).

Associating the low-mode sector with the nonperturbative chiral symmetry breaking and the condensate [51], a complementary question is how important it is for confinement and mass generation of hadrons. Here we study what happens if one removes up to 512 low lying modes from the valence quark sector. We compute propagators of the pion and other mesons and determine the effect of this removal on the mass spectrum. This way we want to shed light on the role of the condensate related to the spectral part of the Dirac operator in confinement and chiral symmetry breaking. Our analysis is done for configurations generated for two light, mass degenerate dynamical quark flavors. The removal of the low lying modes is effective only in the valence quarks sector. However, as will be seen, this already has significant impact on the meson mass spectrum.

In [57, 58] it has been conjectured that chiral symmetry is "effectively restored" for highly excited hadrons, in the sense that valence quarks become less affected by the quark condensate. This situation is similar to ours, where we artificially suppress the condensate as seen by the valence quarks. In the context of effective restoration such an approach has been discussed already in [16, 19].

2.2 Reduced Dirac operator

Lattice Wilson Dirac operators and approximate Ginsparg-Wilson Dirac operators are γ_5-hermitian, $\gamma_5 D \gamma_5 = D^\dagger$, but non-normal, thus their spectral representation has real and complex eigenvalues and the left and right eigenvectors are bi-orthogonal, i.e. $\langle L_i | R_j \rangle = \delta_{ij}$.

1 Even when studying the low lying modes in quenched gauge ensembles one observes nonvanishing density and also the Gell-Mann–Oakes–Renner relation works down to small values of the valence quark mass until quenched chiral logs destroy the leading chiral symmetry breaking behavior.

The so-called hermitian Dirac operator $D_5 \equiv \gamma_5 D$ has real eigenvalues μ_i and the eigenvectors are orthogonal.

We want to construct meson correlators from valence quark propagators that exclude the lowest part of the Dirac spectrum. There are two alternative definitions of reduction: based on eigenmodes of D or based on eigenmodes of the hermitian Dirac operator. We introduce the reduced quark propagator via the spectral representation of D_5,

$$S_{\mathrm{red5}(k)} = S - S_{\mathrm{lm5}(k)} \equiv S - \sum_{i \leq k} \mu_i^{-1} |v_i\rangle\langle v_i|\gamma_5 \ . \tag{2.1}$$

Another alternative works with the bi-orthogonal eigensystem of D. The two types of truncation are not equivalent. We first tested the convergence of the low-mode approximation and, as has been observed in [56], find a clearly slower convergence rate for the standard non-hermitian as compared to the hermitian Dirac operator. In our study we therefore concentrate on our results from truncating the hermitian Dirac operator.

2.3 Chiral symmetry and its breaking

The nonvanishing quark masses of the two lightest quark flavors are relatively small in comparison to the typical QCD scale. Neglecting the masses of the u and d quarks the QCD Lagrangian is invariant under the symmetry group

$$\mathrm{SU}(2)_L \times \mathrm{SU}(2)_R \times \mathrm{U}(1)_V \times \mathrm{U}(1)_A \ . \tag{2.2}$$

The chiral symmetry $\mathrm{SU}(2)_L \times \mathrm{SU}(2)_R$ consists of independent transformations in the isospin space for the left- and right-handed quark fields and can be represented equivalently by independent isospin and axial rotations for the combined quark fields.

The isospin axial transformation mixes states with opposite parity but the same spin. Depending on quantum numbers the chiral partners can have the same or different isospin. The nondegenerate masses of parity partners indicate the dynamical (spontaneous) breaking of this chiral symmetry with the order parameter $\langle\overline{\psi}\psi\rangle$, the chiral condensate. Spontaneous breaking of the chiral symmetry leads to the appearance of the pseudoscalar Goldstone bosons, the pions.

The flavor singlet axial transformation symmetry $\mathrm{U}(1)_A$ is broken explicitly due to the noninvariance of the fermion integration measure, the so-called axial anomaly. It is not a symmetry of the quantized QCD. Consequently no isosinglet Goldstone boson exists within the two-flavor QCD and the η meson(s) are heavier then the pion, attributed to the anomaly. In addition to the anomaly also the chiral condensate breaks this symmetry.

Both symmetry breaking signals are related to low lying modes of the Dirac operator. The

axial anomaly involves the topological charge of the gauge configuration, which is proportional to the net number of exactly chiral (zero-)modes via the Atiyah-Singer index theorem [49]. The chiral condensate is associated with the density of the Dirac operator's low lying (but nonzero) modes [51]. The nonvanishing quark condensate indicates breaking of both symmetries.

2.4 Gauge configurations

For our analysis we used 161 gauge field configurations [59, 60] of lattice size $16^3 \times 32$; with the lattice spacing $a = 0.144(1)\,\mathrm{fm}$ this corresponds to a spatial size of 2.3 fm. The simulation includes two degenerate flavors of light fermions and a corresponding pion mass of $m_\pi = 322(5)\,\mathrm{MeV}$. For the dynamical quarks of the configurations as well as for the valence quarks the so-called chirally improved Dirac operator [45, 46] has been used. This operator is an approximate solution to the Ginsparg–Wilson equation and therefore exhibits better chiral properties than the simpler Wilson Dirac operator while being less expensive by an order of magnitude – in terms of computation time – in comparison to the chirally exact overlap operator.

We calculated up to the lowest 256 eigenmodes of the Dirac operator D and up to lowest the 512 eigenmodes of the hermitian operator D_5 using ARPACK which is an implementation of the Arnoldi method to calculate part of the spectrum of arbitrary matrices [61].

The quark propagator S is determined by inverting the Dirac operator for a given source. Instead of using point sources we use Jacobi smeared sources [31, 32] that are approximately of Gaussian shape. Their shape was adjusted to a width of about 0.27 fm [59]. The low-mode contribution $S_{\mathrm{lm5}(k)}$ to the quark propagator, see (2.1), has to be multiplied with the same sources as the full propagator S in order to achieve the correct reduced propagators $S_{\mathrm{red5}(k)}$.

2.5 Mesons

We restrict ourselves to the study of isovectors, in particular, the chiral partners:

- The vector mesons ρ ($J^{PC} = 1^{--}$) with interpolating fields $\overline{u}(x)\gamma_i d(x)$ and $\overline{u}(x)\gamma_4\gamma_i d(x)$ and a_1 ($J^{PC} = 1^{++}$) with interpolating field $\overline{u}(x)\gamma_i\gamma_5 d(x)$; in a chirally symmetric world the vector and the axial vector interpolator get mixed via the isospin axial transformations.

- The pseudoscalar π ($J^{PC} = 0^{-+}$) with interpolating fields $\overline{u}(x)\gamma_5 d(x)$ and $\overline{u}(x)\gamma_4\gamma_5 d(x)$. We also study the scalar a_0 ($J^{PC} = 0^{++}$), $\overline{u}(x)d(x)$, which would get mixed with $\overline{u}(x)\gamma_5 d(x)$ via the $\mathrm{U}(1)_A$ transformation.

(In the interpolators γ_4 denotes the Dirac matrix in Euclidean time direction.)

We compute from the quark propagators meson propagators, projected to vanishing momentum and determine the hadron masses from a range of Euclidean time values where the correlation function exhibits exponential decay. The final errors are statistical only and obtained by standard jackknife elimination sampling.

2.6 Results

2.6.1 Low-mode sector

Figure 2.1 shows the integral over the distribution $H(|\mu|)$ of the (real) eigenvalues of D_5. The scale is set by the lattice spacing. There is a transition region up to roughly twice the size of the quark mass (for this simulation the unrenormalized mass calculated from the axial Ward identity is 15 MeV [60]) corresponding to $\mathcal{O}(16)$ eigenmodes, as also observed in, e.g., [62, 63, 64, 65]. As will be seen below, this is in accordance with the behavior observed for the meson propagators.

For the overlap operator the real eigenvalues correspond to exact chiral modes, the zero modes. This is no longer true for Wilson-type operators. There one may associate zero modes with real eigenvalues, although there chirality is not unity. For the hermitian Dirac operator there is no simple method to identify these would-be zero modes, and thus all we can say is that the lowest eight modes include a significant number (if not all) of the would-be zero modes (instantons).

Before we construct meson correlators out of reduced quark propagators, let us first consider meson correlators approximated by the lowest k modes only, using propagators $S_{\mathrm{lm5}(k)}$, see (2.1).

In Fig. 2.2 we compare the pseudoscalar correlator using standard full propagators to the correlators using only the lowest modes of the hermitian Dirac operator D_5. For the two pseudoscalar operators the exponential pion decay behavior sets it much earlier (at lower numbers of eigenmodes) for the interpolator $\overline{u}\gamma_5 d$ than for the other interpolator $\overline{u}\gamma_4\gamma_5 d$. Clearly the first one is stronger dominated by the low lying modes than the second. The large time region is well described by the low-modes whereas the short time region – where excited states dominate – gets saturated much more slowly. Comparing with the result for an equivalent approximation for the non-hermitian Dirac operator (not shown here), we find that less eigenmodes of D_5 are needed to obtain a similar quality of approximation of the correlators with full propagators. These results agree with the observations in [16, 17, 56].

2.6.2 Removing the low-mode sector

Figure 2.3 shows the meson propagators for various stages of low-mode *removal*, always in comparison with the full propagator, and Fig. 2.5 combines the corresponding mass fits to the

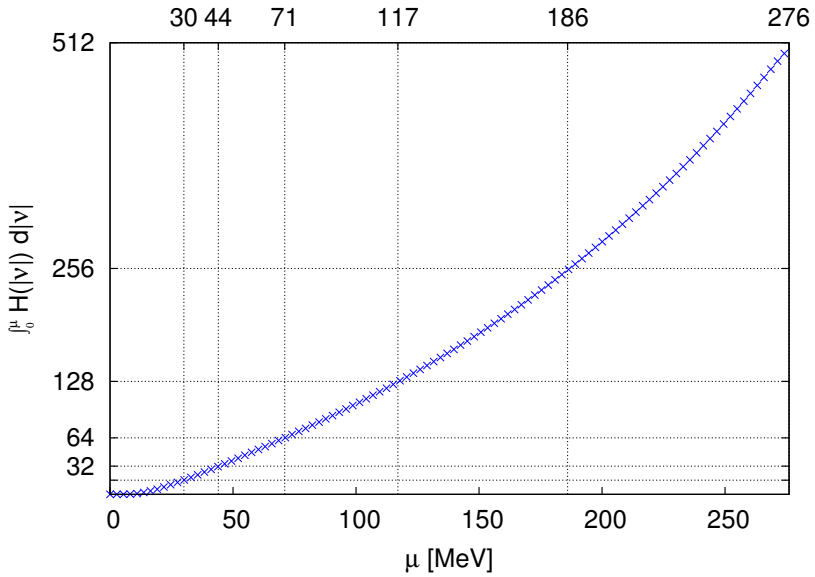

Figure 2.1: The integrated eigenvalue density for the lowest 512 (absolute) eigenvalues of D_5. The eigenvalues are scaled according to the lattice spacing. The number on the upper axis indicates the values of μ where there are 16, 32, 64, 128, 256 and 512 eigenvalues below that value.

regions of exponential behavior.

All mass values (except for the ρ) exhibit a strong dependence on the truncation of the lowest eigenmodes; from truncations levels of ~ 16 modes upwards (corresponding to quark masses of approximately 30 MeV) all mass values then follow a roughly parallel, rising behavior. The range of exponential behavior of the correlators shrinks, as can be seen in the log-plots in Fig. 2.3.

The effective mass plots (the local two-point approximation of the derivative of the logarithm of the correlators) in Fig. 2.4 indicate the regions, where an exponential fit to the correlators has been done. We find that the fluctuation typically decreases with increasing reduction. This may be related to the relative importance of the noisy low lying modes in the quark propagators.

In [66] the parity-chiral group and the effect of symmetry breaking on the meson spectrum is discussed. For example, whereas the $\mathrm{U}(1)_A$ breaking lifts the degeneracy between pion and a_0 (and between η and f_0) the breaking of the chiral $\mathrm{SU}(2)_L \times \mathrm{SU}(2)_R$ symmetry is related to the mass differences of pion and f_0 (and a_0 and η). From Fig. 2.5 we find drastic sensitivity on low-modes for both, the pion interpolator masses and the a_0 mass. At low truncation levels the a_0 mass rapidly drops; it does not drop down to the pion mass value. This might indicate some remnant of the anomaly breaking for the $J = 0$ states.

The pion interpolators exhibit a puzzling behavior. The classical pion interpolator $\overline{u}\gamma_5 d$ quickly loses its exponential behavior at larger (Euclidean) distances; only a more massive

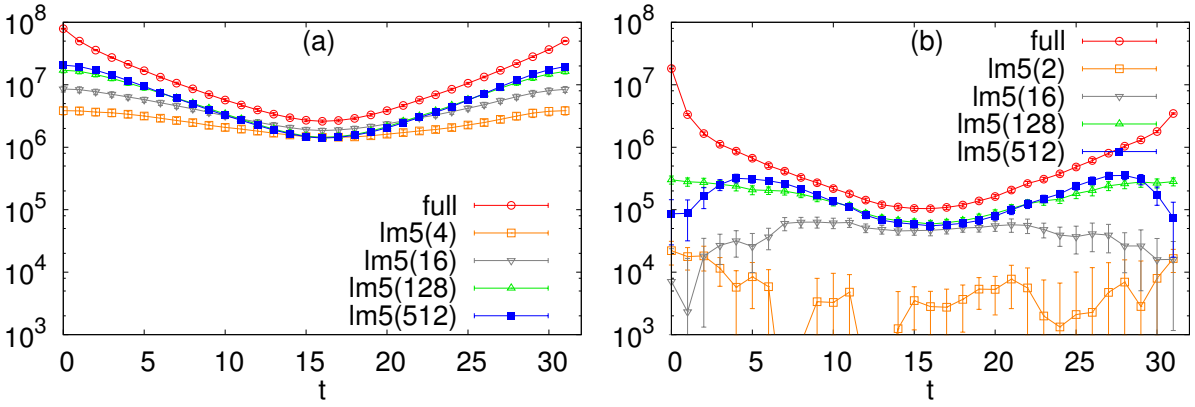

Figure 2.2: Low-mode contribution to the correlators for the $J^{PC} = 0^{-+}$ sector in comparison to the correlators from full propagators with interpolators (a) $\overline{u}\gamma_5 d$ and (b) $\overline{u}\gamma_4\gamma_5 d$. The number of included modes is shown in the legend.

decay signal is observed at smaller distances (Fig. 2.3). From truncation level 16 onwards we therefore do not exhibit mass values in Fig. 2.5 for that interpolator. A fit to the very small time slices gives a mass approaching the mass value from the second interpolator $\overline{u}\gamma_4\gamma_5 d$ with the pion quantum numbers, which couples due to PCAC (proportional to the quark mass).

For the $J^{PC} = 1^{--}$ vector meson ρ there are two chiral representations, which correspond to the vector interpolator $\overline{u}\gamma_i d$ and (Dirac-)tensor interpolator $\overline{u}\gamma_4\gamma_i d$. Their chiral partners [66] are the a_1 and the h_1 mesons, respectively. We did not determine the h_1 mass, since its interpolator includes disconnected graphs (it is an $I = 0$ state). There is no noticeable splitting between the two ρ-interpolators for all stages of truncation. We do find, however, intriguing behavior comparing the ρ mass with the a_1 result. Starting out quite differently for the full quark propagator, the masses approach each other and are compatible with each other from truncation level 8 onwards. This indicates restoration of the $\mathrm{SU}(2)_L \times \mathrm{SU}(2)_R$ symmetry for $J = 1$ states. The very fact that all three interpolators (vector, tensor and axial vector) give the same mass hints to the restoration of the $\mathrm{SU}(2)_L \times \mathrm{SU}(2)_R \times \mathrm{U}(1)_A$ symmetry for $J = 1$ states. The latter could be reliably concluded, however, only after studying of the h_1 meson.

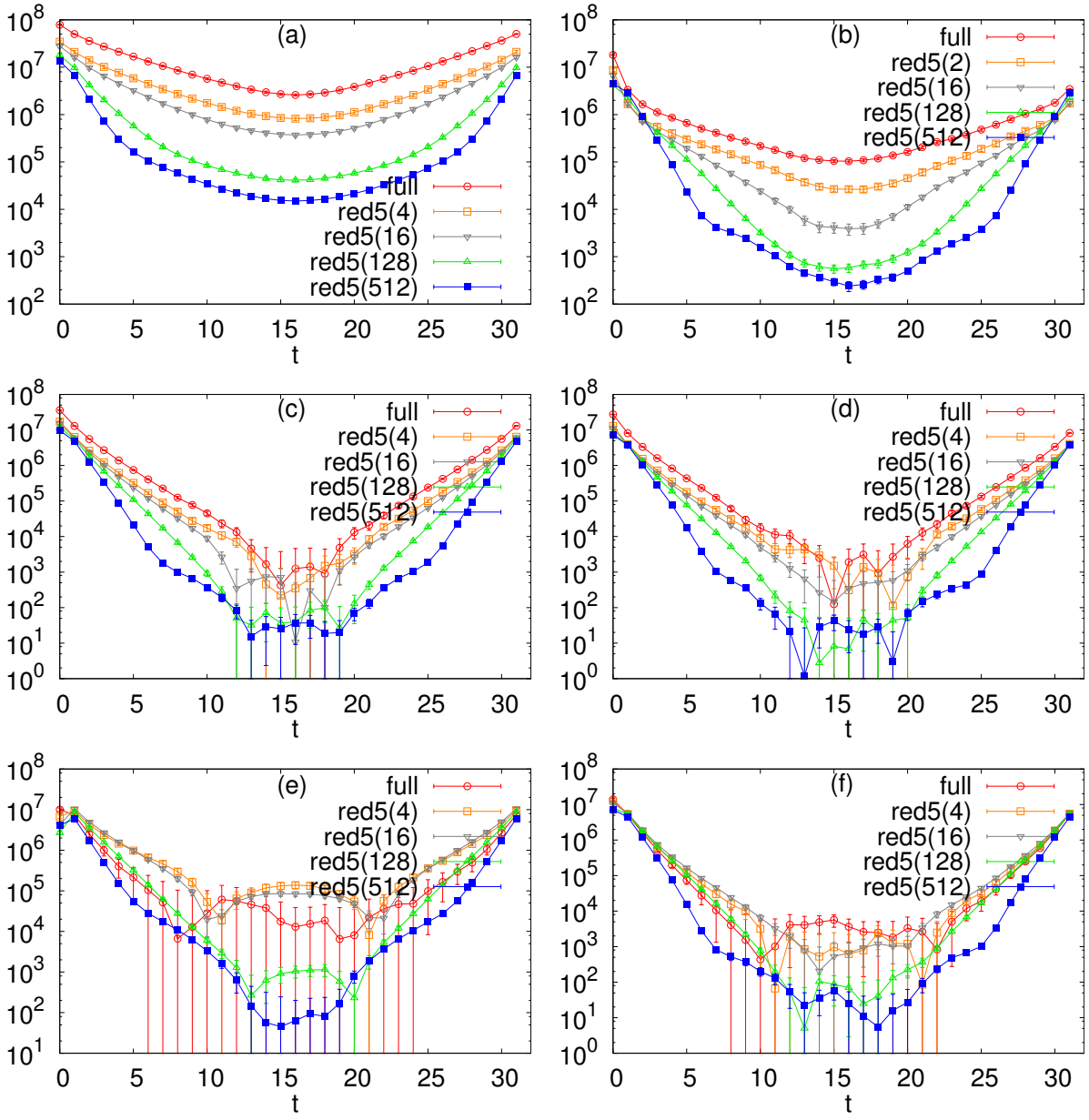

Figure 2.3: Correlation functions for the *reduced* interpolators as compared to the correlators from full propagators. Top: $J^{PC} = 0^{-+}$ with interpolators (a) $\overline{u}\gamma_5 d$, (b) $\overline{u}\gamma_4\gamma_5 d$. Middle: $J^{PC} = 1^{--}$ with (c) $\overline{u}\gamma_i d$, (d) $\overline{u}\gamma_4\gamma_i d$. Bottom: Reduced (e) $J^{PC} = 0^{++}$ ($\overline{u}d$) and (f) $J^{PC} = 1^{++}$ ($\overline{u}\gamma_i\gamma_5 d$).

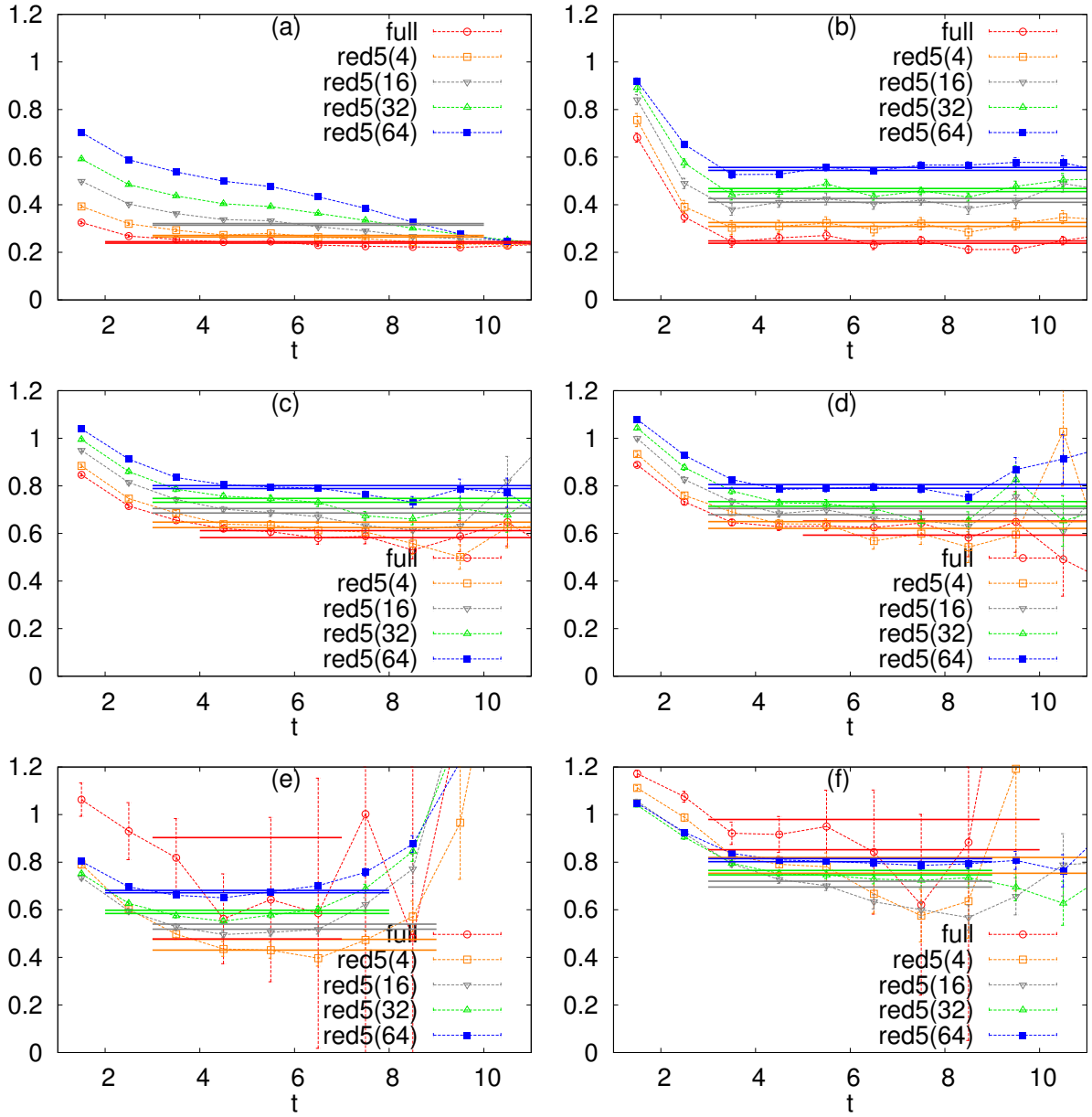

Figure 2.4: Effective mass plots for the *reduced* interpolators as compared to the full propagators. For the notation (a-f) see Fig. 2.3.

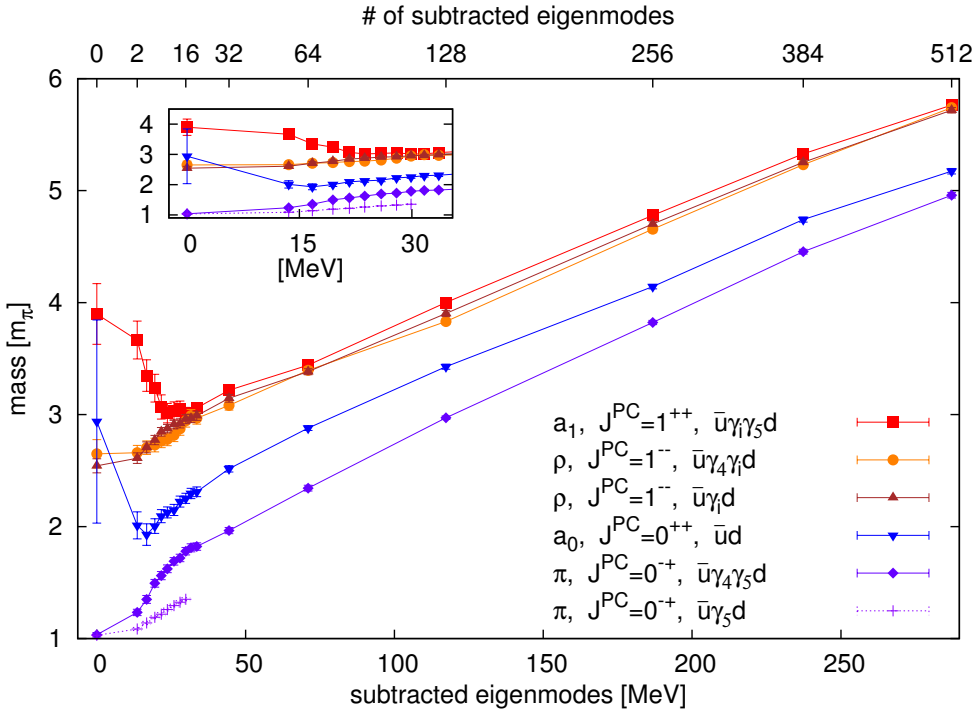

Figure 2.5: The masses of all considered mesons as a function of the reduced spectrum, subtracting the 0–512 lowest modes of D_5.

2.7 Conclusions

The low lying eigenvalues of the Dirac operator are usually associated with chiral symmetry breaking. We have computed hadron propagators while removing increasingly more of the low lying eigenmodes of the Dirac operator. This allows us to study their influence on certain hadron masses. Because of the relationship of the low eigensector with chiral symmetry breaking, this amounts to partially restoring chiral symmetry (in the valence quarks).

We find drastic behavior for some meson interpolators when starting to remove low eigenmodes. At truncation level 16 the behavior saturates and then the mass values rise uniformly with roughly parallel slopes. The confinement properties remain intact, i.e., we still observe clear bound states for most of the studied isovector (scalar, axial vector and vector) mesons. An exception is the pion, where no clear exponential decay of the correlation function is seen in the $\overline{u}\gamma_5 d$ interpolator, but a massive state is seen in the $\overline{u}\gamma_4\gamma_5 d$ interpolator. The mass values of the vector meson chiral partners a_1 and ρ approach each other rapidly when eight or more low modes are removed.

We conclude that essential confinement properties remain intact, even when the low eigenmodes of the Dirac operator are removed in the valence sector. Restoration of chiral symmetry is observed in that approximation.

Chapter 3

The chirally improved quark propagator and restoration of chiral symmetry

The present chapter was motivated by the desire to understand the fact that the masses of the mesons under Dirac low-mode truncation remained rather large as discussed in the previous chapter. It consists of the Letter

- [2] Mario Schröck, *"The chirally improved quark propagator and restoration of chiral symmetry"*, Phys. Lett. B **711** (2012) 217-224.

The mass function of the quark propagator in a gauge fixed setting exhibits the generation of a dynamical mass caused by the dynamical breaking of the chiral symmetry. Thus, it is expected that the dynamically generated mass vanishes under (artificial) chiral restoration. It is not clear *a priori* though, which effect the truncation has on the value of the bare quark mass. The bare quark mass is related to the absolute value of the smallest eigenvalues, hence removal of these small eigenvalues potentially increases the bare mass. Furthermore, it is of interest at which truncation level the chiral condensate completely vanishes. Although we found chiral symmetry to be restored after having subtracted ~ 16 Dirac eigenmodes, it is not understood if the chiral condensate is equal to zero at this stage or if a combined effect of partial removal of the chiral condensate and some effective restoration mechanism occurs.

3.0 Abstract

The chirally improved (CI) quark propagator in Landau gauge is calculated in two flavor lattice Quantum Chromodynamics. Its wave-function renormalization function $Z(p^2)$ and mass function $M(p^2)$ are studied. To minimize lattice artifacts, tree-level improvement of the

propagator and tree-level correction of the lattice dressing functions is applied. Subsequently the CI quark propagator under Dirac operator low-mode removal is investigated. The dynamically generated mass in the infrared domain of the mass function is found to dissolve continuously as a function of the reduction level and strong suppression of $Z(p^2)$ for small momenta is observed.

3.1 Introduction

The quark propagator is one of the fundamental objects in quantum chromodynamics (QCD). The mass function of the quark propagator reveals the value of the running quark mass in the deep ultraviolet (UV) where interactions are weak due to the asymptotic freedom of QCD. In the infrared (IR), the dynamical generation of mass which is associated with the spontaneous breaking of chiral symmetry is exhibited by the mass function. The IR is not accessible with perturbative methods; lattice QCD provides a nonperturbative *ab initio* approach to QCD and thus is a well adapted tool to study the IR physics of the strong nuclear force.

The quark propagator is a gauge dependent object and thus the gauge has to be fixed in order to study its properties; we adopt the manifestly Lorentz covariant Landau gauge for the present work. The Landau gauge quark propagator has been studied on the lattice with various fermionic actions. Some initial investigations using (improved) Wilson fermions have been reported in Refs. [67, 68]. A series of studies using standard Kogut–Susskind [69] and Asqtad [70] quarks found that staggered quarks are well suited to explore the properties of the quark propagator on the lattice [71, 72, 73, 74, 75, 76].

Lattice Dirac operators that fulfill the Ginsparg–Wilson (GW) equation allow for lattice fermions that have an exact chiral symmetry at nonzero lattice spacing. The overlap operator [43, 44] provides a solution to the GW equation. The quark propagator from the overlap action has been examined in [77, 78, 79, 80, 81, 82, 83]. The drawback of overlap fermions is their very high computational cost which renders them impractical for full dynamical simulations.

In this Letter we analyze the quark propagator from the so-called chirally improved (CI) Dirac operator [45, 46] which fulfills the GW equation not exactly, but only approximately. Nevertheless, the gain in simulation time of roughly one order of magnitude, in comparison to overlap fermions, allows for an investigation of the propagator on full dynamical configurations [59, 60]. The better chiral properties of the CI operator as opposed to Wilson's fermion action make it well suited to explore effects of spontaneous chiral symmetry breaking on the lattice.

Banks and Casher formulated a relation of the density of the smallest nonzero eigenvalues of the Dirac operator to the chiral condensate [51]. In [1] we have studied the effects of removing the lowest eigenmodes of the hermitian CI Dirac operator $\gamma_5 D_{\mathrm{CI}}$ on the meson spectrum and found signals for the restoration of chiral symmetry (the masses of the ρ and a_1 became approximately degenerate, cf. [66]) whereas confining properties persisted. The authors of [84]

expand the Wilson loop in terms of Dirac operator eigenmodes and detect that removing the lowest modes does not influence the static quark potential qualitatively.

A portion of this study aims at answering the question, how change the quark wave-function renormalization function $Z(p^2)$ and the quark mass function $M(p^2)$ under Dirac low-mode removal? It is expected that the mass function flattens out in the IR once chiral symmetry is restored. Yet another question of interest is how the Dirac eigenmode truncation level at which chiral symmetry was found to be approximately restored [1], compares to the loss of dynamical mass generation in $M(p^2)$ as a function of the truncation level.

The remainder of this work is as follows: in Sec. 3.2 we briefly summarize the defining equations of lattice Landau gauge fixing. In Sec. 3.3 we first remind the reader of the main steps in the construction of the D_{CI} operator, followed by a discussion of $Z(p^2)$ and $M(p^2)$ from the D_{CI} at tree-level and in the full interacting case. In order to reduce the dominant lattice artifacts we apply tree-level improvement and test a multiplicative and an hybrid scheme of tree-level correction. In Sec. 3.4 we investigate $Z(p^2)$ and $M(p^2)$ from the D_{CI} under Dirac low-mode removal and in Sec. 3.5 we summarize and conclude.

3.2 Gauge fixing

The continuum Landau gauge condition,

$$\partial_\mu A_\mu(x) = 0, \tag{3.1}$$

can be realized on the lattice by requiring the maximization of the gauge functional

$$F_g[U] = \mathfrak{Re} \sum_{\mu,x} \mathrm{tr}\big[U^g_\mu(x) + U^g_\mu(x-\hat{\mu})^\dagger\big] \tag{3.2}$$

with respect to gauge transformations $g(x) \in \mathrm{SU}(3)$ where

$$U^g_\mu(x) \equiv g(x) U_\mu(x) g(x+\hat{\mu})^\dagger. \tag{3.3}$$

The sum in Eq. (3.2) runs over the four Dirac components μ and all lattice sites x. Once such a gauge transformation is found, the discrete Landau gauge condition

$$\Delta(x) \equiv \sum_\mu \left(A_\mu(x) - A_\mu(x-\hat{\mu})\right) = 0 \tag{3.4}$$

holds, where $A_\mu(x)$ is recovered from the lattice gauge links $U_\mu(x)$ via

$$A_\mu(x) \equiv \left[\frac{U_\mu(x) - U_\mu(x)^\dagger}{2iag_0} \right]_{\text{traceless}} . \tag{3.5}$$

A measure for the achieved Landau gauge "quality" is given by

$$\theta \equiv \frac{1}{VN_c} \sum_x \text{tr} \left[\Delta(x) \Delta(x)^\dagger \right], \tag{3.6}$$

here the trace goes over the color indices, N_c is the number of colors and V is the number of lattice points. In the later discussion of the CI quark propagator we will choose $\theta < 10^{-10}$ as the stopping criterion for the gauge fixing algorithm.

We accelerate the costly task of lattice gauge fixing by utilization of the graphics processing unit (GPU) with NVIDIA® 's CUDA™ (Compute Unified Device Architecture) programming environment, as pointed out in the Appendix.[1]

For a general discussion of lattice gauge fixing and its problems we refer to [85].

3.3 The CI quark propagator

In the present section we analyze the lattice dressing functions from the CI quark propagator after having repeated the main steps in the construction of the CI Dirac operator.

3.3.1 The CI Dirac operator

The so-called chirally improved Dirac operator D_{CI} was introduced in [45] and first analyzed in [46] where also its spectral properties were studied. An initial quenched hadron spectroscopy using the D_{CI} was examined in [86] before dynamical configurations including two light degenerate CI quarks have been generated in order to calculate the hadron spectrum in a series of papers [87, 59, 60, 88]. Renormalization factors of quark bilinears of the D_{CI} were studied in [89, 90].

The CI Dirac operator is an approximate solution to the GW equation. It is constructed by expanding the most general Dirac operator in a basis of simple operators,

$$D_{\text{CI}}(x,y) = \sum_{i=1}^{16} c_{xy}^{(i)}(U) \Gamma_i + m_0 \mathbb{1}, \tag{3.7}$$

1 Not included in this thesis since its content became supersede by the later work [4] (Chap. 5).

where the sum runs over all elements Γ_i of the Clifford algebra. The coefficients $c_{xy}^{(i)}(U)$ consist of path ordered products of the link variables U connecting lattice sites x and y. Inserting this expansion into the GW equation then turns into a system of coupled quadratic equations for the expansion coefficients of the D_{CI} . That expansion provides for a natural cutoff which turns the quadratic equations into a simple finite system.

The ansatz is constructed such that all symmetries of the fermionic action are maintained and moreover γ_5-hermiticity is imposed. The so-called clover term [91] is included for $\mathcal{O}(a)$ improvement where the c_{sw} parameter is set to its tree-level value (one).

3.3.2 Configurations

For the analysis of the CI quark propagator we use 125 gauge field configurations [59, 60] of lattice size $16^3 \times 32$ and lattice spacing $a = 0.144(1)\,\mathrm{fm}$. The configurations include two light degenerate dynamical CI quark flavors with the mass parameter set to $m_0 = -0.077$ and a resulting bare AWI-mass of $m = 15.3(3)\,\mathrm{MeV}$. For the simulation of the gauge fields as well as for our valence quarks, paths up to length four are used in the ansatz Eq. (3.7) and the corresponding coefficients can be found in [59].

3.3.3 Nonperturbative quark propagator

The continuum quark propagator at tree-level reads

$$S^{(0)}(p) = (i\not{p} + m)^{-1} \tag{3.8}$$

where m is the bare quark mass. In a manifestly covariant gauge like Landau gauge, the interacting renormalized quark propagator $S(\mu; p)$ can be decomposed into Dirac scalar and vector parts

$$S(\mu; p) = \left(i\not{p}A(\mu; p^2) + B(\mu; p^2)\right)^{-1} \tag{3.9}$$

or equivalently as

$$S(\mu; p) = Z(\mu; p^2)\left(i\not{p} + M(p^2)\right)^{-1}. \tag{3.10}$$

In the last equation we introduced the wave-function renormalization function $Z(\mu; p^2) = 1/A(\mu; p^2)$ and the mass function $M(p^2) = B(\mu; p^2)/A(\mu; p^2)$.

On the lattice, the regularized quark propagator is calculated and consequently it depends on the cutoff a. The regularized quark propagator $S_L(p; a)$ can then be renormalized at the renormalization point μ with the momentum independent quark wave-function renormalization constant $Z_2(\mu; a)$,

$$S_L(p; a) = Z_2(\mu; a)S(\mu; p). \tag{3.11}$$

Whereas the mass function $M(p^2)$ is independent of the renormalization point μ (and equivalently of the cutoff scale a), the wave-function renormalization function $Z(\mu; p^2)$ differs at different scales but can be related from different scales by multiplication with a constant, i.e., by the ratio of the two different quark renormalization constants.

The momentum subtraction scheme (MOM) has the renormalization point boundary conditions $Z(\mu; \mu^2) = 1$ and $M(\mu^2) = m(\mu)$ where $m(\mu)$ becomes the running mass at large momenta.

Below we extract the nonperturbative functions $M(p^2)$ and $Z(p^2) \equiv Z_2(\mu; a)Z(\mu; p^2)$ directly from a lattice calculation as it was discussed in great detail in, e.g., Ref. [92]. We perform a cylinder-cut [67] on all our data and average over the discrete rotational and parity symmetries of $S_L(p; a)$ to increase the statistics.

3.3.4 The lattice quark propagator at tree-level

For the sake of easier notation we will suppress the a dependence of the lattice quark propagator and write $Z_L(p)$ and $M_L(p)$ as functions of p rather than p^2 in the following discussion.

The lattice quark propagator at tree-level $S_L^{(0)}(p)$ differs from the continuum case, Eq. (3.8), due to discretization artifacts,

$$S_L^{(0)}(p) = \left(ia\not{k} + aM_L^{(0)}(p) \right)^{-1} . \tag{3.12}$$

The dressing function $A_L^{(0)}(p)$ is by construction equal to one at tree-level (at least without tree-level improvement) and thus the function $B_L^{(0)}(p)$ equals at tree-level the mass function $M_L^{(0)}(p)$.

We extract the CI lattice momentum $ak(p)$ from the tree-level propagator on the lattice and depict it in Fig. 3.1. The result is consistent with the analytically derived expression for the D_{CI} momenta given in Appendix A.1.

The tree-level mass function $aM_L^{(0)}(p)$ which in the continuum equals the bare mass m, is shown in Fig. 3.2 (red crosses), again together with the corresponding analytical expression. We find that $aM_L^{(0)}(p)$ has a zero-crossing and $aM_L^{(0)}(0) \approx -0.333$. The latter value is trivially equal to the sum of all coefficients of Eq. (3.7) that come with a unit matrix in Dirac space

$$\sum_i s_i + m_0 \tag{3.13}$$

whereby the bare mass parameter is $m_0 = -0.077$ and the nonzero s_i are listed in Appendix A.1.

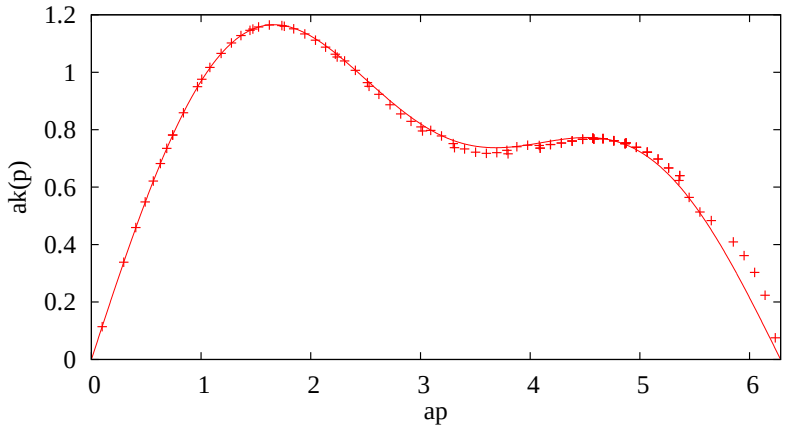

Figure 3.1: CI lattice momentum $ak(p)$ extracted from the tree-level propagator (crosses) compared with the analytical expression (full line) given in Appendix A.1.

3.3.5 The interacting propagator

We expect the interacting propagator to have a similar form to the continuum case Eq. (3.10), hence we write

$$S_L(p) = Z_L(p)\,(ia\not{k} + aM_L(p))^{-1}\,. \tag{3.14}$$

The functions $aM_L(p)$ and $Z_L(p)$ extracted from the lattice Monte Carlo simulation are shown in Fig. 3.2 and Fig. 3.3 (blue triangles), respectively. The shape of $aM_L(p)$ is similar to $aM_L^{(0)}(p)$ and also $Z_L(p)$ strongly deviates from the expected monotonically growing behavior, thus is clearly altered by discretization errors.

To get a handle on the lattice artifacts, i.e., to retain the shapes of the wave-function renormalization function and the mass function familiar from earlier lattice works as well as from Dyson-Schwinger equation studies [93], we discuss improvement and tree-level correction in the forthcoming subsections.

3.3.6 Improvement

The Symanzik improvement program [23] offers a systematic way to reduce the errors of the fermionic action to $\mathcal{O}(a^2)$. All terms that have the correct dimensionality and the symmetries

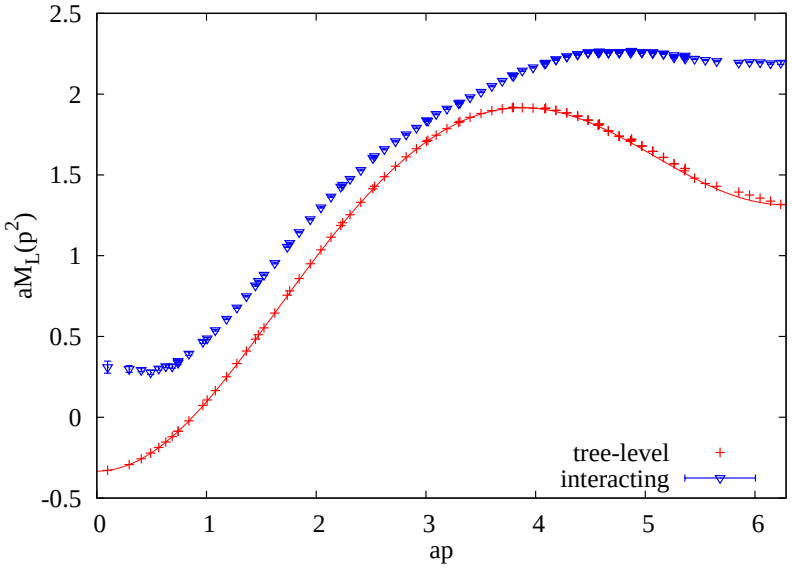

Figure 3.2: The lattice quark propagator mass function at tree-level (red crosses and full line) and in the unimproved full interacting case (blue triangles) without tree-level correction. The tree-level results comprise a lattice extraction from the tree-level D_{CI} (red crosses) and a plot of the analytical expression of the mass function (red line) given in Appendix A.1.

of the QCD fermionic Lagrangian must be included into the action:

$$L_1(x) = \overline{\psi}\sigma_{\mu\nu}F_{\mu\nu}\psi, \tag{3.15}$$

$$L_2(x) = \overline{\psi}\overrightarrow{D}_\mu\overrightarrow{D}_\mu\psi + \overline{\psi}\overleftarrow{D}_\mu\overleftarrow{D}_\mu\psi, \tag{3.16}$$

$$L_3(x) = m\,\mathrm{tr}\left[F_{\mu\nu}F_{\mu\nu}\right], \tag{3.17}$$

$$L_4(x) = m\left(\overline{\psi}\gamma_\mu\overrightarrow{D}_\mu\psi - \overline{\psi}\gamma_\mu\overleftarrow{D}_\mu\psi\right), \tag{3.18}$$

$$L_5(x) = m^2\overline{\psi}\psi. \tag{3.19}$$

The terms L_3 and L_5 can be accounted for by a redefinition of the bare parameters m and g. L_2 and L_4 are only needed for off-shell quantities like hadronic matrix elements or the quark propagator [94]. Thus for on-shell quantities it is sufficient to take the clover term [95] (which corresponds to L_1) into account.

Note that whereas exact GW fermions are automatically $\mathcal{O}(a)$ improved, the CI operator fulfills the GW equation only approximately and thus the clover term is included in the CI action.

Since the quark propagator is an off-shell quantity we would like to include the terms L_2 and L_4 as well. In [96] it is shown that at tree-level L_2 and L_4 can be eliminated by a transformation

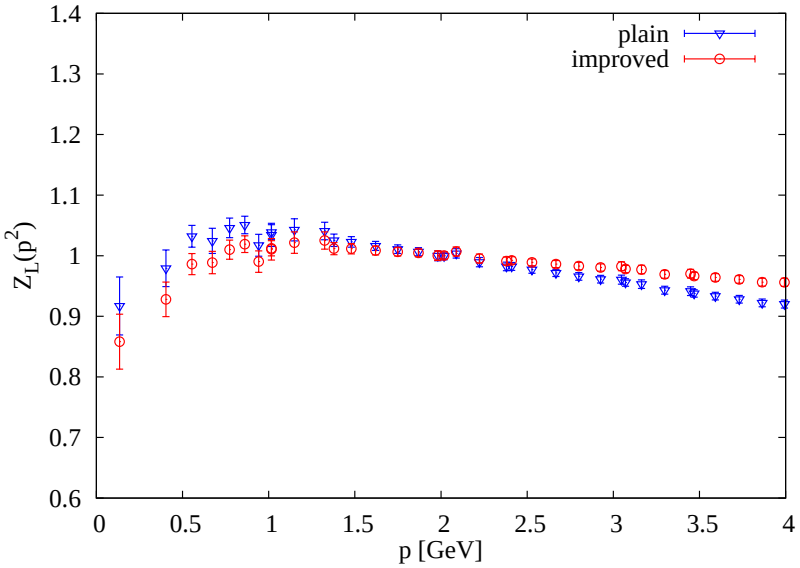

Figure 3.3: The wave-function renormalization function $Z_L(p)$ of the CI quark propagator: unimproved and without tree-level correction (blue triangles) and with tree-level improvement and tree-level correction (red circles). The renormalization point is set at $\mu = 2\,\mathrm{GeV}$.

of the fermion fields according to

$$\psi \to \left(1 + \frac{a}{4}m\right)\left(1 - \frac{a}{4}\gamma_\mu \overrightarrow{D}_\mu\right)\psi, \tag{3.20}$$

$$\overline{\psi} \to \left(1 + \frac{a}{4}m\right)\overline{\psi}\left(1 + \frac{a}{4}\gamma_\mu \overleftarrow{D}_\mu\right). \tag{3.21}$$

Improvement beyond tree-level requires tuning of the coefficients of the fermion field transformations [97] which we do not attempt. Hence we adopt the above fermion field transformations under which the quark propagator turns into [67, 68]

$$S_I(x,y) \equiv \left\langle (1 + am)S(x,y;U) - \frac{a}{2}\delta(x,y)\right\rangle \tag{3.22}$$

where the index I denotes improvement. In Eq. (3.22), $S(x,y;U)$ is obtained by inverting the D_{CI} operator on each configuration and the brackets denote Monte Carlo integration over the gauge fields U.

All results that follow have been tree-level improved according to the above prescription.

3.3.7 Tree-level correction

In order to blank out the lattice artifacts which are already present at tree-level, we now focus on the derivation of the interacting propagator from its tree-level form.

For the renormalization function $Z_L(p)$ we adopt a multiplicative tree-level correction

$$Z_L(p) \to \frac{Z_L(p)}{Z_L^{(0)}(p)}. \tag{3.23}$$

As can be seen in Fig. 3.3 (red circles), this procedure together with the tree-level improvement from the previous subsection flattens $Z_L(p)$, hence reduces the dominant lattice artifacts. However, the fact that the function is still not monotonically growing indicates that the improvement coefficients are not sufficiently adjusted to remove all $\mathcal{O}(a)$ errors when simply picking their tree-level values.

In order to apply a multiplicative tree-level correction to the mass function of the form

$$aM_L(p) \to \frac{amM_L(p)}{M_L^{(0)}(p)} \tag{3.24}$$

we have to carry out an additive mass renormalization of the tree-level function $B_L^{(0)}(p)$ in order to avoid divergences, i.e.,

$$aB_L^{(0)}(p) \to aB_L^{(0)}(p) + am_{\text{add}} \tag{3.25}$$

where am_{add} is chosen such that $B_L^{(0)}(0) = m$, like in the continuum, thus

$$am_{\text{add}} = am - aB_L^{(0)}(0) \approx 0.344. \tag{3.26}$$

As a result, the multiplicative tree-level correction for the mass function is

$$aM_L(p) \to \frac{amM_L(p)A_L^{(0)}(p)}{B_L^{(0)}(p) + m_{\text{add}}}. \tag{3.27}$$

Alternatively, we may adopt an hybrid tree-level correction which is based on the ideas developed in Ref. [68]: if $p < p'$, then perform an additive tree-level correction

$$aM_L(p) \to aM_L(p) - \frac{aB_L^{(0)}(p) + am_{\text{add}}}{A_L^{(0)}(p)} \tag{3.28}$$

and for momenta larger than p' apply a multiplicative tree-level correction

$$aM_L(p) \to \frac{amM_L(p)A_L^{(0)}(p)}{B_L^{(0)}(p)}. \tag{3.29}$$

The momentum parameter p' should be adjusted thereby such that $M_L(p)$ is continuous and smooth at $p = p'$ which we found to be the case for $p' = 1.5\,\text{GeV}$.

Both possibilities of tree-level correction for the mass function $M_L(p)$ are plotted in Fig. 3.4. We observe that the pure multiplicative correction (blue crosses) results in an infrared enhanced function, enhancement occurring from 1.25 GeV on downwards and appearing to be rather steep. The hybrid scheme (red circles), on the other hand, exhibits a wider range of IR mass generation (from 2.5 GeV on downwards), gives a higher IR mass and yields flattening of the mass function in the deep IR. The hybrid scheme allows for an earlier mass generation due to the fact that the multiplicative correction therein (for $p \geq p'$) does not require an additive mass renormalization since the zero-crossing of the tree-level function is handled by the additive tree-level correction ($p < p'$).

When comparing these results with lattice quark propagator studies from a different fermionic action, for example to the (quenched) overlap quark propagator [77, 78, 79, 80, 81, 82, 83], we find better agreement for the hybrid scheme. It has to be stressed however that the parameter p' introduces a small arbitrariness to the procedure whereas the simpler pure multiplicative scheme provides a straightforward comparison of the interacting mass function with its tree-level counterpart while still yielding *qualitatively* the correct physics. Consequently, for the next section we adopt the simpler multiplicative scheme for the analysis of the effects of Dirac low-mode removal on the quark propagator mass function in order to avoid possible systematic errors related to the tuning of p'.

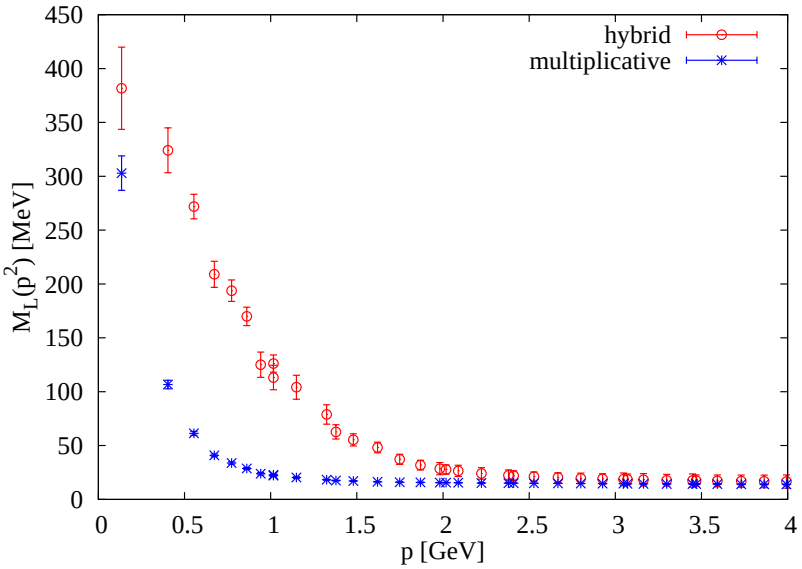

Figure 3.4: The CI quark propagator mass function $M_L(p)$ after improvement and application of a pure multiplicative (blue crosses) and an hybrid (red circles) tree-level correction procedure.

3.4 Restoration of chiral symmetry

The lowest Dirac eigenmodes are known to play a crucial role for dynamical chiral symmetry breaking as stated by the Banks–Casher relation [51]. The latter relates the chiral condensate to the density of the smallest nonzero Dirac eigenmodes. As a consequence, when removing the Dirac eigenmodes near the origin from the theory, the chiral condensate vanishes and chiral symmetry becomes "artificially restored" [1].

The aim of the current work is to analyze the effects of artificial chiral restoration on the dressing functions of the quark propagator. Consider the hermitian Dirac operator $D_5 \equiv \gamma_5 D$ which is normal and thus has real eigenvalues μ_i. D can be written in terms of the spectral representation of D_5,

$$D = \sum_{i=1}^{N} \mu_i \, \gamma_5 \, |v_i\rangle \, \langle v_i| \, . \tag{3.30}$$

We split the quark propagator $S = D^{-1}$ into a low-mode part (lm) and a reduced part (red), e.g., using the eigenvalues and eigenvectors of D_5,

$$S = \sum_{i \leq k} \mu_i^{-1} \, |v_i\rangle \, \langle v_i| \, \gamma_5 + \sum_{i>k} \mu_i^{-1} \, |v_i\rangle \, \langle v_i| \, \gamma_5 \tag{3.31}$$

$$\equiv S_{\mathrm{lm}(k)} + S_{\mathrm{red}(k)}. \tag{3.32}$$

Hence we can obtain the reduced part of the propagator by subtracting the low-mode part from the full propagator

$$S_{\mathrm{red}(k)} = S - S_{\mathrm{lm}(k)}. \tag{3.33}$$

We calculate the quark wave-function renormalization function $Z_L(p)$ and the quark mass function $M_L(p)$ from the reduced propagators of Eq. (3.33) with varying reduction levels $k = 2 - 512$. We tree-level improve the modified propagators and apply the multiplicative tree-level correction scheme, cf. Sec. 3.3. The dressing functions from reduced propagators are presented in Fig. 3.5 and Fig. 3.6.

Figure 3.5 reveals amplification of IR suppression of $Z_L(p)$ when subtracting Dirac low-modes whereas the range from medium to high momenta is not altered at all. The mass function $M_L(p)$, Fig. 3.6, demonstrates a similar behavior: it gets suppressed in the IR when removing more and more eigenmodes until the dynamic generation of mass completely ceases at truncation stage $k \approx 128$.

In Fig. 3.7 we compare the deep IR mass of the CI quark propagator from $M_L(p^2_{\mathrm{min}})$, at the smallest available momentum $p_{\mathrm{min}} = 0.1345\,\mathrm{GeV}$, as a function of the reduction level with the mass splitting of the vector meson ρ and its chiral partner the axial vector current a_1, taken

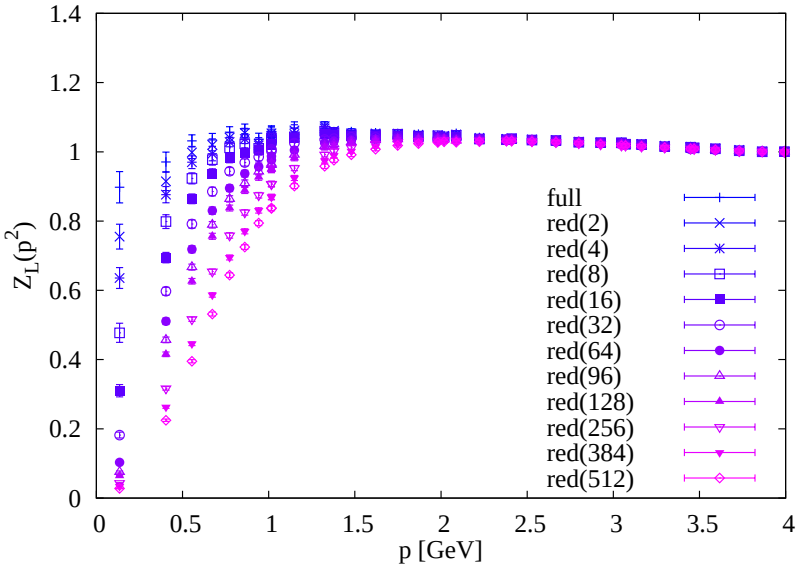

Figure 3.5: The quark wave-function renormalization function $Z_L(p)$ under Dirac eigenmode removal for different reduction levels k. The renormalization point is set at $\mu = 4\,\mathrm{GeV}$.

from Ref. [1]. Note that the reduction level k can be translated to an energy scale which is given in the lower abscissa of the figure and was derived in [1] by integrating the histograms of the eigenvalues.

The mass splitting between the ρ and the a_1 rapidly drops down and reaches a plateau after subtracting about 16 eigenmodes; it does not go down to zero which can most likely be attributed to the small explicit chiral symmetry breaking by the nonvanishing quark mass. In contrast, the dynamically generated mass of the quark propagator, $M_L(p^2_{\mathrm{min}})$, decreases slower and reaches its plateau only after subtracting more than 128 Dirac eigenmodes.

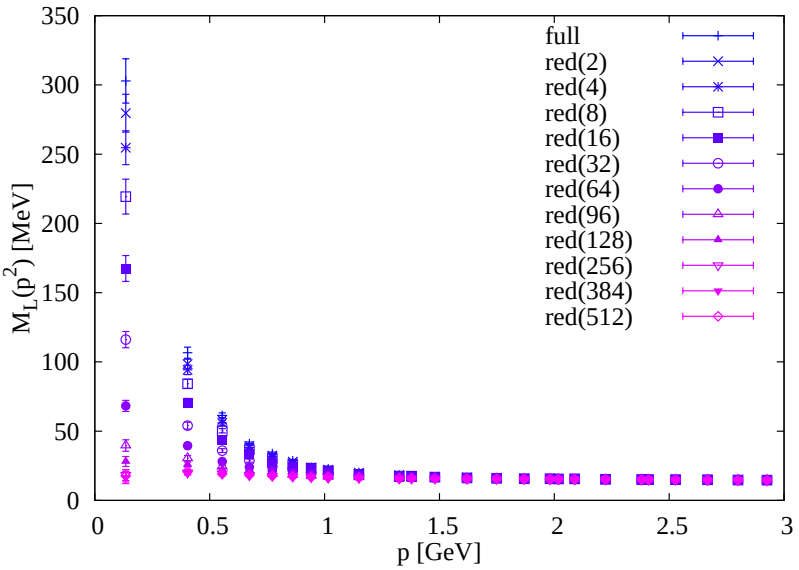

Figure 3.6: The quark mass function $M_L(p)$ under Dirac eigenmode removal for different reduction levels k.

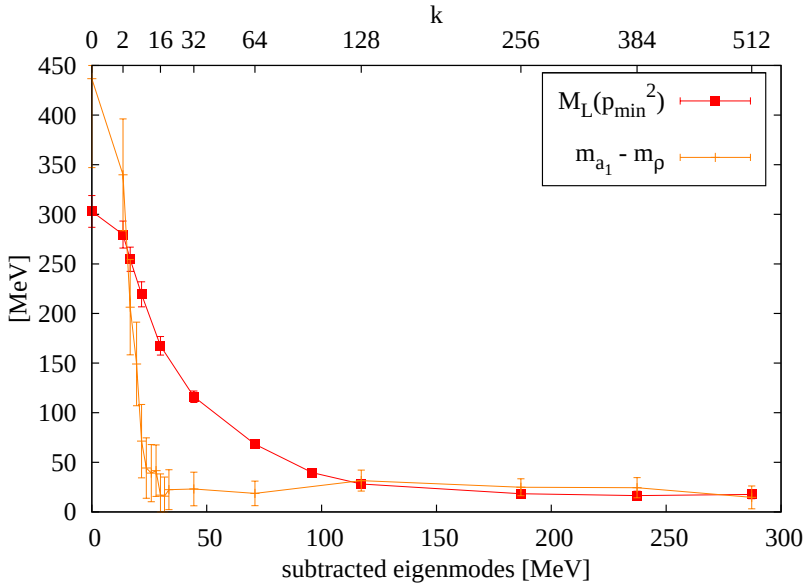

Figure 3.7: The infrared mass $M_L(p^2_{\text{min}})$ of the reduced CI quark propagator as a function of the reduction level compared with the mass splitting between the ρ and the a_1 from Ref. [1]. The upper abscissa shows the truncation level k and the lower abscissa gives the corresponding energy scale, the relation between the two is obtained by integrating the histograms of the D_5 eigenvalues.

3.5 Conclusions

The wave-function renormalization function $Z(p^2)$ and the mass function $M(p^2)$ from the CI quark propagator have been analyzed on configurations with two light degenerate CI quark flavors. It has been demonstrated that the combination of tree-level improvement and a multiplicative or hybrid tree-level correction scheme drastically reduce the dominant lattice artifacts.

Removing the lowest Dirac eigenmodes out of the quark propagator strongly suppresses the wave-function renormalization function in the IR and completely dissolves the dynamically generated mass displayed by $M(p^2)$. Under Dirac low-mode removal, the mass function is found to reveal a smoother transition towards chiral restoration than the splitting of the vector and axial vector currents.

Chapter 4

Symmetries of hadrons after unbreaking the chiral symmetry

In Chap. 2 only ground states of the scalar, pseudoscalar, vector and axial vector mesons under Dirac low-mode removal have been studied. In this chapter, which includes the publication

- [3] L. Ya. Glozman, C. B. Lang, M. Schröck, *"Symmetries of hadrons after unbreaking the chiral symmetry"*, Phys. Rev. D **86** (2012) 014507,

we extend the investigation in the following way: first, the variational analysis method (Sec. 1.1.4) is adopted in order to enable us to obtain the evolution of correlator functions and effective masses of the tensor meson b_1 and some excited states of the previously studied mesons. Second, we include baryons in our analysis, in particular the nucleon and Δ of positive and negative parity, respectively.

4.0 Abstract

We study hadron correlators upon artificial restoration of the spontaneously broken chiral symmetry. In a dynamical lattice simulation we remove the lowest lying eigenmodes of the Dirac operator from the valence quark propagators and study evolution of the hadron masses obtained. All mesons and baryons in our study, except for a pion, survive unbreaking the chiral symmetry and their exponential decay signals become essentially better. From the analysis of the observed spectroscopic patterns we conclude that confinement still persists while the chiral symmetry is restored. All hadrons fall into different chiral multiplets. The broken $U(1)_A$ symmetry does not get restored upon unbreaking the chiral symmetry. We also observe signals of some higher symmetry that includes chiral symmetry as a subgroup. Finally, from comparison

of the $\Delta - N$ splitting before and after unbreaking of the chiral symmetry we conclude that both the color-magnetic and the flavor-spin quark-quark interactions are of equal importance.

4.1 Introduction

Highly excited hadrons in the u, d sector reveal some parity doubling [98, 99, 100, 57, 58, 66, 101, 102, 103, 104] and possibly some higher symmetry. It was conjectured that this parity doubling reflects effective restoration of chiral symmetry, i.e., insensitivity of the hadron mass generation mechanism to the effects of chiral symmetry breaking in the vacuum [98, 99, 100, 57, 58, 66]. Whether this conjecture is correct or not can be answered experimentally since the conjectured symmetry requires existence of some not yet observed states.

Recent and most complete experimental analysis on highly excited nucleons that includes not only elastic πN, but also the photoproduction data, does report evidence for some of the missing states and the parity doubling patterns look now even better than before [105].

The question of a possible symmetry in hadron spectra is one of the central questions for QCD since it would help to understand dynamics of confinement and chiral symmetry breaking as well as their role for the hadron mass generation.

Another "experimental" tool to address the issue of the hadron mass generation is lattice QCD. Equipped with the QCD Lagrangian and Monte Carlo techniques, one can calculate, at least in principle, hadron masses and other hadron properties from first principles. Enormous progress has been achieved for the hadron ground states. The problem of excited states, especially above the multihadron thresholds like πN, $\Delta\pi$, $\pi\pi$, $\pi\rho$, ... turns out to be much more difficult and demanding than was initially anticipated. When it is solved lattice results should reproduce experimental patterns and possibly indicate some still missing states.

Still, the mass of a hadron by itself, obtained from the experiment or from the lattice simulations, tells us not so much about the physics which is behind the mass generation. The pattern of all hadrons, on the contrary, could shed some light on the underlying dynamics if there are some obvious symmetries in the pattern or if its regularities can be systematically explained.

The most interesting issue is to get some insight on how QCD "works" in some important cases and understand the underlying physical picture. In this sense one can use lattice QCD as a tool to explore the interrelations between confinement and chiral symmetry breaking. In particular, we can ask the question whether hadrons and confinement will survive after having artificially removed the quark condensate of the vacuum. This can be achieved via removal of the low lying eigenmodes of the Dirac operator, which is a well defined procedure [16, 19].

In the past mainly the opposite was explored. After suggestions within the instanton liquid model [53] the effect of the low lying chiral modes on the ρ and other correlators was studied

on the lattice. In a series of papers [14, 106, 15, 16] it was shown that low-modes saturate the pseudoscalar and axial vector correlators at large distances and do not affect the part where high-lying states appear. In [16, 17] low-mode saturation and also effects of low-mode removal for mesons were studied for quenched configurations with the overlap Dirac operator [43, 44]. Subsequently low-modes were utilized to improve the convergence of the determination of hadron propagators [16, 17, 18, 54, 55, 56] studying the efficiency when using the low-modes of the Dirac operator or the hermitian Dirac operator.

We are studying the complementary case, i.e., removal of the low-modes and we will refer to this as "unbreaking" the chiral symmetry. This issue has been addressed in a recent paper [1, 5] where the low lying eigenmodes of the Dirac operator have been removed from the quark Green's function and masses of the lowest mesons π,ρ,a_0 and a_1 have been calculated with such truncated quark propagators. The truncated Landau gauge quark propagator itself has been investigated in [2] where the loss of dynamical mass generation in the infrared sector of the propagator has been demonstrated.

After the unbreaking of the chiral symmetry the signal from the π-meson, obtained with the pseudoscalar quark-antiquark operator, disappears, which is consistent with the (pseudo) Goldstone boson nature of the pion. Indeed, with the artificially restored chiral symmetry there cannot be Goldstone bosons. What is very interesting, is that other low lying mesons survive and the quality of their signals become even essentially better after extraction of the low lying eigenmodes of the Dirac operator, responsible for chiral symmetry breaking. The very fact that hadrons survive the unbreaking of the chiral symmetry tells that there is confinement in the system even without the quark condensate. (A similar behavior was found in [84, 107], where the effect of such a removal on the static quark potential was studied.)

After extraction of the quark condensate the lowest-lying ρ and a_1 mesons demonstrate restoration of the chiral symmetry - they become degenerate - and their mass is rather large. This disproves a rather popular assertion that, e.g., the ρ-mass is entirely due to the quark condensate of the vacuum. As a physical implication we should then not expect a drop off the ρ-mass in a dense medium, which is a very popular issue both theoretically and experimentally for the last two decades [108]. This result should also be of importance for a debated issue of confining but chirally symmetric matter at low temperatures and large density [109, 110, 111, 112].

The conclusion of [1] about survival of confinement after unbreaking of the chiral symmetry was obtained on the limited basis of the lowest-lying mesons. In order to see it more clearly we need to extend the number of extracted states, in particular to include radially and orbitally excited hadrons (following quark model terminology). Consequently, we now add the b_1 and ρ' states to the above mentioned list of mesons. We limit ourselves only to the isovector mesons since the isoscalar mesons would require inclusion of disconnected graphs, which is numerically very costly.

Most importantly, we study behavior of the ground and excited positive and negative parity states in the N and Δ spectra. The baryonic states add additional information about existence or nonexistence of confinement. They do allow to see that confinement does survive after the restoration of chiral symmetry. Second, we see some traces of the higher symmetry, higher than simply $SU(2)_R \times SU(2)_L$. This observation may be related with the higher symmetry seen in the highly excited hadrons.

Our paper is organized as follows. In the next section we remind on the connection between low eigenmodes of the Dirac operator and the quark condensate in the vacuum. We discuss some basic aspects of removal of Dirac eigenmodes from the quark propagator. In Sect. 4.3 we present the details of the lattice simulation. The fourth section is devoted to the description of the baryon and meson interpolators used for our study of hadrons. In Sect. 4.5 we show and analyze the results and draw conclusions. Finally, in the last section, we briefly summarize our main observations.

4.2 The quark condensate and the Dirac operator

The lowest eigenmodes of the Dirac operator are related (in the chiral limit) to the quark condensate of the vacuum. This is encoded in the Banks–Casher relation [51]

$$< 0|\bar{q}q|0 >= -\pi\rho(0) \ , \tag{4.1}$$

where $\rho(0)$ is a density of the lowest quasi-zero eigenmodes of the Dirac operator. Here the sequence of limits is important: first, the infinite volume limit at finite quark mass is assumed and then the chiral limit should be taken. The opposite sequence would produce no chiral condensate as in the finite volume there cannot be any spontaneous breaking of chiral symmetry.

All lattice calculations are performed on a lattice of a finite volume. In the finite lattice volume the spectrum of the Dirac operator is discrete and the energy of the lowest nonzero mode of the Dirac operator is finite. Consequently, the quark condensate is strictly speaking zero. However, increasing the lattice volume the gap in the spectrum of the eigenmodes becomes smaller and smaller and the density of the lowest nonzero eigenmodes increases. A well defined limit of this density scaling exists: the number of such eigenvalues in a given interval adjacent to the real axis scales with the lattice volume. (In [113] is is argued[1] that the number of relevant eigenvalues should scale proportional the square root of the number of lattice points.)

In [56, 1] it was established that the eigenmodes of the hermitian Dirac operator $D_5 \equiv \gamma_5 D$ result in a faster saturation of the pseudoscalar correlator when approximating quark propagators

1 We thank Kim Splittorff for pointing us to that reference

by the lowest eigenmodes only, compared with the eigenmodes of the Dirac operator D. Therefore, we focus on reducing the quark propagators in terms of eigenmodes of D_5 rather than D.

From the lattice calculations in a given finite volume we cannot say a priori which and how many lowest eigenmodes of the Dirac operator are responsible for the quark condensate of the vacuum. For the overlap operator the real eigenvalues correspond to exact chiral modes, the zero modes (instantons); for Wilson-type operators one may associate real eigenvalues with zero modes. Their weight is suppressed in the infinite volume limit. The Banks-Casher relation, however, relies only on the density of nonzero modes. For the hermitian Dirac operator D_5 there is no simple method to distinguish between the real modes of the D and its small, but complex modes. In [1, 5] we discuss the integral over the distribution of the (real) eigenvalues of D_5. There we observe a transition region up to roughly twice the size of the quark mass corresponding to $\mathcal{O}(16-32)$ eigenmodes, as also observed in, e.g., [62, 63, 64, 65].

We follow the procedure to remove an increasing number of the lowest Dirac modes and study the effects of the (remaining) chiral symmetry breaking on the masses of hadrons. To be specific, we construct reduced quark propagators

$$S_{\mathrm{red5}(k)} = S - S_{\mathrm{lm5}(k)} \equiv S - \sum_{i \leq k} \mu_i^{-1} |v_i\rangle\langle v_i|\gamma_5 \ , \tag{4.2}$$

where S is the standard quark propagator obtained from the inversion of the Dirac operator, the μ_i are the (real) eigenvalues of D_5, $|v_i\rangle$ are the corresponding eigenvectors and k represents the reduction parameter which will be varied from $0-128$.

Note that the low-mode contribution (lm) of the quark propagators, $S_{\mathrm{lm5}(k)}$, must act on the same quark sources as S, see discussion below.

4.3 The setup

4.3.1 Dirac operator

For the dynamical quarks of our configurations as well as for the valence quarks of our study the so called chirally improved (CI) Dirac operator [45, 46] has been used. The latter represents an approximate solution to the Ginsparg–Wilson equation and therefore offers better chiral properties than the Wilson Dirac operator while being less expensive, in terms of computation time, in comparison to the chirally exact overlap operator.

4.3.2 Gauge configurations

We performed our study on 161 gauge field configurations [59, 60] that were generated for two degenerate dynamical light CI fermions with a corresponding pion mass $m_\pi = 322(5)\,\mathrm{MeV}$. The lattice size is $16^3 \times 32$ and the lattice spacing $a = 0.144(1)\,\mathrm{fm}$.

4.3.3 Quark source smearing

In order to obtain quark propagators, the Dirac operator has to be inverted on given quark sources. To improve the signal in hadron correlators, extended sources of Gaussian form [31, 32] instead of point sources are being used. Using several different extended sources allows for a larger operator basis in the variational method [34, 33, 114]. We use three different kinds of sources: narrow (0.27 fm) and wide (0.55 fm) sources, which are approximately of Gaussian shape, and a derivative source.

The narrow (wide) sources will be denoted by a subscript n (w) of the quark fields and the derivative source by ∂_i, respectively. The details of the calculation of the smeared quark sources are given in [60].

4.3.4 Variational method

In order to disentangle the excited states from the ground state (and also to provide cleaner signals for the ground states) we use the variational method [34, 33]. One computes cross-correlators $C_{ik}(t) = \langle O_i(t) O_k(0)^\dagger \rangle$ between several different lattice interpolators and solves the generalized eigenvalue problem

$$C(t)\boldsymbol{u}_n(t) = \lambda_n(t) C(t_0)\boldsymbol{u}_n(t)\ , \tag{4.3}$$

in order to approximately recover the energy eigenstates $|n\rangle$. The eigenvalues allow us to get the energy values $\lambda_n(t) \sim \exp(-E_n\, t)$ and the eigenvectors serve as fingerprints of the states, indicating their content in terms of the lattice interpolators. In our plots we show $\lambda_n(t)$, the effective masses $E_n(t) = \log(\lambda_n(t)/\lambda_n(t+1))$ and the t- dependence of the eigenvectors in order to verify the state identification. The quality of the results depends on the statistics and the provided set of lattice operators (for a discussion see [60]). The used interpolators are discussed in Sect. 4.4.

4.3.5 Dirac eigenmodes

On the given gauge field configurations we calculated the lowest 128 eigenmodes of the hermitian Dirac operator D_5 using ARPACK which is an implementation of the Arnoldi method to calculate

a part of the spectrum of arbitrary matrices [61].

Once the eigenmodes have been calculated and the quark propagators S have been obtained by inverting the Dirac operator on the three types of sources mentioned in Sec. 4.3.3, we can construct the reduced propagators $S_{\mathrm{red5}(k)}$ according to (4.2) after multiplying the low-mode part of the propagator, $S_{\mathrm{lm5}(k)}$, with the same three source types, respectively.

4.4 Hadron interpolators

Here we list the baryons and mesons we studied under Dirac low-mode reduction and give the interpolating fields for each individual.

4.4.1 Baryons

We analyze the nucleon and Δ baryons both with positive and negative parity. For the interpolators we use Gaussian smeared quark sources (n and w). For the nucleon we adopt three different Dirac structures, resulting in 18 interpolators (see Tab. 4.1) where we left out those operators that are similar to other ones due to isospin symmetry. The construction of the nucleon interpolators is given by

$$N^{(i)} = \varepsilon_{abc}\, \Gamma_1^{(i)}\, u_a \left(u_b^T\, \Gamma_2^{(i)}\, d_c - d_b^T\, \Gamma_2^{(i)}\, u_c\right) . \tag{4.4}$$

For the Δ,

$$\Delta_k = \varepsilon_{abc}\, u_a \left(u_b^T\, C\, \gamma_k\, u_c\right) , \tag{4.5}$$

we use only one Dirac structure and the six corresponding interpolators are listed in Tab. 4.2. We use parity projection for all baryons and Rarita-Schwinger projection for the Δ [60]. The sink interpolators are also projected to zero spatial momentum.

4.4.2 Mesons

We investigate isovector mesons of spin 1. Isoscalars require the calculation of disconnected graphs which are computationally too demanding for the type of fermion action used. The scalar meson a_0 as well as the pseudoscalar pion was studied already in [1].

Thus, the studied nonexotic channels are the J^{PC} combinations 1^{--} (ρ), 1^{++} (a_1) and 1^{+-} (b_1). For the analysis of the mesons we include derivative sources [115] in the construction of the interpolators to provide a large operator basis for the variational method. In Table 4.3 we list only those interpolators explicitly whose combination resulted in a good signal in practice when plugged into the variational method. The sink interpolators are projected to zero spatial momentum. A more complete list of possible interpolating fields is given in [60, 88].

$\chi^{(i)}$	$\Gamma_1^{(i)}$	$\Gamma_2^{(i)}$	smearing	$\#_N$
$\chi^{(1)}$	$\mathbb{1}$	$C\gamma_5$	$(nn)n$	1
			$(nn)w$	2
			$(nw)n$	3
			$(nw)w$	4
			$(ww)n$	5
			$(ww)w$	6
$\chi^{(2)}$	γ_5	C	$(nn)n$	7
			$(nn)w$	8
			$(nw)n$	9
			$(nw)w$	10
			$(ww)n$	11
			$(ww)w$	12
$\chi^{(3)}$	$i\mathbb{1}$	$C\gamma_t\gamma_5$	$(nn)n$	13
			$(nn)w$	14
			$(nw)n$	15
			$(nw)w$	16
			$(ww)n$	17
			$(ww)w$	18

Table 4.1: Interpolators for the N channel. The Dirac structures $\chi^{(i)}$, the quark smearings and the corresponding interpolator numbers $\#_N$ are given.

smearing	$\#_\Delta$
$(nn)n$	1
$(nn)w$	2
$(nw)n$	3
$(nw)w$	4
$(ww)n$	5
$(ww)w$	6

Table 4.2: Interpolators for the Δ channel. The quark smearings and the corresponding interpolator numbers $\#_\Delta$ are given.

$\#_\rho$	interpolator(s)
1	$\overline{a}_n\gamma_k b_n$
8	$\overline{a}_w\gamma_k\gamma_t b_w$
12	$\overline{a}_{\partial_k} b_w - \overline{a}_w b_{\partial_k}$
17	$\overline{a}_{\partial_i}\gamma_k b_{\partial_i}$
22	$\overline{a}_{\partial_k}\varepsilon_{ijk}\gamma_j\gamma_5 b_w - \overline{a}_w\varepsilon_{ijk}\gamma_j\gamma_5 b_{\partial_k}$
$\#_{a_1}$	interpolator(s)
1	$\overline{a}_n\gamma_k\gamma_5 b_n$
2	$\overline{a}_n\gamma_k\gamma_5 b_w + \overline{a}_w\gamma_k\gamma_5 b_n$
4	$\overline{a}_w\gamma_k\gamma_5 b_w$
$\#_{b_1}$	interpolator(s)
6	$\overline{a}_{\partial_k}\gamma_5 b_n - \overline{a}_n\gamma_5 b_{\partial_k}$
8	$\overline{a}_{\partial_k}\gamma_5 b_w - \overline{a}_w\gamma_5 b_{\partial_k}$

Table 4.3: Interpolators for (top) the ρ-meson, $J^{PC} = 1^{--}$, (middle) the a_1-meson, $J^{PC} = 1^{++}$, and (bottom) the b_1-meson, $J^{PC} = 1^{+-}$. The first column shows the number, the second shows the explicit form of the interpolator. The numbers refer to the classification in [88].

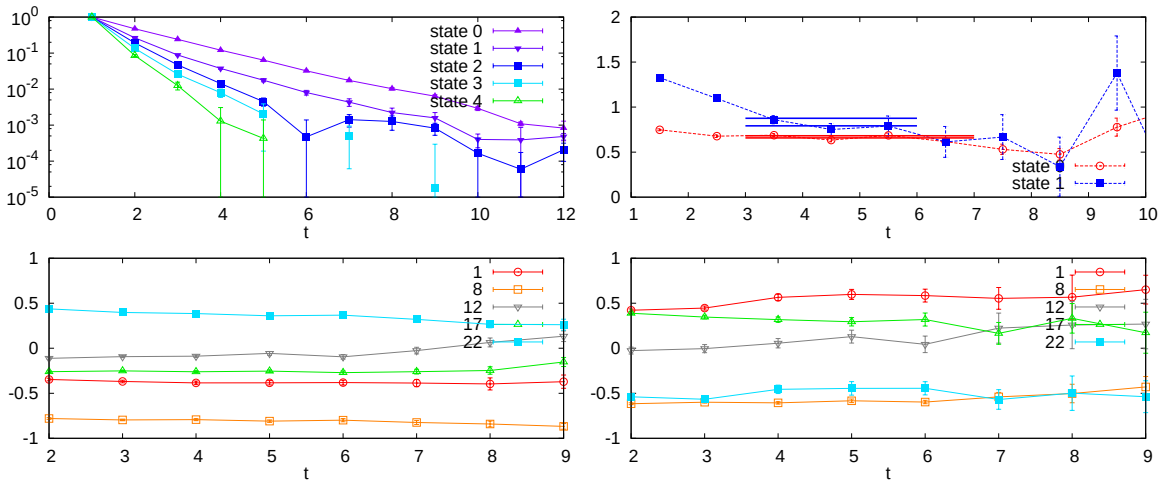

Figure 4.1: ρ with 12 eigenmodes subtracted: The correlators for all eigenstates (upper left), effective mass plot for the two lowest states (upper right), eigenvectors corresponding to the ground state (lower left). and 1st excited state (lower right).

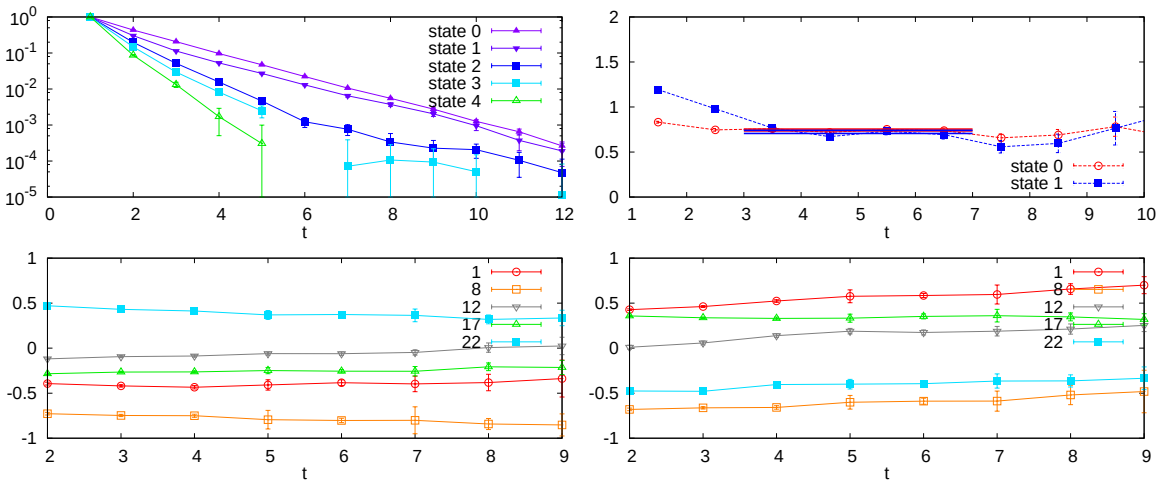

Figure 4.2: ρ with 32 eigenmodes subtracted: The correlators for all eigenstates (upper left), effective mass plot for the two lowest states (upper right), eigenvectors corresponding to the ground state (lower left). and 1st excited state (lower right).

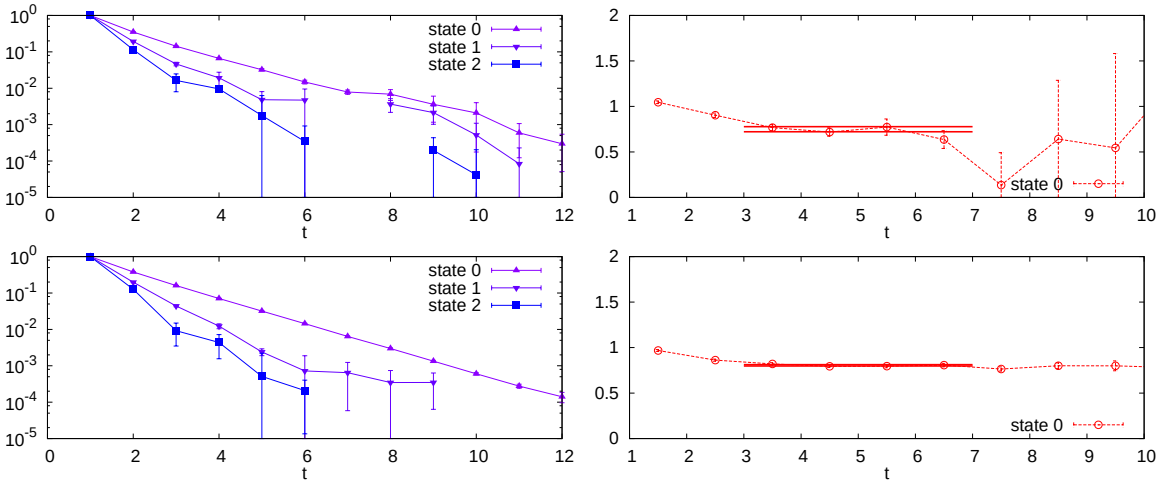

Figure 4.3: a_1 with 4 (upper row) and 64 (lower row) eigenmodes subtracted: The correlators for all eigenstates (left), effective mass plot for the lowest state (right).

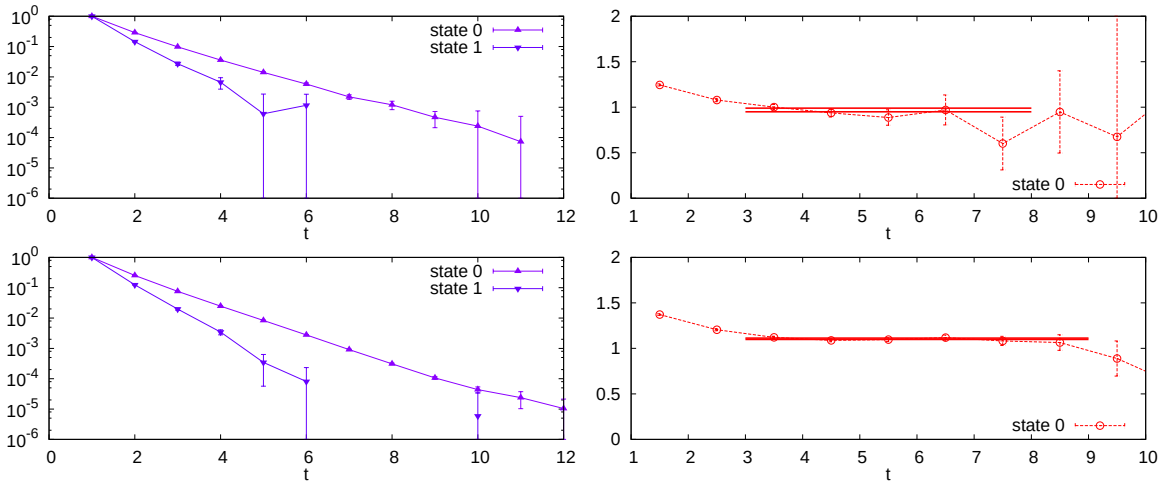

Figure 4.4: b_1 with 2 (upper row) and 128 (lower row) eigenmodes subtracted: The correlators for all eigenstates (left), effective mass plot for the lowest state (right).

4.5 Results and Discussion

4.5.1 Truncation study

The reduction parameter k in (4.2) gives the number of the lowest eigenmodes of the Dirac operator removed from the quark propagator. We study reduced quark propagators with $k = 0, 2, 4, 8, 12, 16, 20, 32, 64, 128$ and three different quark smearings (n, w, ∂_i). These are then combined into different hadron propagators and the correlation matrix for a hadron with given quantum numbers is calculated. The variational method is used to extract the ground and excited states of that hadron. Consequently, we observe and study the evolution of hadron masses as a function of the number of the subtracted lowest eigenmodes. Increasing the number of the subtracted lowest eigenmodes we gradually remove the chiral condensate of the vacuum and consequently "unbreak" the chiral symmetry.

Typical results for the mesons and baryons under study are shown in Figs. 4.1 - 4.12. For each hadron we show in the figures two representative reduction levels k for which we also show explicitly all eigenvalues stemming from the variational method, i.e., the correlators corresponding to different energy levels. Moreover, we show for the ground and first excited state (where applicable) the eigenvector components and the effective mass plots including fit ranges and values. The energy values are determined from exponential fits to the eigenvalues over the indicated fit ranges.

In Figs. 4.1 and 4.2 we show the eigenvalues and eigenvectors (cf. Sect. 4.3.4) and the effective mass plots for the ground and excited states of the ρ-meson ($J^{PC} = 1^{--}$) after having subtracted 12 and 32 eigenmodes of D_5. (The results for the untruncated situation, with higher statistics and for several more parameter sets are shown in [88].) The eigenvector composition for both states is stable and clearly distinct. The mass splitting between ground state and excited state disappears with increasing truncation level.

For the meson channels a_1 and b_1 the statistics allow only to determine the ground state in a reliable way. In the case of the a_1 ($J^{PC} = 1^{++}$) meson (Fig. 4.3 for $k = 4$ and $k = 64$) and for the b_1 ($J^{PC} = 1^{+-}$) meson (Fig. 4.4 for $k = 2$ and $k = 128$) we thus show only the ground states. We observe improved plateau quality for the effective masses when increasing number of truncated modes.

In Fig. 4.5 the nucleon of positive parity (the ground state and its first excitation, $J^P = \frac{1}{2}^+$), after having subtracted the lowest 20 eigenmodes is shown. These should be compared with Fig. 4.6 where 64 modes have been subtracted. In Fig. 4.7 and 4.8 we present two nucleon states of negative parity, $J^P = \frac{1}{2}^-$, (at reduction level 12 and 64).

The positive parity Δ ground and excited states, $J^P = \frac{3}{2}^+$ at reduction level 16 and 128 are shown in Fig. 4.9 and Fig. 4.10 and the negative parity Δ's ($J^P = \frac{3}{2}^-$) at the same reduction

levels are given in Fig. 4.11 and Fig. 4.12, respectively.

An obvious observation is that the quality of the signal (the quality of plateaus) essentially improves with increasing the number of removed eigenmodes for all hadrons under study. This fact makes it easier to reliably identify masses of states after unbreaking the chiral symmetry. In many cases for excited hadrons the quality of plateaus before unbreaking of the chiral symmetry is rather poor, but after removing more and more eigenmodes of the Dirac operator it becomes better and better, so eventually it allows to unambiguously establish that indeed we see the state, even though with the untruncated propagators the identification of the state would be less clear.

A plausible explanation for this phenomenon would be that by unbreaking the chiral symmetry we remove from the hadron its pion cloud and subtract all higher Fock components like πN, $\pi\Delta$, $\pi\pi$, and so on from the hadron wave functions. It is these components related to the chiral symmetry breaking that couple excited and not excited hadrons to each other and render signals from the excited states poor in fully untruncated QCD.

4.5.2 Confinement after unbreaking the chiral symmetry

The most interesting question is whether hadrons and confinement survive the unbreaking of the chiral symmetry. To discuss this issue we put all the results from the previous figures together and analyze how masses of the considered hadrons change with the reduction level. Therefore, the relevant truncation scale is not the Dirac operator eigenmode index k itself, since it has to scale with the lattice volume when keeping the physics constant. Instead, we introduce a cutoff parameter σ such that the reduction level σ means that all μ_k for which $|\mu_k| < \sigma$ have been excluded in the underlying quark propagators [1]. We still give the corresponding index k on the upper horizontal scale of the plots.

The masses of all studied hadrons under D_5 eigenmode reduction are summarized in Fig. 4.13. The scale is set by the Sommer parameter (i.e., by the static potential acting between two heavy quarks, in other words, by the gluonic dynamics). The physics of the static potential knows nothing about the valence quarks and the truncation of lowest lying eigenmodes of the Dirac operator for the light valence quarks. It implies that these plots suggest at least qualitatively the evolution of the hadron masses in absolute units of energy. We observe approximately a universal growth of all hadron masses with equal slope after subtraction of a sufficient amount of the chiral modes of the Dirac operator. In this regime chiral symmetry is approximately restored and the whole hadron mass is not related to chiral symmetry breaking. A universal slope might be interpreted as an indication to a universal growth of the hadron size.

Assume that after having unbroken the chiral symmetry the exponential decay signals from all hadrons would disappear. This would indicate that with the artificial restoration of the

chiral symmetry confinement also vanishes and that there is a direct connection between the confinement in QCD and the lowest lying modes of the Dirac operator. Contrary to that we observe a very clear signal from all hadrons, except for a pion. This suggests that confinement survives the unbreaking of the chiral symmetry.

However, there is still the possibility that this clear signal comes from the unconfined (unbound) quarks with some mass m_0 at a given truncation level. In this case we would expect at a given truncation level a universal scaling law with all mesons having the mass $2\,m_0$ and all baryons with the mass $3\,m_0$. There would be no excited states of hadrons.

In order to address this issue we show in Fig. 4.14 all hadron masses in units of the ρ-meson mass obtained at the same truncation level. Indeed, some of the states – such as a_1 and ρ', as well as the ground and the first excited states of the nucleon of both parities – do follow this behavior of mass $2\,m_0$ and $3\,m_0$ for mesons and baryons, respectively. However, this is definitely not the case for the b_1 state as well as for the Δ-resonance and especially its first excited states of positive and negative parity. Given that the signal in all latter cases is unambiguous, we conclude that there is no universal scaling ($2\,m_0$ for mesons and $3\,m_0$ for baryons) for all hadrons. This rules out the possibility that our signals are produced by the unbound (unconfined) quarks. We do observe confined hadrons.

Actually, this can be seen also from another perspective. The mass m_0 is large and increases with truncation of the quark propagators. At the same time we observe chiral restoration in the correlators (e.g., a_1 and ρ). The large mass m_0 of unconfined free quarks then contradicts restoration of chiral symmetry. This supports our argument that we do not observe unconfined quarks.

The fact that masses of some of the mesons and some of the baryons get degenerate and are related through a simple law $2\,m_0$ for mesons and $3\,m_0$ for baryons indicates symmetries of hadrons that appear after unbreaking (restoration) of the chiral symmetry.

4.5.3 Meson degeneracies and splittings and what they tell us

Restoration of the $SU(2)_L \times SU(2)_R$ chiral symmetry in the vacuum requires the states to fall into parity-chiral multiplets [99, 100, 57, 58, 66]. Below we shortly summarize a content of these parity-chiral multiplets for the mesons in our study.

The full set of multiplets of the parity-chiral group $SU(2)_L \times SU(2)_R \times C_i$, where the group C_i consists of identity and the space inversion, for the $J = 1$ mesons is as follows:

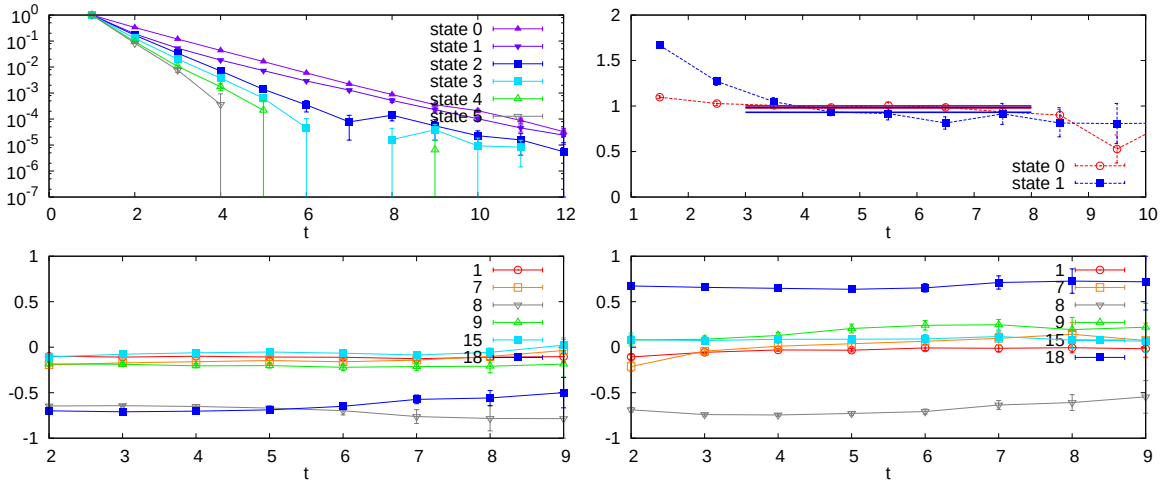

Figure 4.5: $N(+)$ with 20 eigenmodes subtracted: The correlators for all eigenstates (upper left), effective mass plot for the two lowest states (upper right), eigenvectors corresponding to the ground state (lower left). and 1st excited state (lower right).

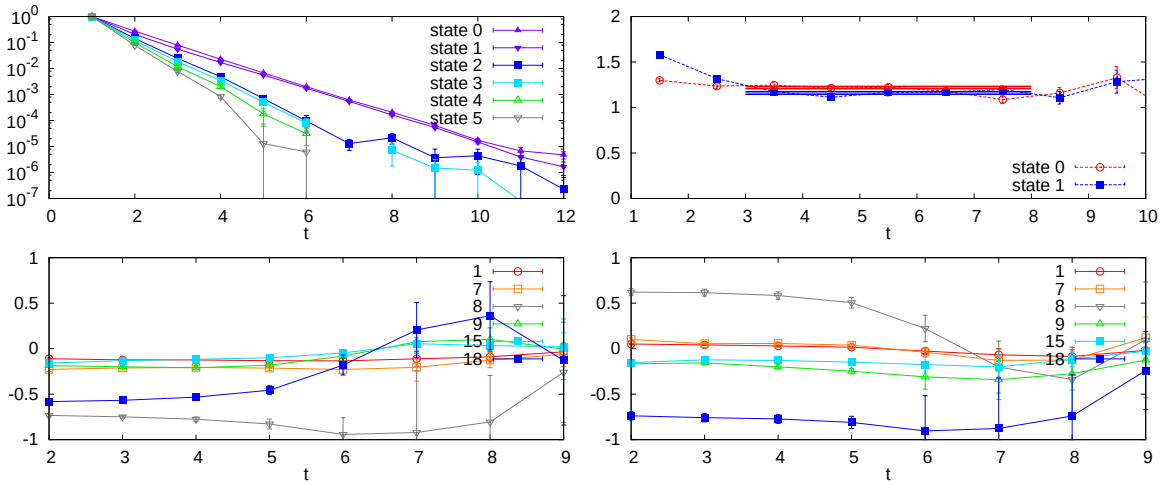

Figure 4.6: $N(+)$ with 64 eigenmodes subtracted: The correlators for all eigenstates (upper left), effective mass plot for the two lowest states (upper right), eigenvectors corresponding to the ground state (lower left). and 1st excited state (lower right).

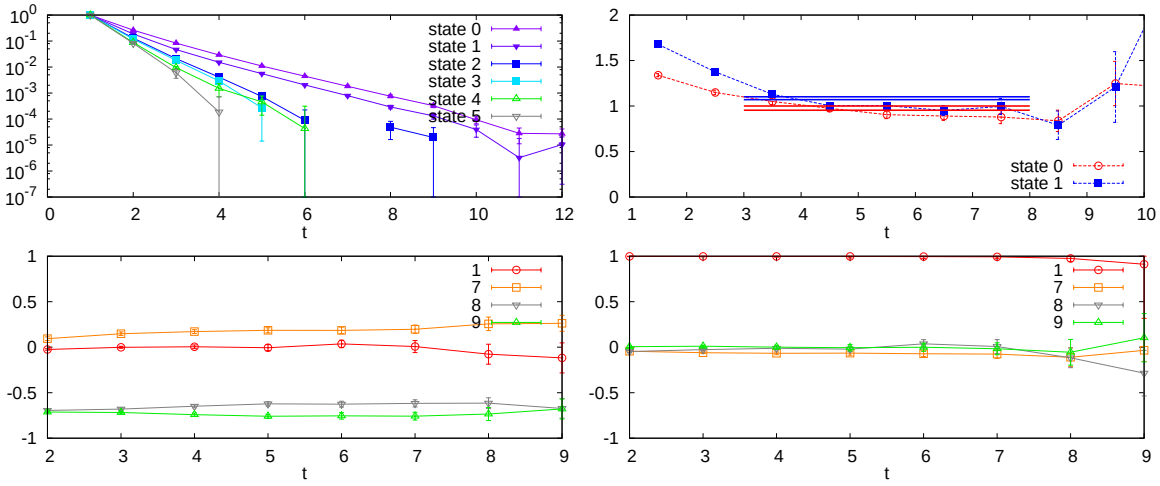

Figure 4.7: $N(-)$ with 12 eigenmodes subtracted: The correlators for all eigenstates (upper left), effective mass plot for the two lowest states (upper right), eigenvectors corresponding to the ground state (lower left). and 1st excited state (lower right).

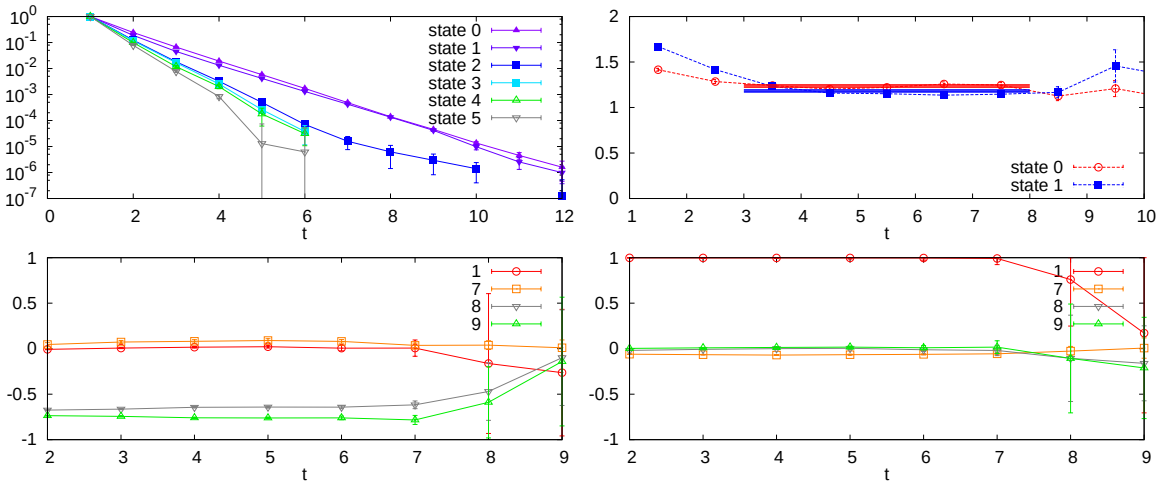

Figure 4.8: $N(-)$ with 64 eigenmodes subtracted: The correlators for all eigenstates (upper left), effective mass plot for the two lowest states (upper right), eigenvectors corresponding to the ground state (lower left). and 1st excited state (lower right).

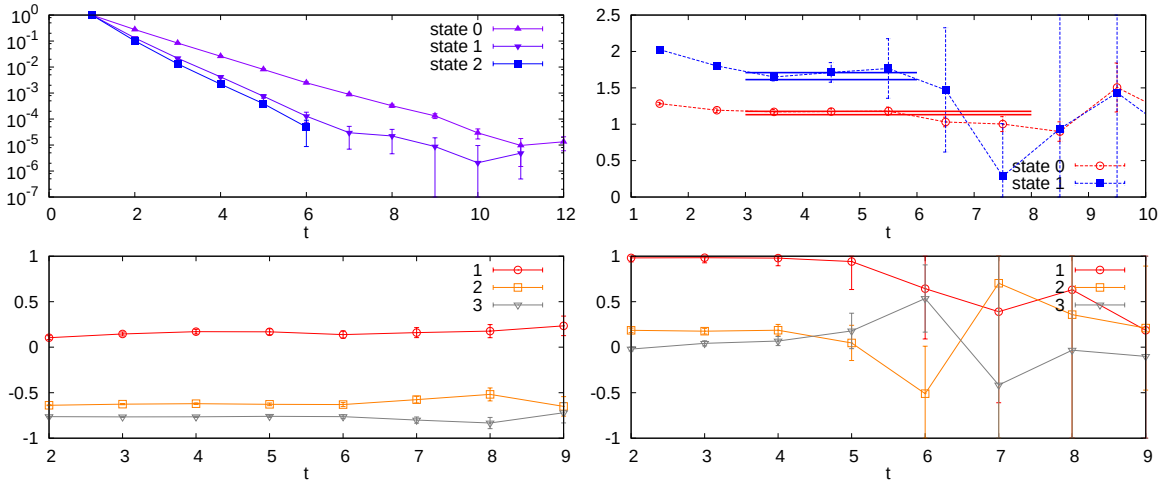

Figure 4.9: $\Delta(+)$ with 16 eigenmodes subtracted: The correlators for all eigenstates (upper left), effective mass plot for the two lowest states (upper right), eigenvectors corresponding to the ground state (lower left). and 1st excited state (lower right).

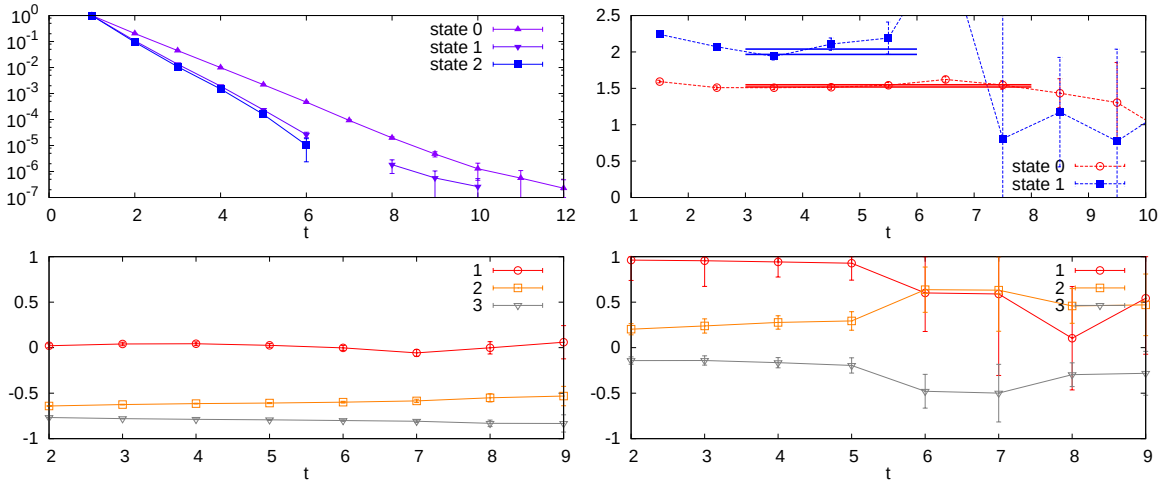

Figure 4.10: $\Delta(+)$ with 128 eigenmodes subtracted: The correlators for all eigenstates (upper left), effective mass plot for the two lowest states (upper right), eigenvectors corresponding to the ground state (lower left). and 1st excited state (lower right).

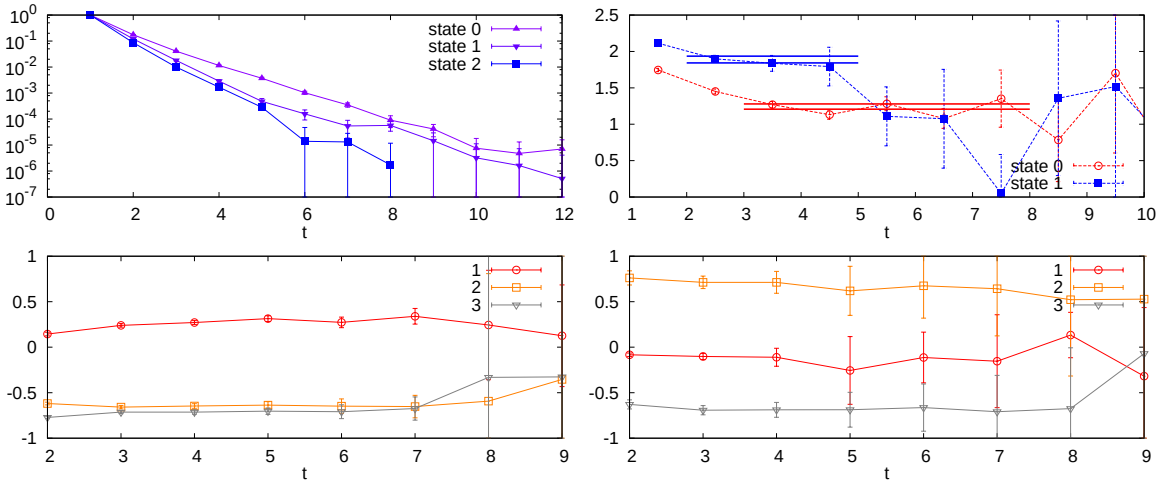

Figure 4.11: $\Delta(-)$ with 16 eigenmodes subtracted: The correlators for all eigenstates (upper left), effective mass plot for the two lowest states (upper right), eigenvectors corresponding to the ground state (lower left). and 1st excited state (lower right).

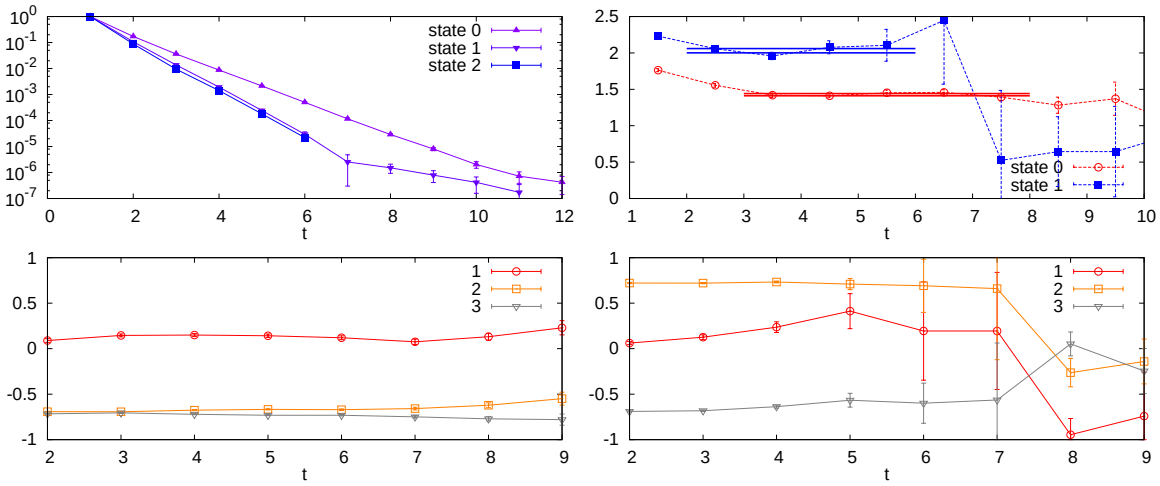

Figure 4.12: $\Delta(-)$ with 128 eigenmodes subtracted: The correlators for all eigenstates (upper left), effective mass plot for the two lowest states (upper right), eigenvectors corresponding to the ground state (lower left). and 1st excited state (lower right).

$$
\begin{array}{lcll}
(0,0) & : & \omega(0,1^{--}) & f_1(0,1^{++}) \\
(\frac{1}{2},\frac{1}{2})_a & : & h_1(0,1^{+-}) & \rho(1,1^{--}) \\
(\frac{1}{2},\frac{1}{2})_b & : & \omega(0,1^{--}) & b_1(1,1^{+-}) \\
(0,1)+(1,0) & : & a_1(1,1^{++}) & \rho(1,1^{--})
\end{array}
$$

Note, that the unbroken chiral $SU(2)_L \times SU(2)_R$ symmetry requires existence of two independent ρ-mesons, one of them is the chiral partner of the h_1 meson, and the other one of the a_1 state. Similar is true for the ω-meson.

The states from two distinct multiplets $(\frac{1}{2},\frac{1}{2})_a$ and $(\frac{1}{2},\frac{1}{2})_b$ that have the same isospin but opposite spatial parity are connected to each other by the $U(1)_A$ transformation, if the $U(1)_A$ symmetry is broken neither explicitly nor spontaneously. In our real world $U(1)_A$ is broken both explicitly via the axial anomaly and spontaneously via the quark condensate of the vacuum. So in the world with restored $U(1)_A$ symmetry a ρ meson, that is the chiral partner to the h_1 meson, would be degenerate with the b_1 state. The h_1, ρ, ω and b_1 states would form an irreducible multiplet of the $SU(2)_L \times SU(2)_R \times U(1)_A$ group.

On top of the chirally symmetric vacuum the $\rho - a_1$ splitting vanishes, see, e.g., Figs. 4.13 and 4.14., a clear signal of the chiral $SU(2)_L \times SU(2)_R$ symmetry restoration in the physical states. At the same time large $b_1 - \rho$ and $b_1 - \rho'$ splittings persist. This is a direct indication that the $U(1)_A$ breaking does not disappear. While that $U(1)_A$ breaking component that is due to the chiral condensate should vanish with the condensate, the $U(1)_A$ breaking via the axial anomaly still persists. Then it follows that there is no direct interconnection of the lowest lying modes of the Dirac operator and the mechanism of the anomalous $U(1)_A$ breaking in QCD. Such a direct interconnection was suggested in the past through, e.g., the instanton fluctuations.

After unbreaking of the chiral symmetry the ρ and ρ' mesons become degenerate. What does this tell us? A degeneracy indicates some symmetry. The two distinct ρ states, ρ and ρ', lie in different irreducible parity-chiral representations, $(\frac{1}{2},\frac{1}{2})_a$ and $(0,1)+(1,0)$. In principle, their degeneracy could point out to a reducible representation of the parity-chiral group that would include both irreducible representations. Indeed, the product of two fundamental quark-antiquark chiral representations does contain, in particular, both $(\frac{1}{2},\frac{1}{2})_a$ and $(0,1)+(1,0)$:

$$
\begin{aligned}
&[(0,\tfrac{1}{2})+(\tfrac{1}{2},0)] \times [(0,\tfrac{1}{2})+(\tfrac{1}{2},0)] \\
&\quad = (0,0)+(\tfrac{1}{2},\tfrac{1}{2})_a+(\tfrac{1}{2},\tfrac{1}{2})_b+(0,1)+(1,0)\ . \qquad (4.6)
\end{aligned}
$$

Such a multiplet of dimension 16 (including isospin degeneracies) would consist of two distinct ω-mesons, f_1, h_1, two ρ-mesons as well as b_1 and a_1 mesons and would require a degeneracy of all of them. Now we do find, however, that the b_1 meson is well split from both ρ and ρ' after

the unbreaking of the chiral symmetry. This rules out that the observed $\rho - \rho'$ degeneracy is related to restored chiral symmetry. The degenerate ρ and ρ' states are different because their eigenvectors are orthogonal and because they are well split before the removal of the low-modes. This can be clearly seen from Figs. 4.13 and 4.14. This degeneracy indicates some higher symmetry that includes chiral $SU(2)_L \times SU(2)_R$ as a subgroup. It is a highly exciting question what this higher symmetry is. It will be seen from the following subsection that baryons also point to some higher symmetry.

4.5.4 Baryon chiral multiplets

If chiral symmetry is restored and baryons are still there they have to fall into (some of) the possible baryonic parity-chiral multiplets. There are three different irreducible representations of $SU(2)_L \times SU(2)_R \times C_i$ for baryons of any fixed spin:

$$(\tfrac{1}{2},0) + (0,\tfrac{1}{2})\,,\ (\tfrac{3}{2},0) + (0,\tfrac{3}{2})\,,\ (\tfrac{1}{2},1) + (1,\tfrac{1}{2})\,. \tag{4.7}$$

The first representation combines nucleons of positive and negative parity into a parity doublet. The second representation consists of both positive and negative parity Δ's of the same spin. Finally, the third representation, that is a quartet, includes one nucleon and one Delta parity doublet with the same spin.

Extraction of the chiral eigenmodes of the Dirac operator leads to a systematic appearance of the parity doublets, as it is clearly seen from Figs. 4.13 and 4.14. There are two degenerate nucleon parity doublets with the same mass. There are also two distinct Δ parity doublets, but with different mass. Since our interpolators have spin $J = \frac{1}{2}$ for nucleons and $J = \frac{3}{2}$ for Delta's, we cannot see possible quartets of the $(\frac{1}{2},1) + (1,\frac{1}{2})$ type.

It is very interesting that the two nucleon parity doublets get degenerate, while the two Delta doublets are well split. The former hints at a higher symmetry for the $J = I = \frac{1}{2}$ states, while this higher symmetry is absent for the $J = I = \frac{3}{2}$ states.

4.5.5 On the origin of the hyperfine splitting in QCD

The $\Delta - N$ splitting is usually attributed to the hyperfine spin-spin interaction between valence quarks. The realistic candidates for this interaction are the spin-spin color-magnetic interaction [116, 117] and the flavor-spin interaction related to the spontaneous chiral symmetry breaking [118]. It is an old debated issue which one is really responsible for the hyperfine splittings in baryons. Our results suggest some answer to this question. Once chiral symmetry breaking is removed, which happens for the ground N and Δ states after extraction of the 50–60 lowest eigenmodes, the $\Delta - N$ splitting is reduced roughly by the factor 2. With the restored chiral

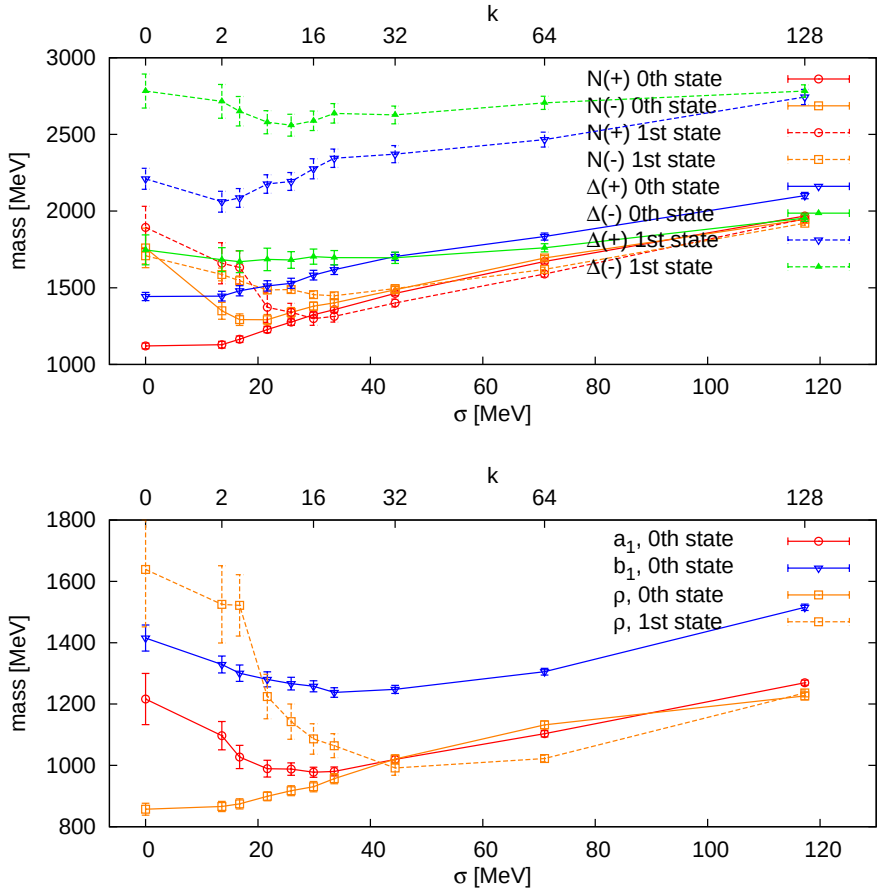

Figure 4.13: Summary plots: Baryon (top) and meson (bottom) masses as a function of the truncation level.

symmetry the effective flavor-spin quark-quark interaction is impossible. The color-magnetic interaction is still there. This result suggests that in our real world the contribution of both these mechanisms to the $\Delta - N$ splitting is of equal importance.

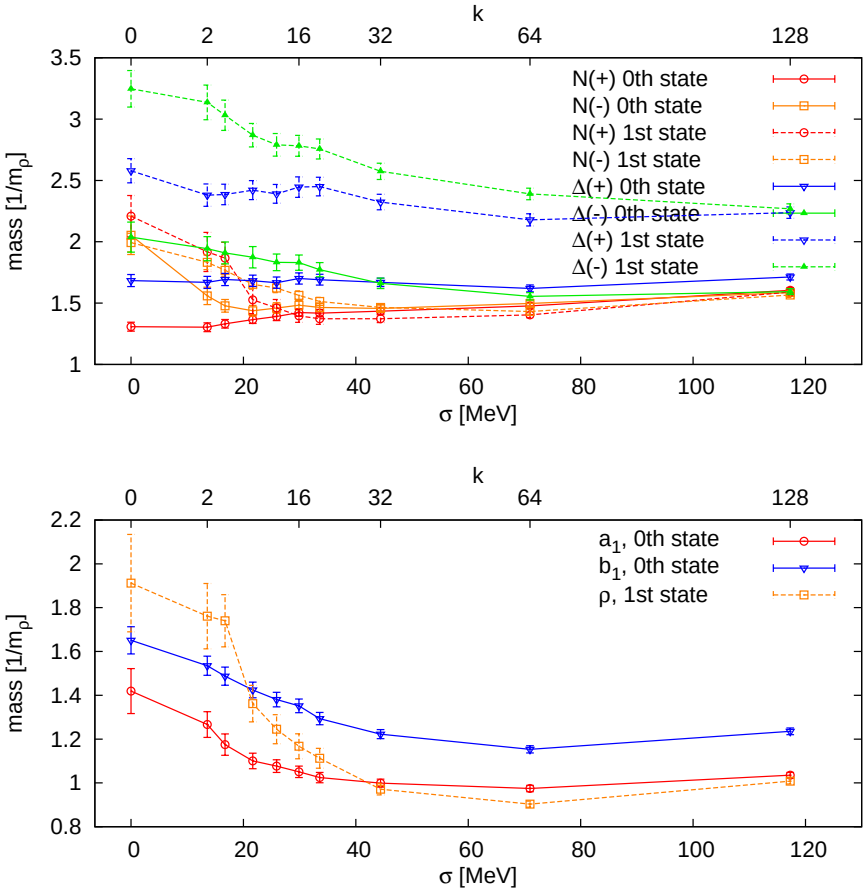

Figure 4.14: Summary plots: Baryons (top) and mesons (bottom) in units of the ρ-mass at the corresponding truncation level.

4.6 Conclusions

We have studied what happens with different mesons and baryons upon modifying the valence quark propagators by removing the lowest lying eigenmodes of the Dirac operator. These eigenmodes are directly related to the quark condensate of the vacuum via the Banks–Casher relation. Consequently, upon removal of the lowest eigenmodes we artificially restore chiral symmetry, what we call "unbreaking" of the chiral symmetry. We study the evolution of the hadron masses with the number of extracted lowest eigenmodes in dynamical lattice simulations. There are a few interesting observations.

First, the quality of the signals from the hadrons after removal of the chiral eigenmodes of the valence quark propagators become much better than with the untruncated propagators. Most probably this is related to the fact that we artificially remove the pion cloud of the hadrons.

Second, from the spectral patterns both for the ground and excited mesons and baryons we conclude that confinement is still there while the chiral symmetry is artificially restored. Restoration of the chiral symmetry is evidenced by the fact that hadrons, both baryons and mesons, fall into different parity-chiral multiplets. At the same time there is a clear evidence that the broken $U(1)_A$ symmetry is not restored.

Third, some distinct parity doublets get degenerate upon chiral symmetry restoration. This indicates that there is some higher symmetry in the chirally restored regime, that includes the chiral group as a subgroup.

Finally, from the comparison of the hyperfine $\Delta - N$ splitting before and after unbreaking of the chiral symmetry we conclude that in our real world both the color-magnetic and the flavor-spin interactions between valence quarks are of equal importance.

Chapter 5

Coulomb, Landau and maximally Abelian gauge fixing in lattice QCD with multi-GPUs

This chapter stems from a project which is only indirectly related to the previous works. It consists of publication

- [4] Mario Schröck, Hannes Vogt, *"Coulomb, Landau and maximally Abelian gauge fixing in lattice QCD with multi-GPUs"*, Comp. Phys. Commun. **184** (2013) 1907-1919

and was originally motivated by the study of the quark propagator under Dirac low-mode truncation, presented in Chap. 3. The quark propagator is not gauge invariant and thus the gauge has to be fixed for the investigation of the quark mass function. Gauge fixing on the lattice is computationally demanding. However, the strict locality of a family of popular gauge fixing algorithms allows for a very fine grained parallelization and modern graphic processing units (GPUs) provide the hardware for such a fine grained approach to parallelization. The difficulty herein lies on the one hand in the memory constraints of GPUs and furthermore in the tuning of the code towards peak performance which has to take detailed hardware knowledge of the underlying architecture into account.

5.0 Abstract

A lattice gauge theory framework for simulations on graphic processing units (GPUs) using NVIDIA's CUDA is presented. The code comprises template classes that take care of an optimal data pattern to ensure coalesced reading from device memory to achieve maximum performance. In this work we concentrate on applications for lattice gauge fixing in 3+1 dimensional SU(3) lattice gauge field theories. We employ the overrelaxation, stochastic relaxation and simulated

annealing algorithms which are perfectly suited to be accelerated by highly parallel architectures like GPUs. The applications support the Coulomb, Landau and maximally Abelian gauges. Moreover, we explore the evolution of the numerical accuracy of the SU(3) valued degrees of freedom over the runtime of the algorithms in single (SP) and double precision (DP). Therefrom we draw conclusions on the reliability of SP and DP simulations and suggest a mixed precision scheme that performs the critical parts of the algorithm in full DP while retaining 80–90% of the SP performance. Finally, multi-GPUs are adopted to overcome the memory constraint of single GPUs. A communicator class which hides the MPI data exchange at the boundaries of the lattice domains, via the low bandwidth PCI-Bus, effectively behind calculations in the inner part of the domain is presented. Linear scaling using 16 NVIDIA Tesla C2070 devices and a maximum performance of 3.5 Teraflops on lattices of size down to $64^3 \times 256$ is demonstrated.

5.1 Introduction

Quantum chromodynamics (QCD) is nowadays, 40 years after its birth, widely accepted as the correct theory of the strong nuclear force which binds the protons and neutrons in the cores of atoms. The guiding principle in the construction of QCD was the local gauge symmetry which has led before to the very successful theory of quantum electrodynamics (QED) that describes the interactions of electrons and light. Local gauge symmetry is the freedom to perform a transformation of the vector fields of the theory, independently at each point of space-time, without changing the physics the theory describes.

Lattice QCD which lives on a discretized space-time background opposed to the continuous world of the original theory, offers a formulation of the gauge theory that is well suited to be simulated on a computer and hence can be used to test the theory against experiment. Furthermore, lattice simulations can help to gain insights in the highly nontrivial, nonperturbative regime of the interactions between quarks and gluons which are the degrees of freedom of QCD.

The gauge symmetry, given below in its discrete version, states that physical observables will remain unchanged if a local transformation of the form

$$g(x)U_\mu(x)g(x+\hat{\mu})^\dagger \tag{5.1}$$

is being carried out. Here, the gauge fields or *link variables* $U_\mu(x)$ as well as the gauge transformations $g(x)$ are elements of the underlying gauge group which is SU(3) in the case of QCD. The index $\mu = 0,\ldots,3$ refers to the direction in four dimensional space-time and with $x+\hat{\mu}$ we denote the neighbor lattice site of x in the μ-direction. The link variables of lattice

QCD are connected to the algebra valued continuum gauge fields $A_\mu(x)$ via

$$U_\mu(x) = \mathrm{e}^{iagA_\mu(x)} \,. \tag{5.2}$$

Whereas physical observables that can be measured in experiments must be independent of the gauge, fixing the gauge, i.e., choosing a particular gauge transformation $g(x)$ for all x, is essential when, e.g., studying gauge dependent quantities like the fundamental two point functions of the theory.

As a typical example of a gauge condition that may be enforced at all space-time points x, we consider the manifestly covariant Landau gauge

$$\partial_\mu A_\mu(x) = 0, \tag{5.3}$$

here stated in the language of continuum field theories. As we will discuss in the next Section, the continuum gauge condition (5.3) translates to a large scale optimization problem in lattice QCD with $\mathcal{O}(VN_c^2)$ degrees of freedom where $V = N_s^3 \times N_t$ is the $3+1$ dimensional lattice volume. Consequently, the process of fixing the gauge on the lattice demands a major part of the whole simulation's computer time and the possible acceleration by highly parallel hardware architectures like graphic processing units (GPUs) will be of great practical use.

A more conceptual issue of gauge fixing is that the set of gauge transformations $g(x)$ that fulfill a desired gauge condition is far from being unique. The set of gauge equivalent configurations of a given gauge field is called the gauge orbit. The gauge fixing condition can be depicted as a hypersurface living in the space of all gauge fields. Each of the multiple intersections of the gauge orbit with the gauge fixing hypersurface is called a Gribov copy.

Gribov copies play a crucial role in restoring the BRST symmetry on the lattice: fixing a gauge via the Faddeev–Popov procedure on the lattice for a compact group boils down to inserting the sum over signs of the corresponding Faddeev–Popov determinants evaluated at all the Gribov copies. Neuberger [119] showed that the sum for any covariant gauge turns out to be zero for any standard model gauge group, SU(N), and for compact U(1), making the expectation value of a gauge-fixed observable 0/0. The zero comes up because each Gribov copy comes in pairs with opposite sign of the Faddeev–Popov determinant. This in turn makes it impossible to construct a BRST symmetry on the lattice. This is called the Neuberger 0/0 problem. Following a topological interpretation of the Neuberger 0/0 problem, in Refs. [120, 121] a modified lattice Landau gauge was proposed which evaded the problem. There, because the Faddeev–Popov is shown to be strictly positive (semi-)definite, the cancellation is avoided. However, it is yet to be shown that the number of Gribov copies in the modified lattice Landau gauge is independent of the background gauge field. Interestingly, recently, a deep relation

between lattice gauge fixing and lattice supersymmetry has been proposed in Ref. [122, 123]: the partition functions of a class of supersymmetric Yang–Mills theories can be viewed as a gauge fixing partition function à la Faddeev–Popov and the "Gribov copies" are then nothing but the classical configurations of the theory.

A possible way out of the problem of the existence of Gribov copies is to restrict the gauge fixing hypersurface to a region which the gauge orbit intersects only once. An example thereof is the so-called Fundamental Modular Region [124] which contains only that intersection of the gauge orbit which corresponds to the global optimum of the gauge condition. Unfortunately, no algorithm is known which finds the global optimum of the gauge condition within finite simulation time. *Simulated annealing*, however, has been shown to highly favor optima closer to the global optimum [125, 126] and moreover it can be shown that, in the limit of infinite time, simulated annealing actually converges to the global maximum.

Recently, the problem of counting Gribov copies has gained a renewed interest. In Refs. [127], an explicit formula of the number of Gribov copies for any number of lattice sites is analytically derived for lattice Landau gauge for the one-dimensional compact U(1) case. In Refs. [128, 129], a novel method based on Algebraic Geometry [130, 131, 132], which can count all the Gribov copies, was proposed. Although the method has only been able to work for small lattices, it is the only known method which guarantees to find all Gribov copies and hence it can work as a benchmark for other methods. One such alternative method is plain brute force, i.e., running a standard optimization algorithm over and over again from different starting points on the gauge orbit and collecting the results consecutively. Clearly, a high performance lattice gauge fixing code is essential for this task and since here one primarily focuses on small lattices, GPUs are favorable given the fact that CPU parallelization techniques are very limited for lattices of small extent.

In this work we present a set of applications for lattice gauge fixing based on the family of relaxation algorithms and simulated annealing. The applications are based on the CUDA accelerated Lattice–Graz–Tübingen code[1] that is written in CUDA C/C++ and makes heavy use of template classes in order to facilitate the extension to a broad variety of applications. Besides the standard relaxation algorithm [133], we support overrelaxation [134] and stochastic relaxation [135] to overcome the problem of critical slowing down. Moreover, the simulated annealing algorithm [125] with a heat bath kernel and microcanonical updates which increases the probability to reach the Fundamental Modular Region has been implemented and tested. The code can be used to fix gauge configurations to the covariant Landau gauge $\partial_\mu A_\mu = 0$, $\mu = 0,\ldots,3$, the Coulomb gauge $\partial_i A_i = 0$, $i = 1,2,3$ and the maximally Abelian gauge.

1 Available for download at www.cuLGT.com

Previous utilizations of GPUs in the field of lattice QCD mainly focused on solvers of linear systems [136, 137]

A first attempt of porting lattice gauge fixing with the overrelaxation algorithm to the GPU has been reported in [2, 7]. An alternative approach based on the steepest descent method has been presented in [138]. For a more general discussion of lattice gauge fixing and its problems we refer the reader to [85].

The remainder of this work is organized as follows: in Sec. 5.2 the optimization problem is stated and the algorithms of choice are presented. In Sec. 5.3 we summarize some hardware properties of the NVIDIA GPUs that we use for our investigation and moreover briefly discuss NVIDIA's programming environment *CUDA*. Next, in Sec. 5.4, we give details of our implementation and the cuLGT framework and moreover discuss numerical accuracy issues. To overcome the memory constraint of single GPUs we extend our implementation to support multi-GPUs; all details thereto are presented in Sec. 5.5. Finally, in Sec. 5.6 we show various performance results for single and multiple GPUs and furthermore present some convergence results of the algorithms. In Sec. 5.7 we summarize and conclude.

5.2 The algorithms

In this Section we will first summarize the defining equations of the optimization problem. Subsequently, we discuss the various flavors of the update kernels and finally we list the main underlying algorithm of this work explicitly in terms of pseudo-code.

5.2.1 The gauge functionals

On the lattice, enforcing a gauge condition, e.g., (5.3) is equivalent to maximizing the corresponding gauge functional. We support three different kinds of gauge conditions and here we give the related gauge functionals and moreover a measure of the iteratively achieved gauge quality that can serve as a stopping criterion for the algorithm.

Coulomb and Landau gauge

The continuum Landau gauge condition, (5.3), is fulfilled if and only if the lattice gauge functional

$$F^g_{\text{Landau}}[U] = \frac{1}{N_c N_d V} \mathfrak{Re} \sum_{\mu,x} \text{tr} \left[U^g_\mu(x) \right], \tag{5.4}$$

resides in a stationary point with respect to gauge transformations $g(x) \in \mathrm{SU}(N_c)$. In the above equation we made use of the short hand notation

$$U_\mu^g(x) \equiv g(x)U_\mu(x)g(x+\hat{\mu})^\dagger. \tag{5.5}$$

Furthermore, with N_c we denote the dimension of the gauge group $SU(N_c)$, $N_c = 3$ for QCD, N_d is the number of space-time dimensions, ($N_d = 4$ for our work) and V is the number of lattice points. When switching to Coulomb gauge, all that changes is that the sum in (5.4) becomes limited to the spatial components of the Dirac index μ, thus leaving out the temporal one. Consequently, the optimization of (5.4) for Coulomb gauge can be performed independently on different time-slices.

A measure θ of how well the Landau/Coulomb gauge condition is satisfied on a given gauge field configuration is the average L_2-norm of the gauge fixing violation $\Delta(x)$, i.e., the discrete derivative of the continuum gauge fields

$$\Delta(x) \equiv \sum_\mu \left(A_\mu(x) - A_\mu(x-\hat{\mu})\right) = 0, \tag{5.6}$$

$$\theta \equiv \frac{1}{N_c V} \sum_x \mathrm{tr}\left[\Delta(x)\Delta(x)^\dagger\right]. \tag{5.7}$$

Maximally Abelian gauge

The gauge functional for the maximally Abelian gauge is, in the case of SU(2), given by

$$F_{\mathrm{MAG2}}^g[U] = \frac{1}{2N_d V} \sum_{x,\mu} \mathrm{tr}\left[\sigma_3 U_\mu(x)\sigma_3 U_\mu(x)^\dagger\right] \tag{5.8}$$

where σ_3 is the diagonal matrix of the three Pauli matrices that correspond to the generators of SU(2). Equivalently, in the case of SU(3) the gauge functional reads

$$F_{\mathrm{MAG3}}^g[U] = \frac{1}{3N_d V} \sum_{x,\mu} \mathrm{tr}\left[\lambda_3 U_\mu(x)\lambda_3 U_\mu(x)^\dagger\right] + \mathrm{tr}\left[\lambda_8 U_\mu(x)\lambda_8 U_\mu(x)^\dagger\right] \tag{5.9}$$

where λ_3 and λ_8 build the Cartan subalgebra of SU(3). Maximizing (5.9) is equivalent to minimizing the off-diagonal components $A_\mu^{(i)}(x)$, $i \neq 3{,}8$ of the continuum gauge fields

$$A_\mu(x) = \frac{1}{2}\sum_{i=1}^{8} \lambda_i A_\mu^{(i)}(x). \tag{5.10}$$

Note that maximizing (5.8) or (5.9), respectively, is equivalent to maximizing the squares of the diagonal of each gauge link

$$F^g_{\mathrm{MAG}}[U] = \frac{1}{N_c N_d V} \sum_{x,\mu,i} \left| (U_\mu(x))_{ii} \right|^2 \tag{5.11}$$

which is the gauge functional that we use in practice.

When the SU(2) gauge functional (5.8) is stationary with respect to gauge transformations, then the off-diagonal elements of

$$X(x) = \sum_\mu \left(U_\mu(x) \sigma_3 U_\mu(x)^\dagger + U_\mu(x-\hat{\mu})^\dagger \sigma_3 U_\mu(x-\hat{\mu}) \right) \tag{5.12}$$

must vanish [139]. Thus, for SU(2) we can use

$$\theta = \frac{1}{N_c V} \sum_x \left| (X(x))_{12} \right|^2 \tag{5.13}$$

as a measure of the gauge quality. The off-diagonal element $(X(x))_{12}$ reads explicitly

$$\begin{aligned} (X(x))_{12} = \sum_\mu & 2(u_{\mu,0}(x)u_{\mu,2}(x) + u_{\mu,1}(x)u_{\mu,3}(x) \\ & -iu_{\mu,0}(x)u_{\mu,1}(x) - iu_{\mu,2}(x)u_{\mu,3}(x) \\ & +u_{\mu,0}(x-\hat{\mu})u_{\mu,2}(x-\hat{\mu}) + u_{\mu,1}(x-\hat{\mu})u_{\mu,3}(x-\hat{\mu}) \\ & +iu_{\mu,0}(x-\hat{\mu})u_{\mu,1}(x-\hat{\mu}) - iu_{\mu,2}(x-\hat{\mu})u_{\mu,3}(x-\hat{\mu})) \end{aligned} \tag{5.14}$$

where we adopted the Cayley–Klein parametrization

$$U_\mu = \begin{pmatrix} u_{\mu,0} + iu_{\mu,3} & u_{\mu,2} + iu_{\mu,1} \\ -u_{\mu,2} + iu_{\mu,1} & u_{\mu,0} - iu_{\mu,3} \end{pmatrix}. \tag{5.15}$$

For SU(3), we use equivalently

$$\theta = \frac{1}{N_c V} \sum_x \left| (X(x))_{12} + (Y(x))_{12} + (Z(x))_{12} \right|^2 \tag{5.16}$$

where the matrices $X(x), Y(x), Z(x) \in \mathrm{SU}(2)$ stem from the three SU(2) subgroups of SU(3).

5.2.2 Relaxation

Now that we stated the optimization problem, we can proceed with presenting the algorithms which we will use to find a solution to the problem before we will discuss the implementation

with CUDA in the next Section.

The main idea of the relaxation algorithm is to sweep over the lattice site by site while optimizing the gauge functional locally. Thereby, as we will see below, can all sites of one of the two *parity subsets* (think of a checker board decomposition) be optimized at the same time since the newly generated local optimum is a function of the nearest neighbors only.

In the following we will discuss the calculation of the local optimum separately for Coulomb/Landau gauge and the maximally Abelian gauge.

Coulomb and Landau gauge

Instead of taking the complete global gauge functional into account,

$$F^g_{\text{Landau}}[U] = \frac{1}{2N_cN_dV}\mathfrak{Re}\sum_x f^g_{\text{Landau}}(x), \tag{5.17}$$

the relaxation algorithm aims at optimizing the value of $F^g[U]$ locally, i.e., for all x the maximum of

$$f^g_{\text{Landau}}(x) = \mathfrak{Re}\ \text{tr}\,[g(x)K(x)] \tag{5.18}$$

is sought. Here we introduced

$$K(x) := \sum_\mu \left(U_\mu(x)g(x+\hat{\mu})^\dagger + U_\mu(x-\hat{\mu})^\dagger g(x-\hat{\mu})^\dagger\right) \tag{5.19}$$

where the sum runs over all space-time indices for Landau gauge and for Coulomb gauge it leaves out the temporal index. The local maximum thereof is, in the case of the gauge group SU(2), simply given by

$$g(x) = K(x)^\dagger/\sqrt{\det\,[K(x)^\dagger]}. \tag{5.20}$$

For the gauge group SU(3) (QCD) one iteratively operates in the three SU(2) subgroups [140] and thereby optimizes the local SU(3) gauge functional.

Maximally Abelian gauge

Similarly as for the Coulomb and Landau gauges, the goal is to maximize the gauge functional (5.8) locally. Again, we only need to know how to achieve this for SU(2) and then we can operate in the SU(2) subgroups of SU(3) for applications in QCD.

Thus, for a given site x we want to maximize

$$\begin{aligned} f^g_{\text{MAG2}}(x) = \sum_\mu \text{tr}\,[&\sigma_3 g(x)U_\mu(x)\sigma_3 U_\mu(x)^\dagger g(x)^\dagger \\ &+\sigma_3 U_\mu(x-\hat{\mu})^\dagger g(x)\sigma_3 g(x)^\dagger U_\mu(x-\hat{\mu})]. \end{aligned} \tag{5.21}$$

Let us focus on the part of (5.21) with the up-going links only, i.e., the first term in the sum; the second term of (5.21) can be treated equivalently.

For the following discussion it will be useful to switch to the Cayley–Klein parametrization of $g(x)$ and $U_\mu(x)$,

$$g = g_0 \mathbb{1} + i \sum_{i=1}^{3} g_i \sigma_i = \begin{pmatrix} g_0 + i g_3 & g_2 + i g_1 \\ -g_2 + i g_1 & g_0 - i g_3 \end{pmatrix} \tag{5.22}$$

and

$$U_\mu = \begin{pmatrix} u_{\mu,0} + i u_{\mu,3} & u_{\mu,2} + i u_{\mu,1} \\ -u_{\mu,2} + i u_{\mu,1} & u_{\mu,0} - i u_{\mu,3} \end{pmatrix}, \tag{5.23}$$

respectively, where for a simpler notation we suppressed the space-time argument x.

Taking the fact that transformations proportional to σ_3 leave the functional (5.8) unchanged into account (thus setting $g_3 = 0$) one obtains

$$\begin{aligned} f^{\text{up}}_{\text{MAG2}}(x) = \sum_\mu - 2\Big(& 4 g_0 (g_1 u_{\mu,0} u_{\mu,1} + g_2 u_{\mu,0} u_{\mu,2} - g_2 u_{\mu,1} u_{\mu,3} + g_1 u_{\mu,2} u_{\mu,3}) \\ & + g_0^2 \left(-u_{\mu,0}^2 + u_{\mu,1}^2 + u_{\mu,2}^2 - u_{\mu,3}^2 \right) \\ & + \left(g_1^2 + g_2^2 \right) \left(u_{\mu,0}^2 - u_{\mu,1}^2 - u_{\mu,2}^2 + u_{\mu,3}^2 \right) \Big). \end{aligned} \tag{5.24}$$

Using a matrix/vector notation with $\boldsymbol{g}^T \equiv (g_0, g_1, g_2)^T$ the latter can be written as

$$f^{\text{up}}_{\text{MAG2}}(x) = 2 \boldsymbol{g}^T \begin{pmatrix} D & E & F \\ E & -D & 0 \\ F & 0 & -D \end{pmatrix} \boldsymbol{g} \tag{5.25}$$

where we defined

$$D = \sum_\mu \left(u_{\mu,0}^2 + u_{\mu,3}^2 - \frac{1}{2} \right) \tag{5.26}$$

$$E = 2 \sum_\mu \left(-u_{\mu,0} u_{\mu,1} - u_{\mu,2} u_{\mu,3} \right) \tag{5.27}$$

$$F = 2 \sum_\mu \left(-u_{\mu,0} u_{\mu,2} + u_{\mu,1} u_{\mu,3} \right) \tag{5.28}$$

whereby in D we used $\det [U_\mu] = u_{\mu,0}^2 + u_{\mu,1}^2 + u_{\mu,2}^2 + u_{\mu,3}^2 = 1$.

Then the maximum of (5.24) is found when $\boldsymbol{g}$ is set to the eigenvector of the matrix of (5.25) corresponding to the largest eigenvalue. The largest eigenvalue is $\lambda = \sqrt{D^2 + E^2 + F^2}$ and the

corresponding eigenvector is

$$\left(D + \sqrt{D^2 + E^2 + F^2}\ ,\ E\ ,\ F\right)^T . \tag{5.29}$$

We refer the reader to [139] for more practical details related to the maximally Abelian gauge.

Overrelaxation

In order to reduce the *critical slowing down* of the relaxation algorithm on large lattices, the authors of [134] suggested to apply an overrelaxation algorithm which replaces the local gauge transformation $g(x)$ by $g^{\omega}(x)$, $\omega \in [1,2)$ in each step of the iteration. In practice the exponentiation of the gauge transformation will be done to first order.

Microcanonical steps

Applying a gauge transformation $g^{\omega}(x)$ with $\omega = 2$ leaves the Landau/Coulomb gauge functional invariant but these so-called microcanonical steps have the beneficial property to lead to a faster decorrelation and thus to faster convergence of the functional from which the simulated annealing algorithm will profit.

Stochastic relaxation

The stochastic relaxation algorithm replaces the local gauge update $g(x)$ by a microcanonical step $g^2(x)$ with probability p and can lead to faster convergence on large lattices.

5.2.3 Simulated annealing

Annealing is a method in condensed matter physics to bring certain materials in their ground state by first heating them above their melting point and subsequently cooling them down very slowly. It is crucial hereby that the system is given enough time to thermalize at each temperature step. If so, the atoms will arrange themselves in such a way that the macroscopic system ends up in its – or at least close to its – lowest energy state.

The authors of [125] developed an analogy of annealing and mathematical optimization problems. Following this analogy, the function which is to be optimized corresponds to the energy of the solid and the optimum is the ground state.

The algorithm then simply performs local *Metropolis* updates where the acceptance probability of a random local gauge update $g(x)$ is given by

$$P[g(x)] = \begin{cases} 1 & \text{if} \quad f^g(x) \geq f(x) \\ \exp\left(\frac{f^g(x) - f(x)}{T}\right) & \text{else.} \end{cases} \tag{5.30}$$

Thus, while in a hot temperature regime, the algorithm accepts a worsening of the local gauge functional with a nonvanishing probability which ensures that the algorithm may overcome local extrema in order to increase the probability to find the global optimum.

In practice, the Metropolis update gets replaced by *heat bath* updates that generate the new gauge transformation directly with the right Boltzmann like probability distribution.[1] In order to reach quicker thermalization at each temperature step, we perform three microcanonical steps after each change in temperature. Note that simulated annealing will never reach the required gauge precision θ very accurately, instead relaxation or overrelaxation which can be regarded as simulated annealing in the limit of zero temperature, should be run subsequently to fully reach the required precision. See also Sec. 5.6.4.

5.2.4 Putting things together

After we have listed the details of the underlying large scale optimization problem and the techniques to perform local optimizations, we are now in the position to consider the global optimization algorithm.

As mentioned before, due to the strict locality of the family of relaxation algorithms and the simulated annealing algorithm, we can perform a checkerboard decomposition of the lattice and operate on all sites of one of the two sublattices *even* and *odd*[2] concurrently. All of the above mentioned algorithms have the same underlying structure which is depicted in Alg. 5.1.

Algorithm 5.1

```
while precision θ not reached do
  for sublattice = even, odd do
    for all x of sublattice do
      for all SU(2) subgroups do
        local optimization: find g(x) ∈ SU(2)                    Step 1.
        which is a function of U_μ(x), U_μ(x − μ̂)
        for all μ do
          apply g(x) to U_μ(x), U_μ(x − μ̂)                       Step 2.
        end for
      end for
    end for
  end for
end while
```

We want to stress that the difference of the various update algorithms as well as the difference between the gauges under consideration lies exclusively in Step 1 whereas, as we list explicitly

1 We use the *Philox* RNG of the *Random123 library*[141] to generate random numbers in the heat bath kernel.
2 The sum over the space-time indices $t + x + y + z$ determines whether a site is considered *even* or *odd*.

in A.2, the main work of the algorithm lies in Step 2 which is independent of the update type and of the target gauge.

5.3 CUDA

Here we briefly introduce the CUDA (Compute Unified Device Architecture) programming model and summarize the hardware properties of the GPUs we adopt in our study.

5.3.1 The programming model

The CUDA model demands the division of the underlying problem into subproblems, so-called *thread blocks*, that can be treated independently from each other in parallel. These thread blocks, on the other hand, are ensembles of threads and the threads within a thread block may communicate with each other through shared memory. The independent thread blocks then form a so-called *grid*. This model is very flexible and allows the user to run a CUDA application on different hardwares (meaning different number of streaming multiprocessors (SMs) and CUDA cores) without the need for major adjustments.[1] This abstraction layer is introduced into the C language by defining a new set of functions which are called *kernels* and are identified by the ___*global*___ declaration specifier. The kernel is executed N times where

$$N = \text{block size} \times \text{grid size} \tag{5.31}$$

and each kernel call is a thread in the nomenclature introduced above. For the invocation of the kernel a new syntax is introduced where the block size and the total number of blocks (grid size) is specified. A unique index is given to each thread to assign, e.g., different memory addresses to different threads.

A group of 32 threads (the number depends on the hardware generation) of the same block are tied together to what is called a *warp*. The operations of all threads within a warp are executed simultaneously as long as they follow the same instruction path. Otherwise, the operations become serialized resulting in up to 32 cycles instead of one, a *warp divergence* occurs.

To efficiently hide memory latencies it is inevitable to have many warps active at the same time on a SM. The possible number of active blocks (or warps) depends on the available hardware that has to be divided among the threads, e.g., it depends on how many registers and how much shared memory is needed for an individual kernel.

1 Since we exclusively adopt devices of the Fermi generation, the characteristic of the SMs is always the same for our tests, see Sec. 5.3.3.

5.3.2 Memory layout

In the CUDA terminology the CPU on which the CUDA application is run is called the *host*, whereas the GPU is called *device* and the associated memory is called host and device memory, respectively. Communication between host and device memory is the main bottleneck. Although, for many single GPU implementations, communication is only necessary in the beginning and in the end of an application. How one effectively can deal with communication from device to device through the host memory in multi-GPU simulations is discussed in Sec. 5.5. The part of device memory that is accessible from the host as well as from all CUDA threads is called *global memory*. Global memory is allocated by a command in the host code. Each thread may then allocate its private *local memory* which resides in the same physical memory as global memory. Global and local memory are both cached in a L1 and L2 cache by default (for Fermi), on a cache miss the latency to device memory is very high. For most applications the bandwidth to device memory is another limiting factor, although it is large compared with a common CPU to RAM bandwidth.

For communication within a block *shared memory* can be used. Shared memory has a very low latency since it resides in the same hardware as the L1 cache.

5.3.3 Hardware

We adopt four different NVIDIA Fermi GPUs for our study, the GTX 480 and GTX 580 from the consumer section and moreover the Quadro 4000 and the Tesla C2070 from the scientific/HPC section. The Tesla C2070, opposed to the consumer cards, supports ECC (error correcting code) protection for DRAM. Recently, the successor of the Fermi architecture has been released (Kepler). In Tab. 5.1 we give the data which is common to all Fermi GPUs, the hardware details of the individual devices are summarized in Tab. 5.2.

compute capability	2.0
cores / SM	32 per SM
warp size	32
L1 cache / SM	16 KiB or 48 KiB
shared memory / SM	16 KiB or 48 KiB
32-bit registers / SM	32768 (32Ki)
max. registers / thread	63

Table 5.1: Specifications of the Fermi architecture.

	GTX 480	GTX 580	Quadro 4000	Tesla C2070
graphics clock	700 MHz	772 MHz	475 MHz	575 MHz
SMs	15	16	8	14
total CUDA cores	480	512	256	448
device memory	1.5 GiB	1.5 GiB	2 GiB	6 GiB
memory bandw.	177.4 GB/s	192.4 GB/s	89.6 GB/s	144 GB/s

Table 5.2: Hardware details of the Fermi devices that we adopt in this work.

5.4 Implementation details

5.4.1 Code design

The design goal of our code was the minimization of local memory usage. One of the main limiting factors of performance is the number of registers that are available per thread: on Fermi GPUs, the latter bound is 63 registers of 32-bit each. If more variables (on the assembly level) are needed per thread, the registers are "spilled" to local memory. Local memory, as mentioned earlier, uses the same hardware as global memory and thus has the same (high) latency and bandwidth bounds. Besides register spilling another source of local memory usage may slow down the execution of a kernel: registers are not addressable and therefore will arrays generally be placed in local memory. In order to capacitate the compiler to place arrays in registers, the size of the arrays and all index variables that access elements need to be computable at compile time[1]. Early versions of our code fulfilled this requirement by manually unrolling all loops and using C macros to access array elements. The present code, however, uses template parameters for the lattice dimensions and the dimension N_c of the gauge group $\mathrm{SU}(N_c)$. As a consequence, unrolling can perfectly be done by the compiler. This code design offers a very flexible setup for further lattice applications.

5.4.2 Reduce memory transfers

In order to reduce memory transfers between global memory and the kernel a 12 parameter representation of the SU(3) matrices has been suggested [142, 136], i.e., only two rows of the matrix are stored and loaded. If we denote the first and the second row of the matrix with vectors $\boldsymbol{u}$ and $\boldsymbol{v}$, respectively, then the third row is given by $(\boldsymbol{u} \times \boldsymbol{v})^*$. The extra numerical work to reconstruct the full matrix is hidden since our kernels are bound by memory transactions and not by floating point operations. This optimization reduces the number of bytes to load and store per site from 576 bytes to 384 in single precision.

1 The latter statement implies that, for example, all for loops have to be unrolled.

Memory pattern

Due to the hardware design of NVIDIA GPUs one has to adopt special memory layouts to efficiently utilize the memory bus to global memory. The peculiarity of these devices is that memory transactions of threads of the same warp are coalesced if they reside in the same 128-byte aligned segment in global memory. Consequently, neighboring threads (i.e. neighboring sites) should access neighboring memory addresses to achieve high memory throughput. A natural memory layout where the gauge links (SU(3) matrices) are stored in one block in memory does not fulfill these requirements, hence the index order of the gauge fields in memory has to be adapted.

The authors of [138], e.g, use the native CUDA datatype *Float4* and therefore distribute the 12 real numbers of a SU(3) element (in the 12 parameter representation, see Sec. 5.4.2) to three *Float4* arrays. In contrast, we build on a more flexible way by employing one large float or double array, respectively, in combination with an access pattern class that hides the memory layout from the user. This strategy allows us to easily change the memory layout depending on the properties of the underlying application.

Here we list explicitly the memory patterns that are in use in our gauge fixing applications, whereby the slowest running index is listed first:

- *StandardPattern* (natural layout): t, x, y, z, μ, i, j, c
- *GpuPattern*: $\mu, i, j, c, p, [t, x, y, z]_p$
- *GpuPatternTimeslice*: $t, \mu, i, j, c, p, [x, y, z]_p$
- *GpuPatternParityPriority*: $p, \mu, i, j, c, [t, x, y, z]_p$
- *GpuPatternTimesliceParityPriority*: $t, p, \mu, i, j, c, [x, y, z]_p$

where $i, j \in \{0,1,2\}$ are the matrix indices, c identifies real ($c = 0$) and imaginary ($c = 1$) part of the complex number, $\mu \in \{0, \ldots, 3\}$ is the direction of the link, t is the index in temporal direction and x,y,z correspond to the spatial components. The index $p \in \{0,1\}$ stands for parity (*even* and *odd*, respectively) and in those patterns where it is in use the space-time indices are split into two groups

$$[t, x, y, z]_p := \{t, x, y, z | \, t + x + y + z \mod 2 = p\} \tag{5.32}$$

and equivalently for $[x, y, z]_p$. Parity splitting is necessary to achieve coalesced access to global memory, since we operate on the parity even and odd sublattices separately (see Alg. 5.1).

The *GpuPattern* is used in the single GPU implementations of Landau and maximally Abelian gauge. For Coulomb gauge we employ the *GpuPatternTimeslice* for the global gauge field array

and the *GpuPattern* in kernels that operate on $1 \times N_s^3$ sublattices, i.e., within a single time-slice. To reduce memory traffic between the nodes in the multi-GPU implementation we adopt the *GpuPatternTimesliceParityPriority*. This allows that only the active parity of the time-slices at the border can be transferred between nodes. All applications use the *StandardPattern* to read and write files with the natural ordering.

All patterns assume that the global array is allocated for full 18 parameter SU(3) links although the applications load and store only 12 parameters.

Representation of the SU(3) link variables

We define a template class *SU3* with a template parameter that determines the storage type. For matrices that reside in the global memory array we offer a class *Link* with three parameters: (1) the pointer to the global memory array, (2) a lattice site given in terms of an object of type *SiteIndex* and (3) the direction μ. No memory is allocated for $SU3\langle Link\rangle$ variables. For local matrices we offer the class *Matrix* which allocates local memory (or uses registers when possible) for matrix elements. Functions for copying between $SU3\langle Link\rangle$ and $SU3\langle Matrix\rangle$ are implemented, as well as functions to load only the first two rows (12 parameter representation) of the matrices as well as a function to restore the third row.

5.4.3 The eight-threads-per-site strategy

Within every iteration of the gauge fixing algorithms each site update needs its adjacent links. These are read from global memory and after the update they have to be written back to global memory. After having restored the third line, these eight SU(3) matrices per site equal 8×18 reals $= 144$ reals and therewith exceed the register limit of 63 per thread what results in register spills to global memory and as a consequence negatively effects the bandwidth bound performance of the kernel.

With the purpose of reducing register spills, we switch to a finer parallelization granularity: instead of assigning one thread to one lattice site we now tie eight threads to a single lattice site, i.e., one thread for each of the eight matrices that are involved in a site update. As a result, each thread needs only 18 registers to store the gauge link.

In order to avoid warp divergences the kernel is invoked with a thread block size of $8 \times 32 = 256$. By doing so, each of the eight warps takes care of one neighbor type of the 32 sites and thus all threads within one warp follow the same instruction path.

The gauge transformation is then accumulated in shared memory. Since one operates on the SU(2) subgroups of SU(3) and an SU(2) matrix can conveniently be represented by four reals, this requires $4 \times 32 = 128$ reals or 512 bytes (SP) or 1024 bytes (DP) per thread block. To avoid race conditions on the shared array the accumulation is done using the *atomic_add*

function in single precision and by explicit serialization using *__syncthreads()* in combination with *if*-statements in double precision[1].

The benefit of this strategy is that, in single precision, no register spillings occur at all if no further constraints on the kernel are applied (see Sec. 5.4.4) and for double precision, register spills are drastically reduced. The drawback of the current implementation compared to a more conventional one-thread-per-site strategy is that the number of simultaneously computed sites per multiprocessors is decreased. Nevertheless this strategy results in a clear overall performance gain [7].

5.4.4 Optimizations

Besides the aforementioned algorithmic optimizations we further tuned our code by optimizing the CUDA settings.

First of all we set *launch bounds* to individual kernels: by specifying the number of threads per block and a minimum of active blocks a bound on the maximal register usage is given. Without *launch bounds* the compiler uses 45 registers in the overrelaxation kernel for Landau and Coulomb gauges, resulting in a theoretical occupancy of 42%. By setting the register limit to 32 the theoretical occupancy is increased to 67% on the cost of a small amount of register spilling (24 byte stack frame, 24 byte spill stores, 40 byte spill loads).[2] The same settings are applied to the other gauge fixing kernels.

Fermi devices have a L1 cache that physically shares the same 64 KiB hardware (per SM) with shared memory. The size of the L1 cache and shared memory can be set by the user for each kernel. Since we only need 512 Byte shared memory per block and a maximum of 4 blocks is possible, we only need a total of 2 KiB shared memory per SM. This allows us to set the kernel to a *prefer L1 cache* configuration which means 16 KiB shared memory and 48 KiB of L1 cache. With this setting the register spilling introduced by the launch bounds is cached more efficiently.

By a global compiler switch, the use of L1 cache can be set to either caching (default) or non-caching (-Xptxas -dlcm=cg) loads. By using non-caching loads our applications shows a small improvement in performance. This is due to the fact that the use of global memory is designed such that only in the beginning of each kernel the matrices are loaded to local memory (i.e., into registers) and after all operations are finished they are written back. In between there is no reuse of cached data and thus there is no benefit in caching at all. With non-caching load

1 *atomic_add* is not supported for datatype *double*.

2 The given values for register usage and spilling are for CUDA Toolkit 5.0 compiled for compute capability 2.0. They vary between different between CUDA 4.x and 5.0 but the optimal launch bounds are found to be the same.

the L1 cache is solely used for register spilling and write-backs of register spills to the device memory are reduced or totally removed.

In all applications we compile with the *use_fast_math* switch. Single precision operations are then replaced by faster implementations on the expense of precision though we did not experience any effects by this setting. For double precision operations there is no such option.

5.4.5 Numerical accuracy

In the following we investigate the accumulation of numerical rounding errors within our lattice gauge fixing applications. A suitable measure is the conservation of unitarity of the SU(3) matrices during the progress of the algorithm through many iterations. In Fig. 5.1 we show

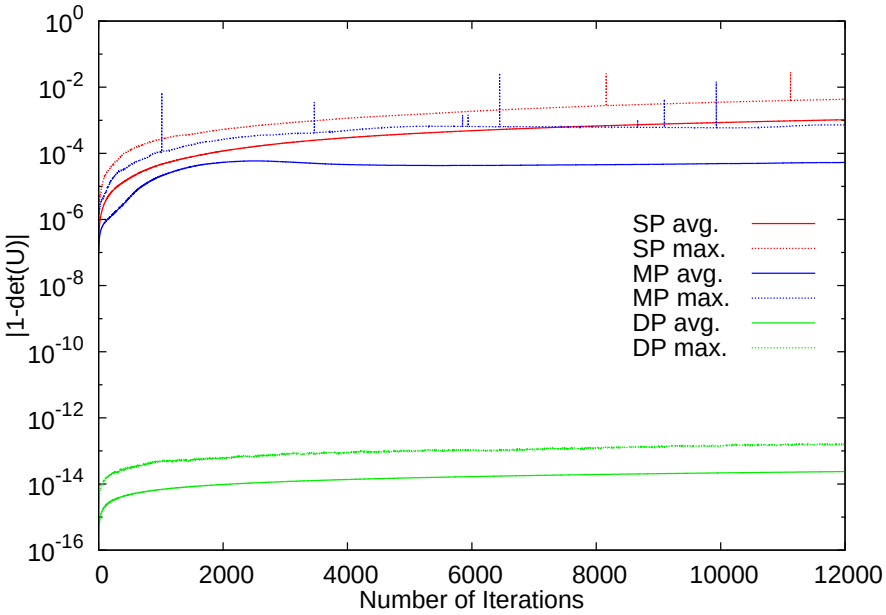

Figure 5.1: Conservation of unitarity ($|1 - \det[(]\, U)|$) in SP, MP and DP.

$$\frac{1}{4V}\sum_{\mu,x}|1 - \det[(]\, U_\mu(x))| \quad \text{and} \quad \max_{\mu,x}|1 - \det[(]\, U_\mu(x))| \tag{5.33}$$

from a run over 12000 iterations of the overrelaxation update on a 32^4 lattice in single (SP) and double (DP) floating point precision. Moreover the plot shows lines corresponding to a mixed precision (MP) ansatz which calculates the overrelaxation gauge update on the SP gauge fields in full DP (see Fig. A.3) while the less precision demanding application of the gauge transformation to the links (Step 2 in Alg. 5.1) is performed in SP.

In DP, both, the average and even the maximal value stay well below 10^{-12} whereas in SP the error accumulates to the order 10^{-3}. To overcome the loss of unitarity, one may use the

unitarity as a constraint and thus reproject the links to SU(3) after a given number of iteration steps.

The peaks in the SP maximum lines are individual outliers that occur approximately every 1000 iterations in one of the links of a 32^4 lattice on our GTX 580, whereas they could not be detected on the Quadro 4000.

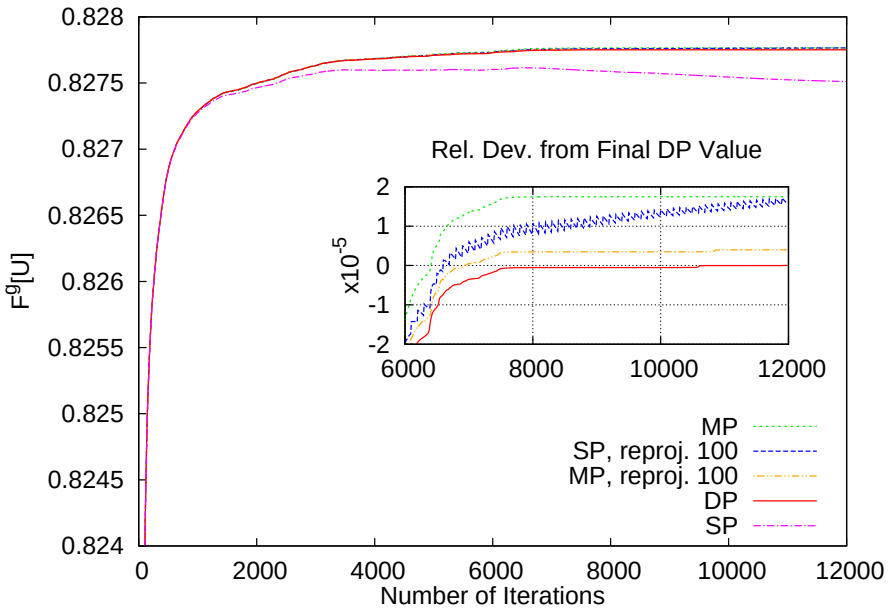

Figure 5.2: The value of the Landau gauge functional $F^g_{\text{Landau}}[U]$ as a function of the number of iterations of the overrelaxation kernel in single (SP), mixed (MP) and double precision (DP). In addition, the evolution of the functional value is shown when a reprojection to SU(3) is done every 100 iteration steps in SP and MP. The inner plot gives relative deviation of all curves (except SP without reprojection) from the final functional value in DP.

Whether or not the loss of high precision unitarity in SP is of significance, depends of course on the individual problem the code is applied to. In Fig. 5.2 we show the value of the Landau gauge functional which is the sensitive quantity in our applications, in different precisions, again over 12000 iterations[1] on a 32^4 lattice. It becomes obvious that SP without reprojection is not a good choice for lattice gauge fixing since the value of F^g even starts to decrease after around 3000 iterations. The DP functional value increases monotonically and finally reaches a plateau, this fact together with the previous mentioned maintenance of high precision unitarity lets us conclude that a DP simulation, even without reprojection, is very accurate. Thus, we can use the DP value as a benchmark for the other approaches. In the inner plot of Fig. 5.2 we show the relative deviation of each curve to the final DP result: SP with reprojecting to

1 The gauge precision thereafter was $\theta < 6.0 \times 10^{-11}$ for the run in DP.

unitarity after every 100 steps and MP without reprojection stay within a relative deviation of 2×10^{-5} and MP with reprojection even within 5×10^{-6}. Moreover, the MP line shares the same qualitative behavior as the DP curve (monotonicity, convergence to a constant).

Therefore, our conclusion for the required floating point precision in lattice gauge fixing is as follows: in case one is primarily interested to actually fix the gauge of a gauge field configuration without being interested in the precise value of the resulting gauge functional, SP with reprojection is fine. If it is required to obtain the gauge functional value within a precision of no more than 10^{-5}, MP with reprojection is recommended since it retains most of the SP performance, as we will show in Sec. 5.6, opposed to DP which should only be chosen when one depends on a high precision result in the value of the gauge functional.

5.5 Multi-GPU

In the following discussion we will replace the space-time argument $x = (\boldsymbol{x}, t)$ by the time argument t alone wherever the $\boldsymbol{x}$ dependence is of no significance in the given context. Moreover, we will assume that one MPI process is assigned to one GPU device and thus use the terms process and device interchangeably.

In order to share the work which has to be performed locally on each lattice site, between several processes, we adopt a straightforward domain decomposition: we split the lattice of size $N_s^3 \times N_t$ into $N_t/nprocs$ partitions, where *nprocs* denotes the number of processes involved in the parallelization. For Coulomb gauge this splitting is trivial since, as we discussed above, we can operate on the different time-slices separately and only need to apply the final gauge transformation $g(t)$ of the time-slice $U_\mu(t)$ to the temporal components of the preceding time-slice $U_0(t-1)$. This makes *on-the-fly* communication between devices for Coulomb gauge fixing unnecessary.

Manifestly covariant gauges like the Landau gauge and the maximally Abelian gauge, on the other hand, are more subtle. Here, all four neighboring links in the negative μ-direction have to be collected on each site x in order to calculate the gauge update $g(x)$ which subsequently is applied to all the eight links connected to the site x. Thus, with the ansatz of splitting the lattice across the temporal direction, we have to exchange the temporal components $U_0(x)$ of the gauge fields on time-slices that lie at the boundary of two processes.

5.5.1 Data exchange between neighboring devices

If we label the minimum time-slice that resides on a given device with $t_{\min}$ and the maximum time-slice with $t_{\max}$, then only the calculation of the local gauge transformations $g(t_{\min})$ depends on the data exchange between different processes since for its calculation the gauge

links $U_\mu(t_{\min}-1)$ that reside on the neighbor process are needed. Note that since we operate on the parity even and odd lattice sites consecutively, the currently active parity of the time-slice $U_\mu(t_{\max})$ is completely unaffected by the exchange with the neighboring process that only touches the passive parity part of $U_\mu(t_{\max})$. That means, on a given process, all time-slices except $t_{\min}$ can be updated without exchanging any information with the neighbor processes. In order to update the $U_\mu(t_{\min})$ on all devices, however, the following set of instructions has to be carried out on each device in order to transfer the links $U_0(t_{\max})$ of device i to device $i+1$:

1. *cudaMemcpyDeviceToHost* of $U_0(t_{\max})$ (inactive parity)
2. *MPI_Send* of $U_0(t_{\max})$ to device $i+1$ and *MPI_Recv* of $U_0(t_{\min}-1)$ from device $i-1$
3. *cudaMemcpyHostToDevice* of $U_0(t_{\min}-1)$
4. update $U_\mu(t_{\min})$ (active parity) which affects $U_0(t_{\min}-1)$ (inactive)
5. *cudaMemcpyDeviceToHost* of $U_0(t_{\min}-1)$ (inactive parity)
6. *MPI_Send* of $U_0(t_{\min}-1)$ to device i and *MPI_Recv* of $U_0(t_{\max})$ from device $i+1$
7. *cudaMemcpyHostToDevice* of $U_0(t_{\max})$

5.5.2 Data pattern

The memory pattern *GpuPatternTimesliceParityPriority*, introduced in Sec. 5.4.2, will be the pattern of choice for applications that get accelerated by a time-slice split multi-GPU approach. Not only is the time-index running slowest and thus allows to handle different time-slices separately in the latter mentioned pattern, moreover the time-slice internal pattern is very advantageous: each time-slice is split into its two parity parts of which each has the Dirac index μ running fastest, followed by the row index of the individual gauge matrices.

This layout ensures that the data which has to be exchanged, the first two rows (12 parameter representation) of the link variables $U_0(t_{\min})$ of a given parity, lie contiguous in device memory. The size of the data block that has to be exchanged is then given by the size of a time-slice multiplied by 1/2 (parity), 1/4 (Dirac index) and 2/3 (12 parameter representation), thus 1/12 in total.

5.5.3 Asynchronous memory transfers

We target at hiding the data exchange between different devices by overlapping them with calculations on the unaffected time-slices. Replacing the CUDA function *cudaMemcpy* with *cudaMemcpyAsync* results in a non blocking copying process from host to device or vice versa.

Making use of different *cudaStream*s a device can then perform a copying request and execute a kernel at the same time.

In order to investigate how many time-slices are needed per device to fully hide the data exchange between two devices, we measured the time for the execution of the overrelaxation kernel on one time-slice and the time for a transfer of 1/12 of a time-slice for different spatial lattice sizes N_s^3 and averaged the result over 1000 iterations, see Tab. 5.3. As we can read off from the table, the asynchronous kernel execution on two time-slices takes longer then a device to host or host to device copy process, respectively. As discussed above, the necessary data exchange between two devices includes in total four such copy processes and thus eight time-slices are enough to reach a complete overlap of data exchange from device to host (host to device) and calculations in the inner part of the domain.

So far we neglected the data exchange via MPI between the two neighboring host processes. As for the data exchange between host and device, here again it is advantageous to use non blocking functions for the data exchange, i.e., *MPI_Isend* and *MPI_Irecv*. By doing so we can again overlap the data exchange between the processes by calculations on time-slices that are not involved in the exchange.

In practice, we implemented the overlap of calculations with the data exchange between the processes and between host and device as a method of a communicator class. Then we only have to set up a certain update type (overrelaxation, simulated annealing etc.) and the *apply* method of the communicator object applies that update including full overlap with the data exchange.

N_s^3	D2H [μs]	H2D [μs]	kernel [μs]	D2H/kernel	H2D/kernel
16	0.0398	0.0368	0.0209	1.90	1.76
32	0.2543	0.2276	0.1443	1.76	1.58
64	1.2510	1.1830	1.0489	1.19	1.13
128	8.9597	8.7169	8.3041	1.08	1.05

Table 5.3: The time needed to copy the relevant part (1/12) of a time-slice from device to host (D2H) and host to device (H2D) compared with the time needed to update one time-slice with the overrelaxation kernel (all in μs) averaged over 1000 iterations for different spatial volumes N_s^3. The two most right columns give the ratios.

5.6 Results

In this Section, we firstly examine the performance of the code on various devices including multiple GPUs. There, we pick the Landau gauge overrelaxation kernel as a representative for all kernels and gauges. Secondly, we outline a few sample results obtained by the application of our lattice gauge fixing code.

5.6.1 Performance on single-GPUs

In Fig. 5.3 we show the performance of the overrelaxation kernel on the GTX 580 for different spatial volumes as a function of the temporal lattice extent. The data stems from an average of one hundred repeated applications with 1000 iterations each. We achieve up to 370 GFlops in SP, up to 300 GFlops in MP and 80 GFlops in DP. The maximum performance of 370 GFlops corresponds to an execution time of 6.4 s with the given lattice size and number of iterations. For the smaller lattices the theoretical occupancy of the device is not reached and therefore the maximum performance is not achieved. Apart from that, we find almost constant performance for all lattice volumes.

In Fig. 5.4 we compare the performance of different Fermi devices on lattices of size 32^4. Our top performers in SP are the GTX 580 with nearly 370 GFlops, followed by the GTX 480 at around 300 GFlops. The difference between these devices results from the reduction in chip clock, number of SMs and bandwidth. The scientific GPUs are designed for a longer runtime and therefore the chip clock is remarkably lower. Thus, the performance of the C2070 is only close to 200 GFlops, the Quadro 4000 is at around 120 GFlops. Noteworthy is the difference between single and double precision: the theoretical ratio of SP to DP arithmetic operations for the scientific devices is 1:2, whereas the consumer GPUs have a ratio of 1:8. Accordingly, the performance ranking changes: still the GTX 580 performs best with approximately 80 GFlops, now followed by the C2070, slightly faster than the GTX 480 at around 70 GFlops. Thus, even for the scientific GPUs the theoretical factor of a half compared to SP could not be reached. The reason is that approximately twice as many registers are needed in DP and therefore even for the maximum of 63 registers *spilling* occurs. Additionally, the theoretical occupancy is reduced by the increase in registers.

The performance data given above is intended for comparing the algorithm on different architectures. Is is based on counting Flops as described in A.2. The actual number of operations differs since we did not count the overhead for computing the third line reconstruction and we did not account for fused multiply-add operations. A true measure for the performance of our code is the number of instructions per cycle (IPC). For the top performer, the GTX 580, the IPC in SP is 1.49 which means roughly 75% of the peak performance, since a maximum of 2

instructions is issued per cycle. On the other hand, the global memory throughput is 120 GB/s which is only approximately 60% of peak. Combining these results, the most likely performance bound is not memory bandwidth, but *memory latency* which could theoretically be cured by increasing occupancy. In practice this is not possible, since this would mean further decreasing registers per thread and thus introducing additional register spilling.

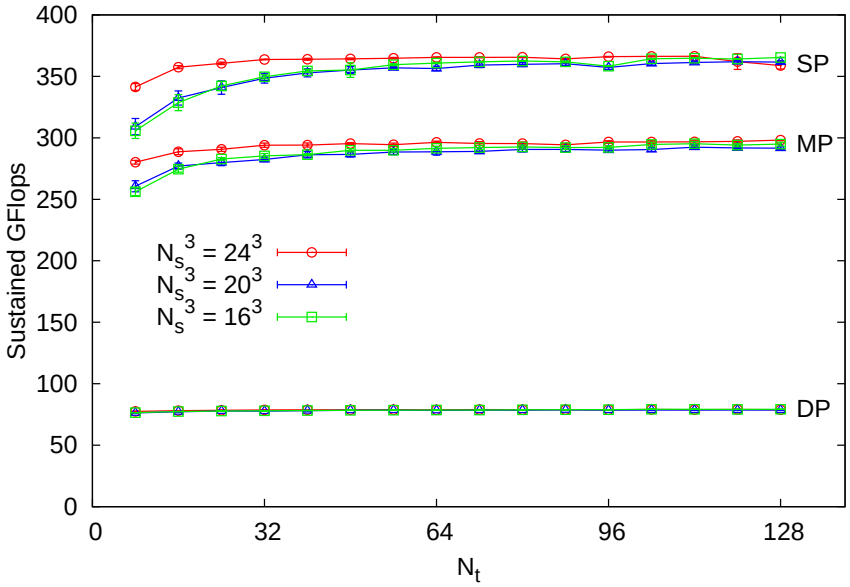

Figure 5.3: Performance of different spatial volumes as a function of the temporal lattice extend in SP, MP and DP on a GTX 580.

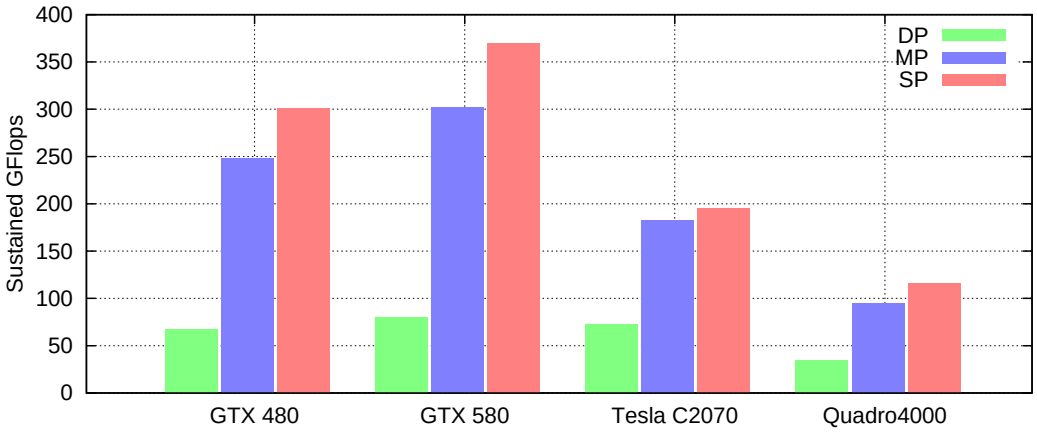

Figure 5.4: Performance of the Landau overrelaxation kernel on different NVIDIA devices in single (SP), mixed (MP) and double precision (DP) on a 32^4 lattice.

5.6.2 Performance on multi-GPUs

Our multi-GPU performance tests have been carried out on the "mephisto" cluster at the University of Graz. The cluster provides five compute nodes with four NVIDIA Tesla C2070 GPUs and CUDA 5.0. Moreover, each node offers two Intel Xeon Six-Core CPUs X5650 ("Westmere") @ 2.67GHz on each node. The nodes are connected via InfiniBand and OpenMPI 1.4.3 and CUDA 5.0 is installed.

In the plot of Fig. 5.5 we show that linear weak scaling is reached with this strategy. The test have been performed on lattices of size $64^3 \times 32$ per GPU ($64^3 \times 512$ in total with 16 GPUs) and 48^4 per GPU ($48^3 \times 768$ in total with 16 GPUs). The higher performance of the spatial volume of 64^3 is simply due to higher occupancy: since we operate on single time-slices at a time, the lattice of spatial size 48^3 is not sufficient to efficiently occupy the device.

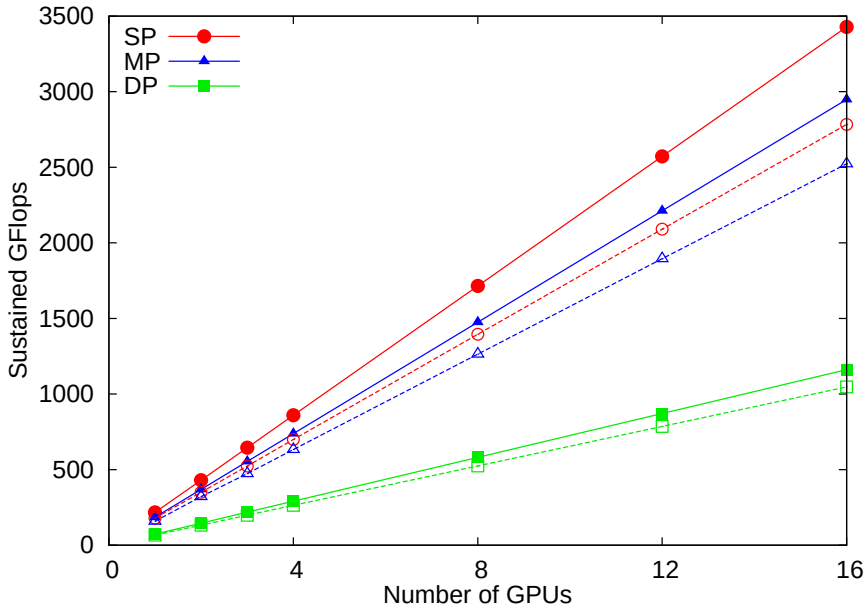

Figure 5.5: Weak scaling on the Tesla C2070 in single (SP), mixed (MP) and double precision (DP). The full symbols correspond to a lattice size of $64^3 \times 32$ per GPU and the open symbols to 48^4 per GPU.

In Fig. 5.6 strong scaling is tested. For a total lattice size of $64^3 \times 256$ we find close to linear strong scaling up to 16 GPUs which corresponds to 16 time-slices per device. On a lattice of size $64^3 \times 128$ we find for 16 GPUs (eight time-slices per device) a performance loss of 15–30% (DP vs. SP). When moving on to a smaller temporal lattice extent, $N_t = 96$, the performance decreases further. Moreover, for this lattice size, no gain in performance is apparent when adopting 16 instead of 12 devices.

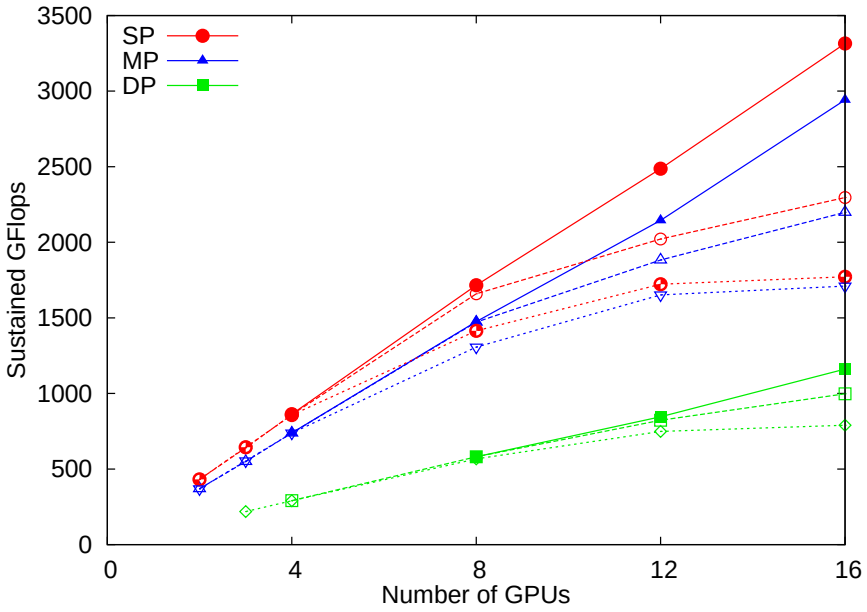

Figure 5.6: Strong scaling on the Tesla C2070. The spatial lattice volume is kept fixed at 64^3 and the total temporal extent varies for the three lines (per precision) from the top downwards $N_t = 256, 128, 96$.

5.6.3 Comparison to existing CPU code

Lastly, we compare our performance to the overrelaxation kernel of the *FermiQCD* library [143]. The *FermiQCD* toolbox is open source (C++) and has been designed to be easy to use while at the same time offering the user many applications for lattice QCD, in some applications at the expense of performance. To our knowledge, it is the only publicly available code that supports lattice gauge fixing with the overrelaxation algorithm in Landau gauge. We would be happy to compare our code with a wider range of implementations.

As test bed we chose an Intel Xeon Westmere CPU on the mephisto cluster, see Sec. 5.6.2. We run the *FermiQCD* Landau gauge overrelaxation kernel in SP on a lattice of size 32^4 on a single core in avoidance to reflect parallelization artifacts. Then we compare the performance to our code (same lattice size and precision) from the Tesla C2070 that the cluster offers.

FermiQCD reaches a performance of 0.414 GFlops and our code reaches for this setup 195.08 GFlops. Thus, our implementation executed on the Tesla GPU is equivalent to *FermiQCD* executed on ≈ 470 CPU cores of the given type, under the naive assumption of linear scaling for the CPU code.

5.6.4 Temperature dependence of the simulated annealing algorithm

In Sec. 5.2.3 we discussed the importance of keeping the temperature gradient small in the simulated annealing. Therefore, it is crucial to set up the right temperature interval in order not to waste many iteration steps in a temperature region where the gauge functional is insensitive to.

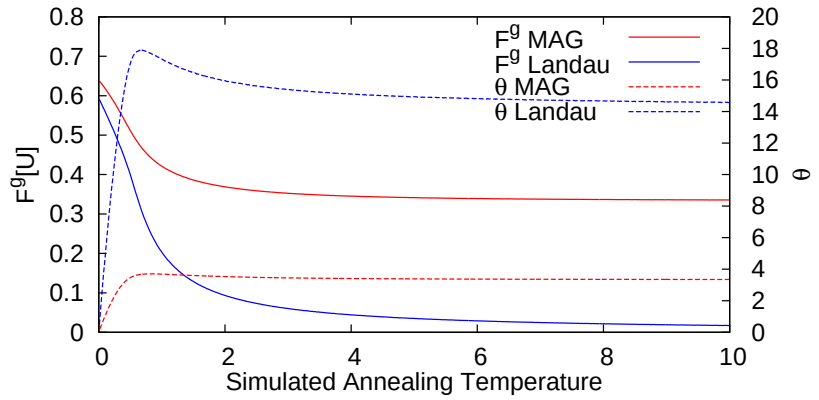

Figure 5.7: The temperature dependence in simulated annealing of the gauge functional $F^g[U]$ and the gauge precision θ of the Landau gauge and the maximally Abelian gauge.

In Fig. 5.7 we show an example of the evolution of the gauge functional $F^g[U]$ and the gauge precision θ of the Landau gauge and the maximally Abelian gauge. The simulation has been performed on a *hot gauge field*, i.e., having all gauge links set to random SU(3) matrices. The lattice size is 32^4 and for both cases 10,000 simulated annealing steps have been carried out.

As one can read of from the plot, in this case, the sensitive region where the gauge functional changes most is for Landau gauge below $T < 4$ and for the maximally Abelian gauge slightly lower, $T < 2$.

5.6.5 Cooling down to maximally Abelian gauge

Here, we aim at reducing the time and number of iterations to gauge fix a configuration to the maximally Abelian gauge. We test overrelaxation versus a combination of simulated annealing, stochastic relaxation and overrelaxation in terms of required number of iterations to gauge fix a sample gauge configuration with inverse coupling $\beta = 5.7$ and lattice size 32^4.

Both approaches use an overrelaxation parameter of $\omega = 1.35$, the second method starts off by applying 2000 simulated annealing steps including three microcanonical updates after each step (i.e., 8000 steps in total). Subsequently, a maximum of 2000 stochastic relaxation steps are applied and lastly overrelaxation until the precision $\theta < 10^{-12}$ is reached. Method one directly applies the overrelaxation kernel until convergence.

We started both variants on 100 randomly chosen points on the gauge orbit. Method one succeeded to find an optimum for 84 out of the 100 copies, the remaining 16 got stuck at a value of $\theta \approx 10^{-7}$ until the algorithm was stopped after one hundred thousand iterations. Method two was successful for 97 copies.

The average number of required iterations (the combined number of all updates) is given in Tab. 5.4, together with the final value of the gauge functional $F^g[U]$.

As it is evidence from the data, the combined approach of simulated annealing, stochastic relaxation and overrelaxation outperforms the pure overrelaxation method in terms of number of iterations by a factor of almost two and moreover reaches an higher average value of the gauge functional while bringing more gauge copies to converge. The average time spend by the device (GTX 580) per gauge copy was four minutes for method two and slightly below seven minutes for method one. It has to be stressed, however, that not all gauge copies converged and hence these copies enter the average of the execution time with a biased weight since the kernel was executed until the maximum number of iterations was reached.

5.6.6 Towards the global maximum of the Landau gauge functional

We take the same gauge field configuration with $\beta = 5.7$ and lattice size 32^4 of the previous subsection and now aim at finding Landau gauge Gribov copies with gauge functional values as high as possible. Three runs with 100 random starts on the gauge orbit have been performed. The difference of the three runs lies in the number of simulated annealing steps that are applied before the overrelaxation kernel takes over. We apply zero, three thousand or ten thousand simulated annealing steps, respectively. The temperature has been decreased from 4 down to 10^{-4}. Each simulated annealing step is followed by three microcanonical updates. Subsequently, we apply the overrelaxation kernel until $\theta < 10^{-10}$.

We determined the maximum gauge functional value of all the runs, which we denote by $F^g_{\max}$ and define the relative deviation from it by

$$F^g_{\text{rel}} = \frac{F^g_{\max} - F^g}{F^g_{\max}}. \tag{5.34}$$

	OR	SA/SR/OR
# of converged copies	83	97
# of iterations	272340 ± 8405	16701 ± 2562
$F^g[U]$	0.74356431(39697)	0.74423815(10996)

Table 5.4: Comparing the application of the overrelaxation algorithm (OR) solely, to the subsequent application of simulated annealing (SA) with microcanonical steps, stochastic relaxation (SR) and OR on 100 copies of a gauge field of lattice size 32^4.

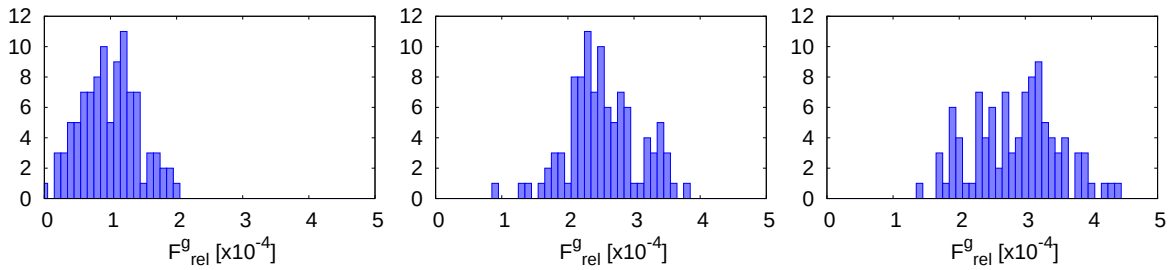

Figure 5.8: The relative deviation from the maximal gauge functional. From left to right with 10000, 3000 and zero simulated annealing steps.

The latter is plotted in histograms in Fig. 5.8 for all the three runs. The plot clearly demonstrates how the application of simulated annealing increases the chance to find the global maximum, especially on a relatively large lattice of size 32^4. This test has been performed in parallel on two Tesla C2070 devices within several hours.

5.7 Summary

We presented a CUDA implementation for gauge fixing in lattice gauge field theories based on the relaxation algorithms. The code is based on the cuLGT package[1] and supports the Landau, Coulomb and maximally Abelian gauge fixing conditions.

The implementation and the various optimization strategies have been discussed in detail. We showed that simulated annealing and overrelaxation can heavily be accelerated by employing GPUs. We listed convergence results in different floating point precisions and concluded that a mixed precision ansatz that performs only the critical parts of the simulation in double precision is a good compromise in terms of precision ($\sim 10^{-5}$ relative to DP) and performance ($80\% - 90\%$ of SP).

A maximum sustained performance of 370 GFlops on a single GTX 580 has been reached and moreover linear scaling on 16 Tesla cards with 3.5 Teraflops, given that the number of time-slices per device does not fall below 16.

Lastly, we demonstrated how the combination of simulated annealing and the various relaxation flavors can be tuned in such a way that either fast convergence to the gauge of choice is reached or alternatively that a gauge functional value as high as possible is obtained.

We are currently preparing tests on the Kepler architecture, updates on Kepler performance will be available on our homepage shortly.

1 Both is available for downloaded under www.cuLGT.com.

Chapter 6

Locality, sea quarks and more

In this chapter additional, yet unpublished material on the subject of Dirac low-mode truncation and artificial chiral restoration is collected. In particular, in Sec. 6.1 we demonstrate that locality violation is small for the truncated Dirac operators that we construct. In Sec. 6.2, we present a possible extension of Dirac low-mode truncation to the sea quark sector that relies on a reweighting method and, finally, in Sec. 6.3 we test an alternative method to artificially restore the chiral symmetry, which is not based on Dirac low-mode truncation.

6.1 Locality properties of the truncated CI Dirac operator

Locality of the Dirac operator is a vital property for a quantum field theory since it ensures the causality of the theory. The original CI Dirac operator is, like the Wilson operator, *ultra local* by definition. The Neuberger overlap operator, on the contrary, must violate locality at finite lattice spacing [144]. The authors of [145] have shown, though, that the nonlocal contributions of the overlap operator fall exponentially with the distance r/a to the source point and thus, in the naive continuum limit locality will eventually be restored. It is not clear a priori to what extent the exclusion of the low lying part of the Dirac eigenspectrum, like done in this work, violates the locality of a Dirac operator like the CI operator. The latter will be analyzed here.

The magnitude of the nonvanishing contributions of a column of the (hermitian) Dirac operator to the source point, as a function of the distance to the source serves as a measure of locality [145]. A single column of the Dirac operator is given by

$$\psi(x)^{[x_0,\alpha_0,a_0]} = \sum_y D_5(x,y)\,\eta(y)^{[x_0,\alpha_0,a_0]} \tag{6.1}$$

where we use matrix/vector notation in color and Dirac space and the multiindex $[x_0,\alpha_0,a_0]$ labels a point-source

$$\eta_a^\alpha(y)^{[x_0,\alpha_0,a_0]} = \delta(y-x_0)\,\delta_{\alpha\alpha_0}\,\delta_{aa_0}\ . \tag{6.2}$$

In practice we set $x_0 = 0$ without loss of generality. Eq. (6.1) defines a set of 12 columns of the Dirac matrix, one for each combination of color a_0 and Dirac α_0 indices.

In the following we want to investigate how $\psi(x)$ falls as we move away from the source-point $x_0 = 0$. Hence we define the distance of a point x to the origin on a d-dimensional lattice with periodic boundary conditions,

$$\mathbb{I}\, x\, \mathbb{I} := \left(\sum_{\mu=1}^{d} \min\left(x_\mu,\, N_\mu - x_\mu\right)^2\right)^{1/2} . \tag{6.3}$$

Next, we define a function that gives us the upper bound to the contributions from $\psi(x)$ as a function of the distance r to the source

$$f(r) = \max_{x,\alpha_0,a_0} \left\{ \|\psi(x)\| \mid \mathbb{I}\, x\, \mathbb{I} = r \right\} \tag{6.4}$$

where $\|\cdot\|$ is the usual vector norm over the internal color and Dirac structures of $\psi(x)$. Then we can analyze the expectation value $\langle f(r)\rangle$, which serves as a measure for the violation of locality.

We adopt a subset of 59 configurations of the same dynamical configurations as in the foregoing part of this thesis and we apply the CI operator according to (6.1) with the same parameters as before. First, we plot Eq. (6.4) for the original (untruncated) CI Dirac operator in Fig. 6.1, which trivially shows its ultra locality. Note that the most distant nonzero contribution lies at $\sqrt{5}$, which stems from paths of length two in the μ-direction and length one in the ν-direction, $\nu \neq \mu$.

Subsequently, we study (6.4) for the low-mode truncated Dirac operator D_5, i.e., we consider columns of the truncated operator

$$\psi(x)^{[x_0,\alpha_0,a_0]}_{\mathrm{red}(k)} = \sum_y D_5(x,y)\eta(y)^{[x_0,\alpha_0,a_0]} - \sum_{i=0}^{k} \mu_i v_i(x) \sum_y v_i(y)^\dagger \eta(y)^{[x_0,\alpha_0,a_0]} \tag{6.5}$$

where the μ_i are the eigenvalues of D_5 and v_i the corresponding eigenvectors. Therefrom we calculate $\langle f(r)\rangle$ for truncation steps in powers of 2 from $k = 2,\ldots,128$, see Fig. 6.2. First, we observe that the deviation from the nonzero contributions of the full operator are of the order of 10^{-5}, as can be seen from the inner plot of the figure, and thus are very small. Moreover, the truncated Dirac operator collects some nonlocal contributions of similar order, $10^{-8} - 10^{-5}$,

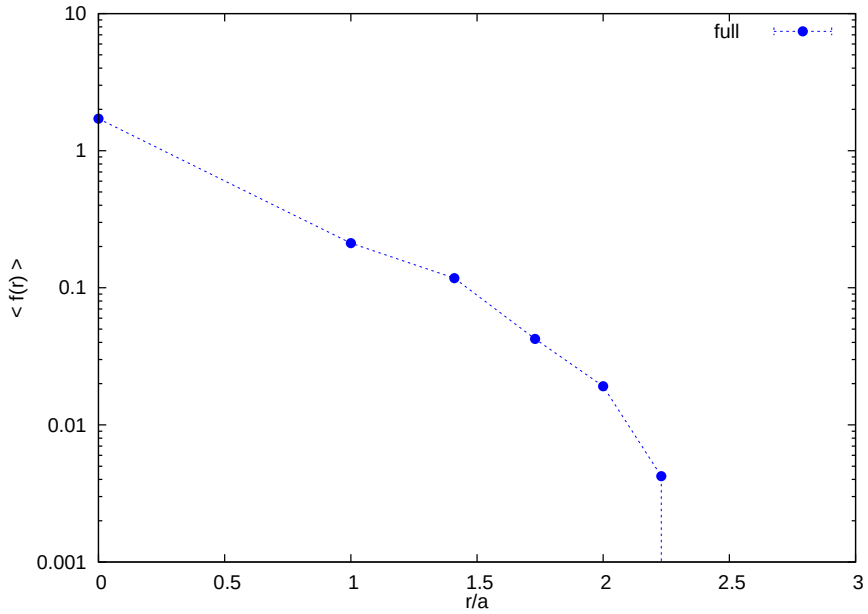

Figure 6.1: The expectation value $\langle f(r) \rangle$ for the full (untruncated) CI Dirac operator.

from distant points on the lattice. These contributions show, for $k \geq 32$, an exponential decay as function of the distance.

The continuum limit, however, is more subtle in this case: as we move towards smaller lattice spacings at constant volume, the number of eigenvalues increases with the number of lattice points $|\Lambda| = N_s^3 N_t$. Hence, if we want to keep the eigenmode cutoff constant in physical units, the number of eigenmodes that we have to include grows with a^{-4}, due to the volume scaling, but decreases only linearly with the energy scale a. Consequently, the number of eigenmodes we have to include in order to keep the physical cutoff constant, grows with a^{-3} and the nonzero contributions to $\langle f(r) \rangle$ grow at least linearly with the number of eigenmodes k. If the exponential decay we observe in Fig. 6.2 persists for higher k, it would account for the a^{-3} dependence of the number of modes but in order to draw concrete conclusions a more detailed numerical analysis would be advisable.

Nevertheless, this investigation points out that for our specific setup at finite lattice spacing the nonlocal contributions are very small and mostly do not affect our results.

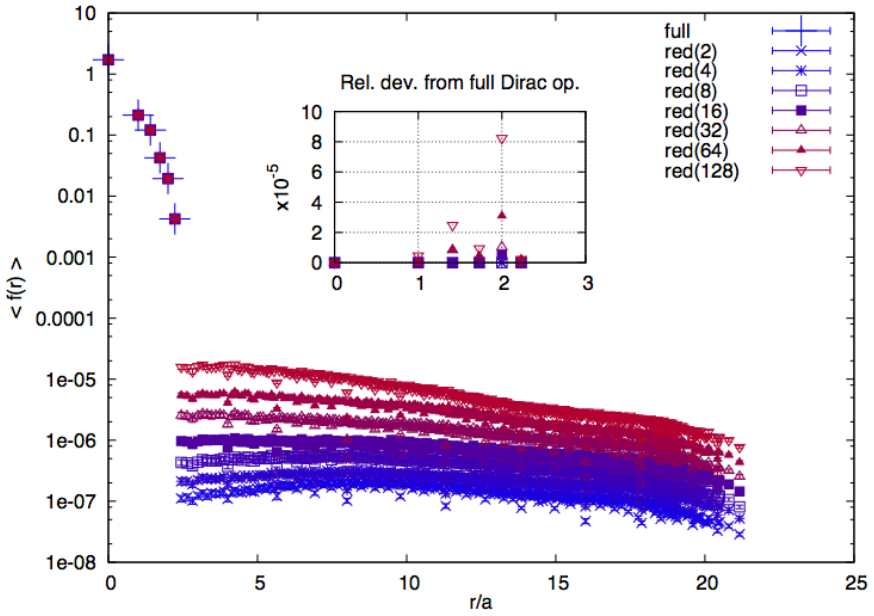

Figure 6.2: The expectation value $\langle f(r) \rangle$ for the truncated CI Dirac operator. Small nonlocal contributions are present.

6.2 The sea quark sector

Throughout this work we left the two flavors of dynamical fermions of the gauge field configurations untouched and only low-mode truncated the valence quark sector. Here we elaborate how the sea quark sector can in principle be low-mode truncated *a posteriori* via a reweighting procedure of the configurations.

We recall from Sec. 1.1.3 that we calculate observables $\mathcal{O}$ on the lattice via

$$\langle \mathcal{O}[U] \rangle = \frac{\int \mathcal{D}U \ \mathrm{e}^{-S_G[U]} \det[D_u] \det[D_d] \mathcal{O}[U]}{\int \mathcal{D}U \ \mathrm{e}^{-S_G[U]} \det[D_u] \det[D_d]} . \tag{6.6}$$

In the latter expression the fermionic degrees of freedom have been integrated out and consequently the fermion determinant of the quarks arises. In the following we assume the two light quark flavors to be degenerate, i.e., we can write

$$\det[D_u] \det[D_d] \equiv (\det[D])^2 . \tag{6.7}$$

The fermion determinant can be written as the product of the Dirac eigenvalues λ_i:

$$\det[D] = \prod_{i \in \Lambda} \lambda_i = \prod_{i \leq k} \lambda_i \cdot \prod_{i > k} \lambda_i \tag{6.8}$$

where in the second step we have split the product into a low-mode part and a reduced part

$$\det [D]_{\mathrm{lm}(k)} = \prod_{i \leq k} \lambda_i \,, \qquad \det [D]_{\mathrm{red}(k)} = \prod_{i > k} \lambda_i \,. \tag{6.9}$$

Then we can formally include a weight w_k, which we define as

$$w_k \equiv \left(\det [D]_{\mathrm{lm}(k)} \right)^{-2} , \tag{6.10}$$

into (6.6) in order to cancel the low-mode contribution of the fermion determinant

$$\langle \mathcal{O}[U] \rangle_{w_k} = \frac{\int \mathcal{D}U \;\; \mathrm{e}^{-S_G[U]} \left(\det [D] \right)^2 w_k \, \mathcal{O}[U]}{\int \mathcal{D}U \;\; \mathrm{e}^{-S_G[U]} \left(\det [D] \right)^2 w_k} \tag{6.11}$$

$$= \frac{\int \mathcal{D}U \;\; \mathrm{e}^{-S_G[U]} \left(\det [D]_{\mathrm{red}(k)} \right)^2 \mathcal{O}[U]}{\int \mathcal{D}U \;\; \mathrm{e}^{-S_G[U]} \left(\det [D]_{\mathrm{red}(k)} \right)^2} . \tag{6.12}$$

Consequently, only the reduced part of the fermion determinant remains in the path integral to represent the sea quarks. In the next step we replace the integration over the gauge fields in (6.11) with a Monte Carlo integration, which yields

$$\langle \mathcal{O}[U] \rangle_{w_k} \approx \frac{\sum_n \mathcal{O}[U_n] \, w_k[U_n]}{\sum_n w_k[U_n]} \tag{6.13}$$

where the finite number of gauge field configurations $U_n, n = 1, \ldots, N$, have been generated with the standard weight factor $\mathrm{e}^{-S_G[U]} \left(\det [D] \right)^2$.

To test the practicability of the above described reweighting scheme, we first study the magnitude and the fluctuations of the weight factor w_k defined in (6.10). We use the identical setup as before and adopt the eigenvalues of D itself (not of D_5) to study the expectation value of w_k,

$$\langle w_k[U] \rangle = \frac{1}{N} \sum_n w_k[U_n] \,. \tag{6.14}$$

The values $\langle w_k \rangle$ with jackknife error bars for different k are shown in Fig. 6.3 and the standard deviation over the mean value,

$$\frac{\sqrt{\mathrm{Var}(w_k)}}{\langle w_k \rangle} = \frac{\sqrt{\langle w_k^2 \rangle - \langle w_k \rangle^2}}{\langle w_k \rangle} , \tag{6.15}$$

is shown in Fig. 6.4. From the plots we see that the weight factors from the definition (6.10) are extremely large. To compensate therefor we can bring (6.13) in a form more similar to the

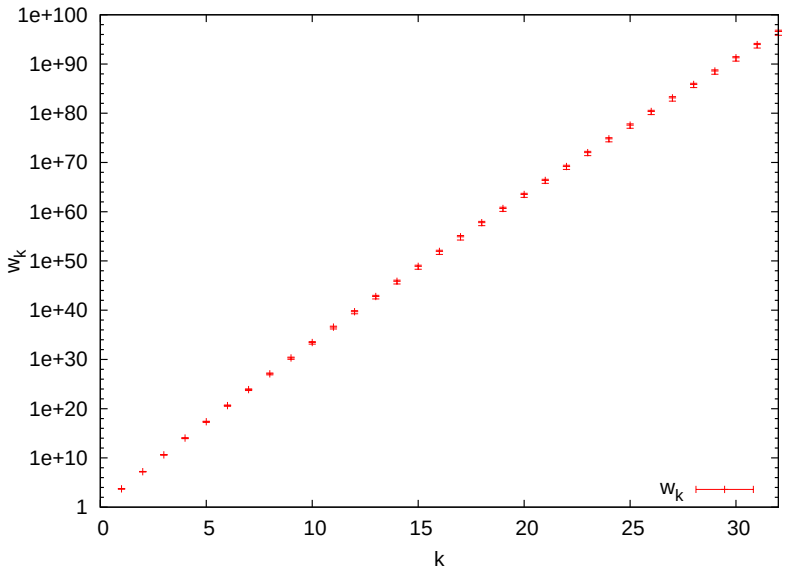

Figure 6.3: The weight factor $\langle w_k \rangle$ from the Monte Carlo integration as a function of the truncation level k.

unweighted case by defining the ratio

$$\overline{w}_k \left[U_n\right] \equiv \frac{w_k \left[U_n\right]}{\sum_n w_k \left[U_n\right]} \cdot N \ . \tag{6.16}$$

Therewith we can rewrite (6.13) to obtain

$$\left\langle \mathcal{O}\left[U\right] \right\rangle_{w_k} \approx \frac{1}{N} \sum_n \mathcal{O}\left[U_n\right] \overline{w}_k \left[U_n\right] \ , \tag{6.17}$$

which differs from the unweighted case (1.31) only by the factors $\overline{w}_k \left[U_n\right]$, which multiply the observable $\mathcal{O}\left[U_n\right]$ on each configuration that enters into the Monte Carlo integration.

In Fig. 6.5 we show the distribution of the values $\overline{w}_k$ for $k = 2, 10, 20, 30$ from our set of 161 gauge field configurations. Unfortunately, this shows that for truncation levels $k \geq 20$, that is the level of interest for the restoration of the chiral symmetry (see Chap. 2), the Monte Carlo sum is highly dominated by very few gauge configurations. Therefore, we would need many more (uncorrelated) gauge field configurations in order to obtain the same statistics as before. There is a chance, however, that the distribution of the weight factors is narrower for overlap fermions due to the strict circular distribution of the eigenvalues of the overlap operator in the complex plane, opposed to the eigenvalues of the CI that are spread with respect to the circle.

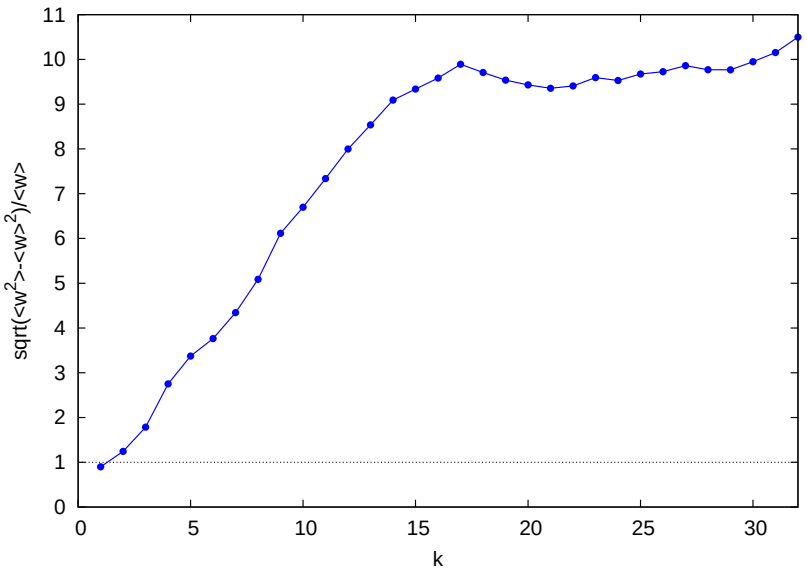

Figure 6.4: The ratio $\sqrt{\langle w_k^2\rangle - \langle w_k\rangle^2}/\langle w_k\rangle$.

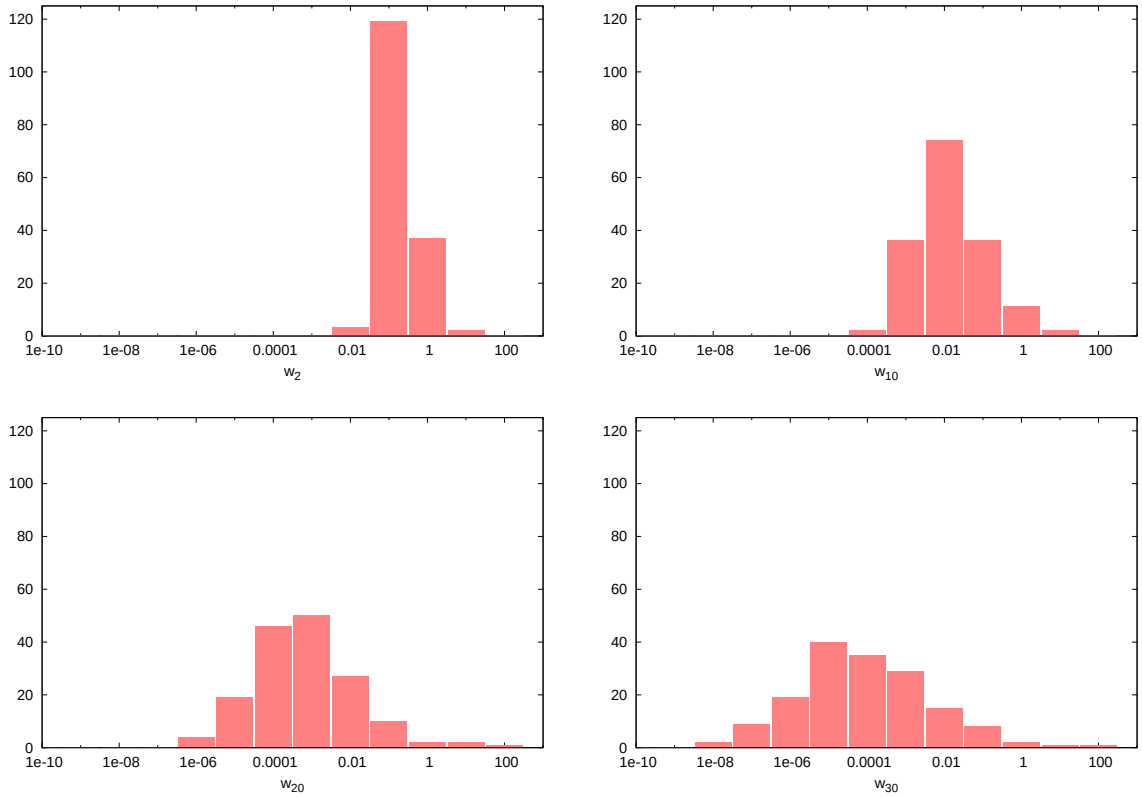

Figure 6.5: Histograms of the values $\overline{w}_k$ for $k = 2$ (top left), $k = 10$ (top right), $k = 20$ (bottom left) and $k = 30$ (bottom right) from a set of 161 gauge field configurations.

6.3 An alternative trial to artificially restore the chiral symmetry

Here we present another approach of artificially restoring the chiral symmetry that is not based on Dirac low-mode truncation but on the decomposition of the (interacting) quark propagator in its Clifford algebra elements.

6.3.1 Motivation

We remind the reader that the (continuum) tree-level quark propagator in momentum space consists of a Dirac vector and a Dirac scalar part,

$$S_0(p) = (i\not{p} + m)^{-1} . \tag{6.18}$$

Assuming the quark propagator retains this general decomposition in the interacting case one can write it as

$$S(p) = (i\not{p}A(p) + B(p))^{-1} . \tag{6.19}$$

The dynamical breaking of the chiral symmetry, and accordingly the formation of a chiral condensate, is equivalent to an infrared enhancement of the scalar function $B(p)$. Here we restore chiral symmetry by partially turning off the interactions of the quark propagator with the gluon fields, to be precise, we replace the scalar function $B(p)$ by its tree-level form, while leaving the interactions in $A(p)$ fully intact. Then we construct color-singlet hadron correlators out of these quark propagators, thus no gauge fixing is necessary here.

6.3.2 Details

Lattice quark propagator in momentum-space

Due to discretization artifacts, the lattice tree-level quark propagator differs from (6.18):

$$S_0(p) = (ia\not{k}(p) + B_0(p))^{-1} , \tag{6.20}$$

where the lattice momenta $k_\mu(p_\mu)$ and the tree-level scalar function $B_0(p)$ that are functions of the discrete momenta p_μ, are known analytically, see, e.g., Appendix A.1 for the CI Dirac operator.

The CI Dirac operator includes, by construction, not only Dirac scalar and vector parts but all 16 elements of the Clifford algebra. Thus our interacting lattice quark propagator has the

general form

$$S(p) = \left(B(p)\mathbb{1} + i\sum_{\mu} V_\mu(p)\gamma_\mu + \sum_{\mu} X_\mu(p)\gamma_5\gamma_\mu + \sum_{\mu,\nu<\mu} T_{\mu\nu}(p)\gamma_\mu\gamma_\nu + P(p)\gamma_5 \right)^{-1} \tag{6.21}$$

where the functions $B(p)$ and $V_\mu(p)$ are real, whereas the axial vector $X_\mu(p)$, tensor $T_{\mu\nu}(p)$ and pseudoscalar $P(p)$ contributions are complex.

The method

Here we explain how we can replace $B(p)$ with the tree-level form $B_0(p)$ in existing lattice quark propagators. Note that this would correspond to replacing $B(p)$ with the bare quark mass m in the continuum.

First, we Fourier transform all four space-time directions of the lattice quark propagator to momentum space,

$$S^{\alpha\beta}_{ab}(x,0) \quad \rightarrow \quad S^{\alpha\beta}_{ab}(p)\,, \tag{6.22}$$

for all color and Dirac components. The discrete momenta p are defined as

$$\begin{aligned} p_0 &= \frac{2\pi}{aN_t}\left(n_0 + \frac{1}{2} - \frac{N_t}{2}\right), \\ p_i &= \frac{2\pi}{aN_s}\left(n_i + 1 - \frac{N_s}{2}\right). \end{aligned} \tag{6.23}$$

Next, we define

$$D^2(p) = B^2(p) + \sum_{\mu} V^2_\mu(p) + \sum_{\mu} X^2_\mu(p) + \sum_{\mu,\nu<\mu} T^2_{\mu\nu}(p) + P^2(p) \tag{6.24}$$

and moreover the dressing functions $\mathcal{B}(p)$, $\mathcal{V}_\mu(p)$, $\mathcal{X}_\mu(p)$, $\mathcal{T}_{\mu\nu}(p)$ and $\mathcal{P}(p)$ such that

$$S(p) = \mathcal{B}(p)\mathbb{1} - i\sum_{\mu} \mathcal{V}_\mu(p)\gamma_\mu + \sum_{\mu} \mathcal{X}_\mu(p)\gamma_5\gamma_\mu + \sum_{\mu,\nu<\mu} \mathcal{T}_{\mu\nu}(p)\gamma_\mu\gamma_\nu + \mathcal{P}(p)\gamma_5\,, \tag{6.25}$$

which are related to the functions from (6.21) by factors $1/D^2(p)$. The latter dressing functions

can be extracted from (6.25) as

$$\mathcal{B}(p) = \frac{1}{4}\,\mathrm{tr}\,[S(p)]\ , \tag{6.26}$$

$$\mathcal{V}_\mu(p) = \frac{i}{4}\,\mathrm{tr}\,[\gamma_\mu S(p)]\ , \tag{6.27}$$

$$\mathcal{X}_\mu(p) = \frac{1}{4}\,\mathrm{tr}\,[\gamma_\mu\gamma_5 S(p)]\ , \tag{6.28}$$

$$\mathcal{T}_{\mu\nu}(p) = \frac{1}{4}\,\mathrm{tr}\,[\gamma_\nu\gamma_\mu S(p)]\ , \tag{6.29}$$

$$\mathcal{P}(p) = \frac{1}{4}\,\mathrm{tr}\,[\gamma_5 S(p)] \tag{6.30}$$

where the trace goes over Dirac space. Note that we carry this procedure out for all color components of the quark propagator individually. Therefrom we obtain the original dressing functions of (6.21), when dividing by $\mathcal{D}^2(p)$ which is defined equivalently to (6.24).

In the last step, we simply replace $B(p)$ by $B_0(p)$ and reassemble the quark propagator,

$$S(p) = \frac{B_0(p)\mathbb{1} - i\sum_\mu V_\mu(p)\gamma_\mu + \sum_\mu X_\mu(p)\gamma_5\gamma_\mu + \sum_{\mu,\nu<\mu} T_{\mu\nu}(p)\gamma_\mu\gamma_\nu + P(p)\gamma_5}{D^2(p)}\,. \tag{6.31}$$

Consistency check

For the purpose of checking the consistency of the whole procedure, we Fast-Fourier-Transform (FFT) a sample quark propagator and subsequently decompose it according to the above description, assemble it again without replacing $B(p)$ by $B_0(p)$ and perform the inverse FFT. Agreement of all elements of the quark propagator before and after the decomposition proves consistency.

Relation to Dirac low-mode truncation

In Fig. 6.6 the functions $A(p) = \sum_\mu V_\mu/k_\mu$ and $B(p)$ of (6.21) are shown for the full case and after having subtracted the lowest 16 and 32 Dirac eigenmodes. Here, the configurations have been fixed to Landau gauge.

As can be seen from the plot, the influence of Dirac low-mode truncation is much more severe on $A(p)$ than on $B(p)$. Thus, low-mode truncation removes the chiral condensate in the renormalization point invariant mass function $M(p) = B(p)/A(p)$ by enhancing $A(p)$ instead of by suppressing $B(p)$.

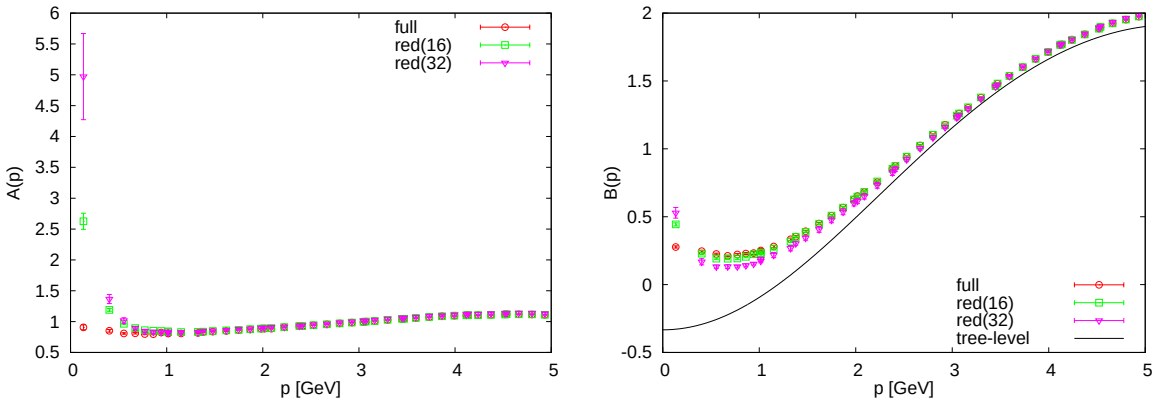

Figure 6.6: The functions $A(p)$ and $B(p)$ for the full case and after having subtracted the lowest 16 and 32 Dirac eigenmodes.

6.3.3 Results

We tested the method for the π (0^{-+}), a_0 (0^{++}), ρ (1^{--}), a_1 (1^{++}) and b_1 (1^{+-}) mesons and the nucleon and Delta baryons. Each with only a single interpolator (Jacobi smeared "narrow") using 100 configurations for the mesons and 300 for the baryons.

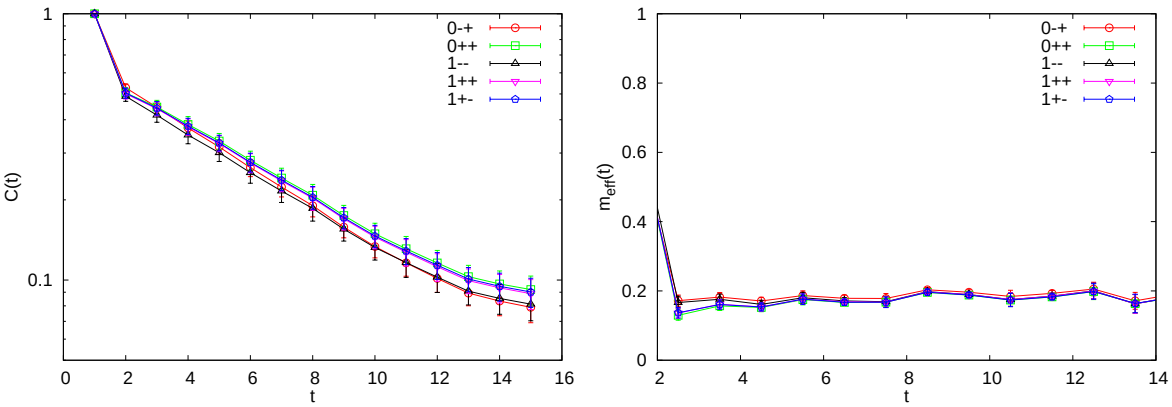

Figure 6.7: Correlator and effective mass plots of the π (0^{-+}), a_0 (0^{++}), ρ (1^{--}), a_1 (1^{++}) and b_1 (1^{+-}) mesons after the scalar part $B(p)$ has been replaced with its tree-level form $B_0(p)$.

In Fig. 6.7 we show the results for the mesons that we obtain after the scalar part $B(p)$ has been replaced with its tree-level form $B_0(p)$. It is evident that this approximation implies degeneracy of all mesons under study. The degeneracy of ρ and a_1 can be accounted for by the restoration of the chiral symmetry, whereas the degeneracy of a_0 and π signals the restoration of the $U(1)_A$ symmetry, equivalently the degeneracy of ρ and b_1. Then the question remains why the groups ρ, a_1, b_1, on the one hand and π, a_0, on the other hand, are degenerate as well. One could argue that the pseudoscalar state, the pion, in a chirally symmetric world, has no

reason to have a different mass to, e.g., the rho meson.

Alternatively we have to consider the possibility that we do not obtain confined states anymore, but find only freely traveling quarks. The correlators of the baryons under this kind of truncation, see Fig. 6.8, do not show clean exponential decays at all, which strengthens the argument that confinement does not survive the replacement of the Dirac scalar part by its tree-level form. Surprisingly, however, the weak signal of a state in the baryon channels has a mass much higher than $3/2$ times the masses of the mesonic states, which one would expect if one was confronted with free quarks. Interestingly, though, the correlators of $N(+)$ and $\Delta(+)$ are similar to each other and furthermore the correlators of $N(-)$ and $\Delta(-)$.

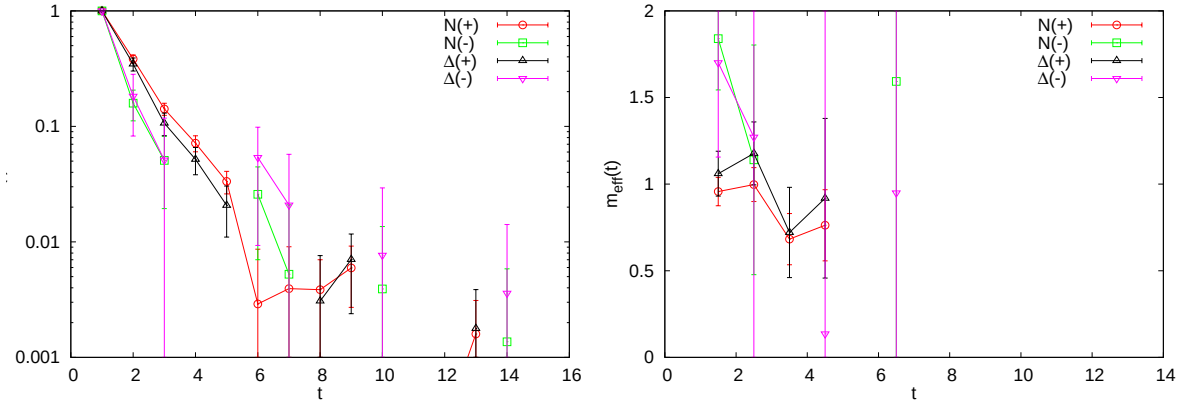

Figure 6.8: Correlator and effective mass plots of the nucleon and Δ of both parities after the scalar part $B(p)$ has been replaced with its tree-level form $B_0(p)$.

In summary, at the current stage, profound conclusions on the effects of replacing the scalar part of the Dirac operator with its tree-level form cannot be drawn. A future study could profit from the adoption of exact chirally symmetric fermions that do not obtain an additive mass renormalization.

Chapter 7

Conclusions

In this thesis, the interrelation between dynamical chiral symmetry breaking (DχSB) and confinement in QCD has been studied. To this end, we were motivated by the Banks–Casher relation, which connects the low lying Dirac eigenmodes to DχSB, to remove the chiral condensate from the valence quark sector by hand. We constructed valence quark propagators on two-flavor dynamical configurations, which omit a variable-sized part of the lowest Dirac eigenmodes. Plugging these modified quark propagators into meson and baryon interpolators enabled us to draw conclusions on the fate of confinement in a world without chiral symmetry breaking.

7.1 Low-mode truncated quarks

What happens to the valence quarks when we remove the lowest eigenmodes? First of all, it has to be stressed that, against naive assumptions, this procedure does not crucially violate the locality of the theory. By construction, removing a part of the eigenspectrum violates locality to some extent. We have shown in Sec. 6.1, that the nonlocal contributions to the truncated Dirac operator are of the order of one million times smaller than the local contributions, and moreover, fall exponentially with the distance at finite lattice spacing. Therefore, the influence of nonlocal contributions can be neglected. Consequently, we are still confronted with a causal quantum field theory on the lattice. Nevertheless, the modifications we applied to the quark propagators clearly render the theory different to conventional lattice QCD. This gives rise to the question: what exactly is different? What happens to the quarks upon Dirac eigenmode truncation?

In Chap. 3 we investigated the quark propagator in a gauge fixed setting under Dirac low-mode

removal, with the goal of finding the effects thereof on the quark wavefunction renormalization function and on the quark mass function which exhibits the dynamical generation of mass due to DχSB. The first observation was that removing the lowest Dirac modes causes the dynamical mass generation to cease, while the value of the bare mass (which is also connected to the lowest Dirac eigenmodes) is not affected. The truncation level $k \approx 128$, at which the quark mass function appears flat, must coincide with the level of complete removal of the chiral condensate from the valence quark sector. Not only the mass function is affected by Dirac low-mode truncation, the quark wavefunction renormalization function has also been found to be strongly suppressed when subtracting more and more low-modes. Infrared suppression of the wavefunction renormalization function, which appears as an overall factor of the renormalized quark propagator, can be interpreted as suppression and eventual extinction of low-momentum quarks in the spectrum. The latter is in accordance with the observation that the low-momentum states of quarks are directly connected to low Dirac eigenvalues as we derived explicitly in Sec. 1.4.4 for the case of free quarks.

In summary, the effects of Dirac low-mode removal on the fundamental fermionic degrees of freedom of QCD include the following: first, the dynamical mass generation of the quarks vanishes, signalling the restoration of the chiral symmetry. Secondly, the momentum of the quarks is increased compared with the full theory.

7.2 The hadron spectrum from low-mode truncated quarks

What does the hadron spectrum from low-mode truncated quarks look like? Most important is the observation that all hadron states we studied (except for a pion from the pseudoscalar interpolator) persist in the modified theory. Moreover, the signals of the exponentially decaying correlator functions became essentially better as compared to the full theory. This amounts to the fact that the noise in correlators is dominated by the lowest Dirac eigenvalues which enter inversely in the quark propagators and thus in the hadron interpolators.

The persistence of exponentially decaying states allowed the extraction of effective mass values from these states. Mass degeneracies of 'would-be' chiral partners confirm the restoration of the dynamically broken chiral symmetry. While we clearly observe the restoration of chiral symmetry, the splitting between currents that are related via the flavor singlet axial transformation persists, and we conclude that the $U(1)_A$ symmetry, which is not only broken spontaneously but also explicitly by the anomaly, does not get restored. The axial anomaly is related to the real eigenmodes of the Dirac operator (Sec. 1.4.1) and our maximum truncation level does not cover all these real modes (Fig. A.5). Moreover, there are arguments [146, 147, 148] that in high temperature QCD with two light flavors, when chiral symmetry becomes restored, the effects of $U(1)_A$ violation in two-point functions of quark bilinears remain. However, so the authors of

the aforementioned studies, for three or more light flavors $\mathrm{U}(1)_A$ violation cannot be observed in two-point functions beyond the chiral phase transition.

Interestingly, matching of the masses of most of the chiral partners is found at an earlier truncation level than suggested by the vanishing of the dynamically generated mass of quarks: degenerate states of, e.g., the vector and axial vector currents are observed at truncation level $k \approx 16$ while, as discussed above, the chiral condensate decreases with the truncation level until it disappears completely only at $k \approx 128$. This can be explained by considering the increased momenta of the quarks under Dirac low-mode removal. The early chiral restoration, as displayed by the degeneracy of states, must be an effective restoration that is a combination of two underlying phenomena: first, the dynamically generated mass of the quarks has shrunk to about sixty percent of its original value and second, the momenta of the quarks are increased such that the effective dynamical mass at that momentum tends towards zero. Overall, the effects of removing the lowest Dirac modes can be summarized diagrammatically as presented in Fig. 7.1.

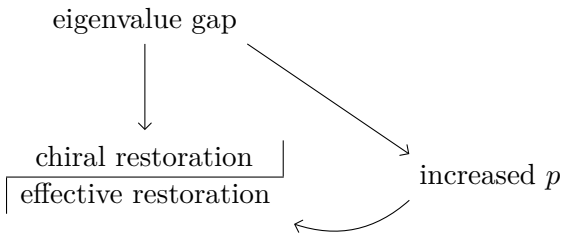

Figure 7.1: The chiral condensate emerges from the density of the lowest lying Dirac eigenmodes. On the other hand, these low-modes bear a relation to the momenta of the quarks. As shown in this work, artificially removing these low-modes has a twofold effect: it restores the chiral symmetry and it increases the average momenta of the quarks within the hadrons. Thereby, one has to distinguish between the effective chiral restoration due to the increased quark momenta and the actual chiral restoration, i.e., the vanishing of the quark condensate.

7.3 Mass generation in QCD

How is the mass of hadrons containing light quarks generated? It is often believed that DχSB accounts for the main bulk of mass in light hadrons such as the rho and the nucleon. We find, however, that at low truncation levels where the chiral symmetry is (effectively) restored, the masses of these hadrons does not significantly reduce. Instead, the hadron mass even grows with higher truncation levels because the energy of the quarks is increased which is a remarkable consequence of the increasing of the quark momenta with the truncation level.

7.4 The interrelation between DχSB and confinement

Within this study, confinement survived the artificial restoration of the chiral symmetry. On the contrary, in lattice QCD thermodynamics, where high temperatures are introduced by a shortened temporal direction of the lattice causing a low-mode gap to form [149, 150, 151], the chiral restoration phase transition and the deconfinement phase transition coincide. Clearly, the difference is that in our work, the lowest Dirac modes have been set to zero by hand, while in high temperature lattice QCD, the gap forms due to the higher energies of the quarks stemming from the discretization on a shortened lattice in one direction.

Appendix A

Appendix

Sects. A.1 and A.2 consist of the original Appendices of Refs. [2, 4] (i.e., Chaps. 3 and 5), respectively. Ancillary, in Sec. A.3 we show the spectrum of the free Dirac operator and compare its lowest eigenvalues with the eigenvalues of the interacting operator. In the subsequent sections we discuss low-mode truncation based on eigenmodes of the Dirac operator D vs. low-mode truncation based on eigenmodes of the hermitian Dirac operator D_5, and we show the pion correlator on a small lattice built out of the low- and high-modes, where we vary the truncation level over the whole spectrum (Sec. A.4 and Sec. A.5, respectively).

A.1 Analytical expressions for the tree-level CI Dirac operator

At tree-level, the tensor, axialvector and pseudoscalar terms of Eq. (3.7) vanish identically and only scalar and vector terms remain [59]. When transformed to momentum space one obtains the following analytical expressions for the latter two: the scalar part, i.e., the tree-level mass

function which is plotted in Fig. 3.2 is given by

$$
\begin{aligned}
&M_L^{(0)}(p) = s_1 + 48s_{13} \\
&+ (2s_2 + 12s_8)(\cos(p_0) + \cos(p_1) + \cos(p_2) + \cos(p_3)) \\
&+ (8s_3 + 64s_{11})(\cos(p_0)\cos(p_1) + \cos(p_0)\cos(p_2) \\
&+ \cos(p_0)\cos(p_3) + \cos(p_1)\cos(p_2) + \cos(p_1)\cos(p_3) + \cos(p_2)\cos(p_3)) \\
&+ 48s_5(\cos(p_0)\cos(p_1)\cos(p_2) + \cos(p_0)\cos(p_1)\cos(p_3) \\
&+ \cos(p_0)\cos(p_2)\cos(p_3) + \cos(p_1)\cos(p_2)\cos(p_3)) \\
&+ 8s_6(\cos(p_0)\cos(2p_1) + \cos(p_0)\cos(2p_2) \\
&+ \cos(p_0)\cos(2p_3) + \cos(p_1)\cos(2p_2) + \cos(p_1)\cos(2p_3) + \cos(p_2)\cos(2p_3) \\
&+ \cos(2p_0)\cos(p_1) + \cos(2p_0)\cos(p_2) + \cos(2p_0)\cos(p_3) + \cos(2p_1)\cos(p_2) \\
&+ \cos(2p_1)\cos(p_3) + \cos(2p_2)\cos(p_3)) + 384s_{10}\cos(p_0)\cos(p_1)\cos(p_2)\cos(p_3) \\
&+ m_0,
\end{aligned}
$$

where the relevant coefficients are listed in Table A.1. In the same manner, the analytical expressions of the lattice momenta $k_\mu(p_\mu)$ from Fig. 3.1 read

$$
\begin{aligned}
k_0 &= 2v_1\sin(p_0) + 8v_2\sin(p_0)(\cos(p_1) + \cos(p_2) + \cos(p_3)) \\
&\quad + (32v_4 + 16v_5)\sin(p_0)(\cos(p_1)\cos(p_2) + \cos(p_1)\cos(p_3) \\
&\quad + \cos(p_2)\cos(p_3)), \\
k_1 &= 2v_1\sin(p_1) + 8v_2\sin(p_1)(\cos(p_0) + \cos(p_2) + \cos(p_3)) \\
&\quad + (32v_4 + 16v_5)\sin(p_1)(\cos(p_0)\cos(p_2) + \cos(p_0)\cos(p_3) \\
&\quad + \cos(p_2)\cos(p_3)), \\
k_2 &= 2v_1\sin(p_2) + 8v_2\sin(p_2)(\cos(p_0) + \cos(p_1) + \cos(p_3)) \\
&\quad + (32v_4 + 16v_5)\sin(p_2)(\cos(p_0)\cos(p_1) + \cos(p_0)\cos(p_3) \\
&\quad + \cos(p_1)\cos(p_3)), \\
k_3 &= 2v_1\sin(p_3) + 8v_2\sin(p_3)(\cos(p_0) + \cos(p_1) + \cos(p_2)) \\
&\quad + (32v_4 + 16v_5)\sin(p_3)(\cos(p_0)\cos(p_1) + \cos(p_0)\cos(p_2) \\
&\quad + \cos(p_1)\cos(p_2)).
\end{aligned}
$$

The wave-function renormalization function is equal to one at tree-level by construction.

s_1	$0.1481599252 \times 10^{1}$
s_2	$-0.5218251439 \times 10^{-1}$
s_3	$-0.1473643847 \times 10^{-1}$
s_5	$-0.2186103421 \times 10^{-2}$
s_6	$0.2133989696 \times 10^{-2}$
s_8	$-0.3997001821 \times 10^{-2}$
s_{10}	$-0.4951673735 \times 10^{-3}$
s_{11}	$-0.9836500799 \times 10^{-3}$
s_{13}	$0.7529838581 \times 10^{-2}$
v_1	$0.1972229309 \times 10^{0}$
v_2	$0.8252157565 \times 10^{-2}$
v_4	$0.5113056314 \times 10^{-2}$
v_5	$0.1736609425 \times 10^{-2}$
m_0	-0.077

Table A.1: The relevant D_{CI} coefficients. For a complete description see [59].

A.2 Counting flops

As we discussed in Sec. 5.2.4, the main work of Alg. 5.1 consists of applying the new update $g(x)$ to the neighboring links of site x, i.e., Step 2 of the algorithm. We will now analyze this more quantitatively. In Fig. A.1 we show the code snippet of cuLGT for the multiplication of a SU(3) matrix with a SU(2) subgroup element from the left. Here, the SU(2) subgroup element is stored as a an object of class *Quaternion* (Cayley–Klein four parameter representation).

As we can read of from the figure, in the loop over k we encounter four complex multiplications (six flop each) plus two complex additions (two flop each), thus $28 \cdot 3 = 84$ flop for the update of $U_\mu(x)$ and equivalently for $U_\mu(x - \hat{\mu})$. Consequently, the number of flop for Step 2, in four dimensions, sums up to $84 \cdot 2 \cdot 4 = 672$ per lattice site and SU(2) subgroup and hence to $672 \cdot 3 = 2016$ for SU(3).

As mentioned before, the above part is the same for all gauges and all update types. Only Step 1 of Alg. 5.1 distinguishes between different gauges and update types. Let us consider for example an overrelaxation update for Landau gauge. The latter consists of calculating $g(x)$ according to (5.19) plus a first order approximation of the exponentiation $g(x) \to g^{\omega}(x)$. In the cuLGT code, the sum of (5.19) is done on the *Quaternion* objects. Extracting the four reals of *Quaternion* representation of a SU(2) subgroup element of SU(3) requires four flop, see Fig. A.2. The *Quaternion* objects are then gathered in an array in shared memory (*shA*) according to (5.19). This means four flop (four additions) for each *Quaternion*. Thus the number of flop in (5.19) is eight per link variable and in 4D eight link variables are involved, i.e., 64 flop per lattice site and SU(2) subgroup iteration or 192 for SU(3).

Subsequently, the overrelaxation update $g(x) \to g^{\omega}(x)$ is calculated. Counting each operation in Fig. A.3 as one floating point operation (*rsqrt* corresponds to two operations), the *effective* number of flop for the overrelaxation update is 22 per lattice site and SU(2) subgroup, thus 66 for SU(3).

Summing up, the overrelaxation algorithm in SU(3) for Landau gauge requires

- 192 flop to gather the neighboring links $U_\mu(x)$, $U_\mu(x - \hat{\mu})$,
- 66 flop for the overrelaxation update,
- 2016 flop to apply the new $g(x)$ to $U_\mu(x)$, $U_\mu(x - \hat{\mu})$

and thus in total 2274 flop/site. Note that we do not take the extra Flops for the reconstruction of the third row of the SU(3) matrices into account.

For the heat bath kernel of the simulated annealing algorithm the number of flops cannot be calculated correctly because of the non-deterministic loops with random-number-dependent termination conditions. We counted the flops as if every loop is only run once and each RNG call is counted as one flop. Both choices are very conservative. Therefore, a comparison of simulated annealing implementations should be based on pure time measurements.

```
template<class Type>
void SU3<Type>::leftSubgroupMult( lat_group_dim_t i,
                lat_group_dim_t j, Quaternion<Real> *q )
{
        for( lat_group_dim_t k = 0; k < 3; k++ )
        {
                Complex<Real> IK = q->get( 0, 0 ) * get(i,k);
                IK += q->get( 0, 1 ) * get(j,k);

                Complex<Real> JK = q->get( 1, 0 ) * get(i,k);
                JK += q->get(1,1) * get(j,k);

                set( i, k , IK );
                set( j, k,  JK );
        }
}
```

Figure A.1: Multiplication of a SU(3) matrix by a SU(2) subgroup element in Quaternion representation from the left. The total number of flop is 84 per SU(2) subgroup iteration; see discussion in the text.

```
template<class Type>
Quaternion<Real> SU3<Type>::getSubgroupQuaternion(
                 lat_group_dim_t iSub, lat_group_dim_t jSub )
{
        Quaternion<Real> q;
        Complex<Real> temp;
        temp = mat.get(iSub,iSub);
        q[0] = temp.x;
        q[3] = temp.y;
        temp = mat.get(jSub,jSub);
        q[0] += temp.x;
        q[3] -= temp.y;
        temp = mat.get(iSub,jSub);
        q[2] = temp.x;
        q[1] = temp.y;
        temp = mat.get(jSub,iSub);
        q[2] -= temp.x;
        q[1] += temp.y;

        return q;
}
```

Figure A.2: Extracting a SU(2) subgroup element of SU(3) in *Quaternion* representation.

```
void OrUpdate::calculateUpdate( volatile Real (&shA)[4*NSB],
                                                short id )
{
        Real ai_sq = shA[id+NSB]   * shA[id+NSB]
                    +shA[id+2*NSB] * shA[id+2*NSB]
                    +shA[id+3*NSB] * shA[id+3*NSB];

        Real a0_sq = shA[id] * shA[id];

        Real b = (orParameter*a0_sq + ai_sq)/(a0_sq + ai_sq);
        Real c = rsqrt( a0_sq + b*b*ai_sq );

        shA[id] *= c;
        shA[id+NSB]   *= b*c;
        shA[id+2*NSB] *= b*c;
        shA[id+3*NSB] *= b*c;
}
```

Figure A.3: The overrelaxation update requires 22 flop per lattice site and SU(2) subgroup.

A.3 Eigenvalues of the free CI Dirac operator and formation of the chiral condensate

In Sec. 1.4.4 we derived an analytic expression for the eigenvalues of the free Dirac operator:

$$\lambda = s(p) \pm i\,|k(p)|\ , \tag{A.1}$$

where $s(p)$ is the scalar part of the Dirac operator, $k(p)$ is the vector part and p are the discrete momenta. See Appendix A.1 for the analytic expressions of $s(p)$ and $k(p)$ for the CI Dirac operator.

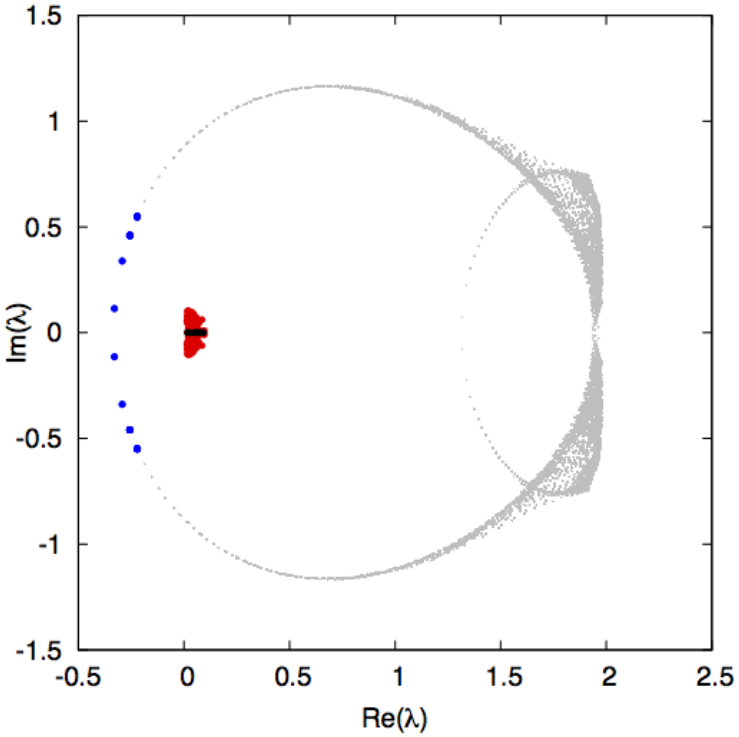

Figure A.4: Eigenvalues of the free CI Dirac operator (gray and blue) and the lowest 120 eigenvalues of the interacting operator (red and black).

As discussed in Chap. 3, the lowest $\sim$ 128 eigenmodes are connected to the dynamical generation of a mass and therefore to the chiral condensate. In Fig. A.4, the full spectrum of the free CI Dirac operator is compared to the lowest 120 eigenvalues of the interacting propagator from one sample configuration. In this figure, the lowest 120 eigenvalues of the free operator are shown in blue. Note the twofold degeneracy of the eigenvalues λ of Eq. (A.1), plus the additional degeneracies due to discrete rotational symmetry and parity symmetry on the lattice, for some of the points. When the interaction with the gluon fields is switched on,

these eigenvalues transform into the points in red and black. The black points correspond to the (real) would-be zero modes and the red points account for the near zero eigenvalue density that, according to the Banks–Casher relation, forms the chiral condensate. The shift of the eigenvalues towards larger real values, compared to the free case, signals an additive mass renormalization.

A.4 Eigenvalues of D vs. eigenvalues of D_5

For the investigation of the hadron mass spectrum under Dirac eigenmode truncation, presented in Chapters 2 and 4, we used 161 gauge configurations of size $16^3 \times 32$ with a lattice spacing $a = 0.1440(12)\,\mathrm{fm}$ [59]. These configurations include two degenerate flavors of light fermions with a resulting pion mass of $m_\pi = 322(5)\,\mathrm{MeV}$ and were generated with the chirally improved Dirac operator [45, 46], which is an approximate solution of the Ginsparg–Wilson equation.

Here we compare the properties of D and D_5, and to this end elaborate the advantages of D_5 over D, for our purposes, which justifies the adoption of D_5 in the aforementioned studies. We used valence quarks which are in mass and Dirac operator type equal to the sea quarks of the given configurations and we calculated the lowest modes (with respect to magnitude) of D and D_5 using the parallel version of the ARPACK package [61]. The latter is an implementation of the Arnoldi-method to calculate a part of the spectrum of arbitrary hermitian and non-hermitian matrices.

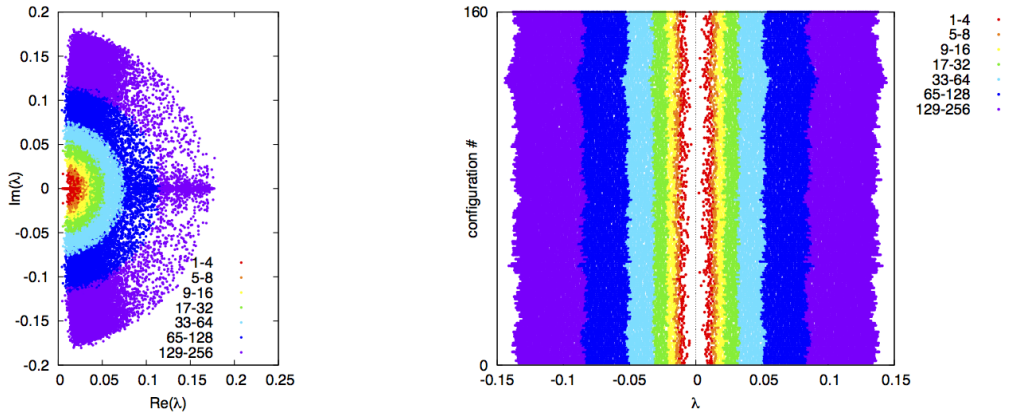

(a) D **(b)** D_5

Figure A.5: The 256 lowest (in terms of magnitude) eigenvalues, superimposed from 161 configurations.

In Fig. A.5 we show the lowest 256 eigenvalues of D and D_5, respectively, superimposed from all 161 configurations. Note that the eigenvalues of D_5 are real but not symmetrically spread with respect to zero. In Fig. A.6, histograms of the real part of the eigenvalues of D,

the absolute value of D and the absolute value of D_5 are plotted. Moreover, we integrated the three different histograms of Fig. A.6 to obtain Fig. A.7.

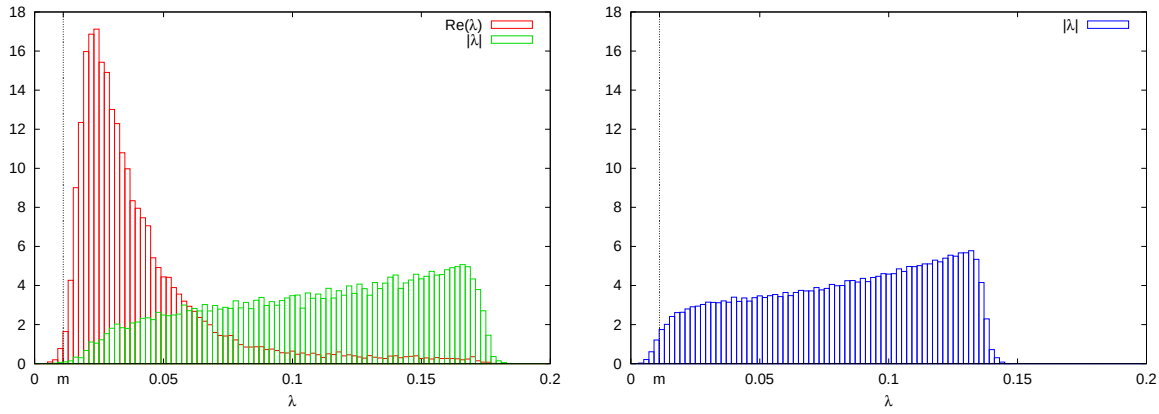

(a) D **(b)** D_5

Figure A.6: Histograms of the lowest 256 eigenvalues.

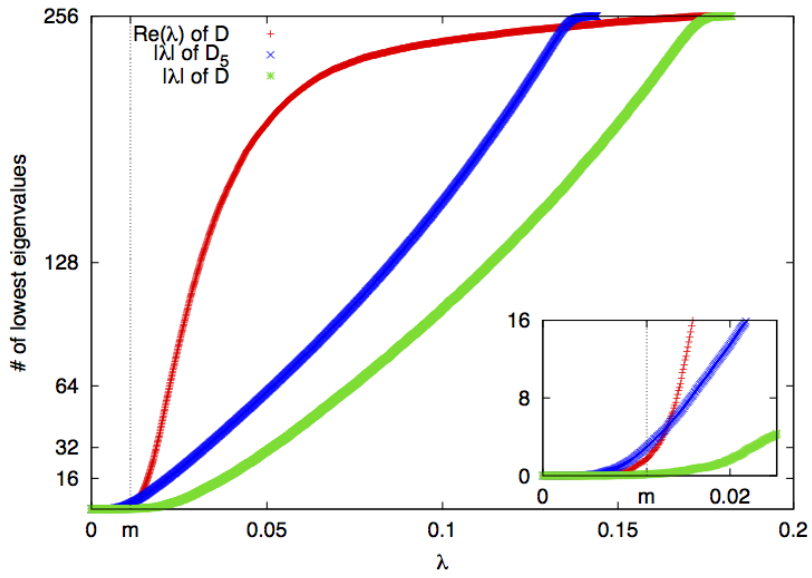

Figure A.7: Integrals over the histograms.

The question that naturally arose in our study was, whether to use the eigenvalues and eigenvectors of D or D_5 to construct truncated quark propagators and therefrom hadron correlators. In order to answer this question, we considered the saturation behavior of meson correlators from the low-modes of D and D_5.

Fig. A.8 shows the low-mode contribution to the pion correlator and Fig. A.9 equivalently the contribution to the rho correlator. As can be seen from these figures, fewer eigenmodes

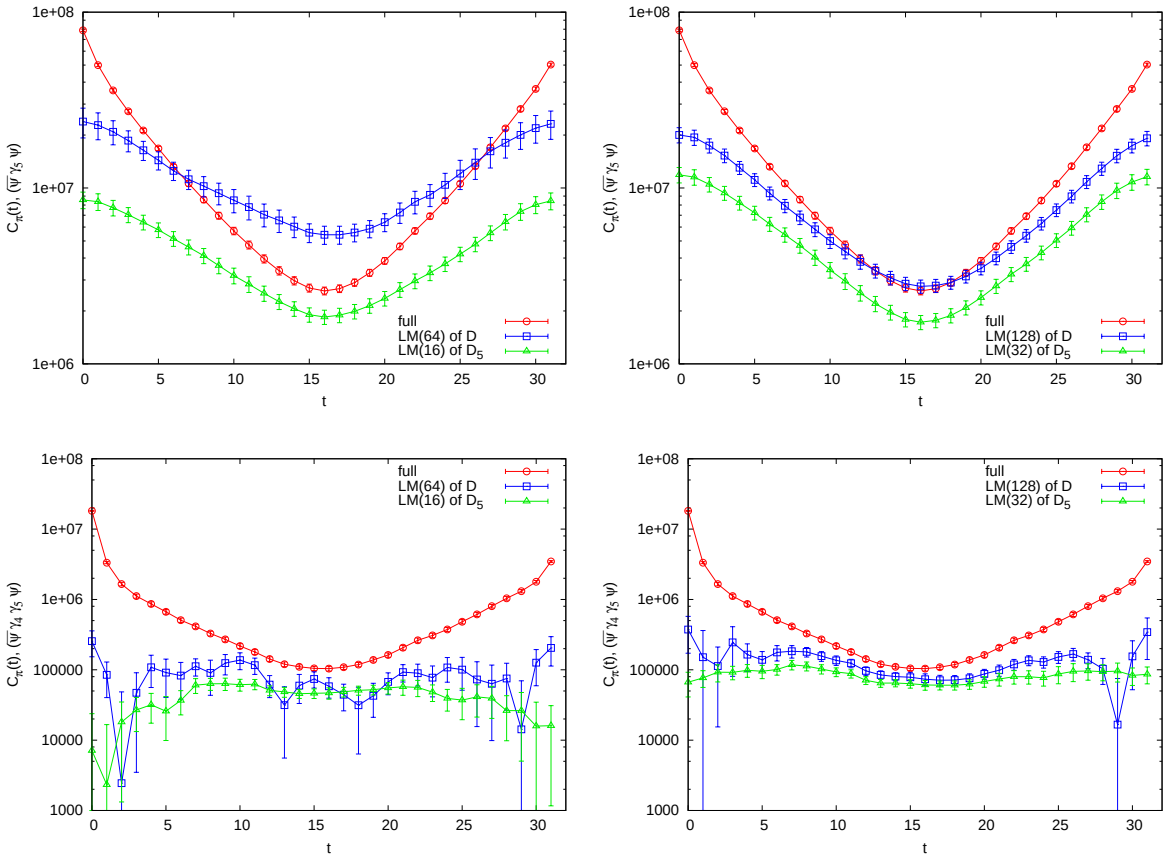

Figure A.8: Low-mode contribution to the $J^{PC} = 0^{-+}$ correlator using interpolators $\overline{\psi}\gamma_5\psi$ (top) and $\overline{\psi}\gamma_4\gamma_5\psi$ (bottom).

of D_5 in comparison to D are needed in order to obtain a similar slope of the correlators and therefore a similar effective mass of the corresponding particle. On the left hand side plots of Figs. A.8 and A.9, we use the lowest 64 modes of D but only the lowest 16 modes of D_5 and on the right hand side plots we use 128 vs. 32 low-modes of D and D_5, respectively.

Looking again at Fig. A.7, we observe that the different amounts of D and D_5 low-modes correspond to the same cutoff in terms of the real part of the spectrum. In quantitative terms the latter means that on the left hand side plots of Figs. A.8 and A.9, we allow for all eigenvalues of D and D_5 with a maximum real part of approximately 0.022 (in lattice units), and on the right hand side plots roughly 0.032.

While in Figs. A.8 and A.9 we show only the contribution of the low-modes to the pion and rho correlators, in Fig. A.10 and Fig. A.11 we now exclude the lowest modes, i.e., these correlators are built with truncated quark propagators. For the rho (Fig. A.11) we clearly obtain a linear region in the logarithmic correlator for medium times, although with slightly different

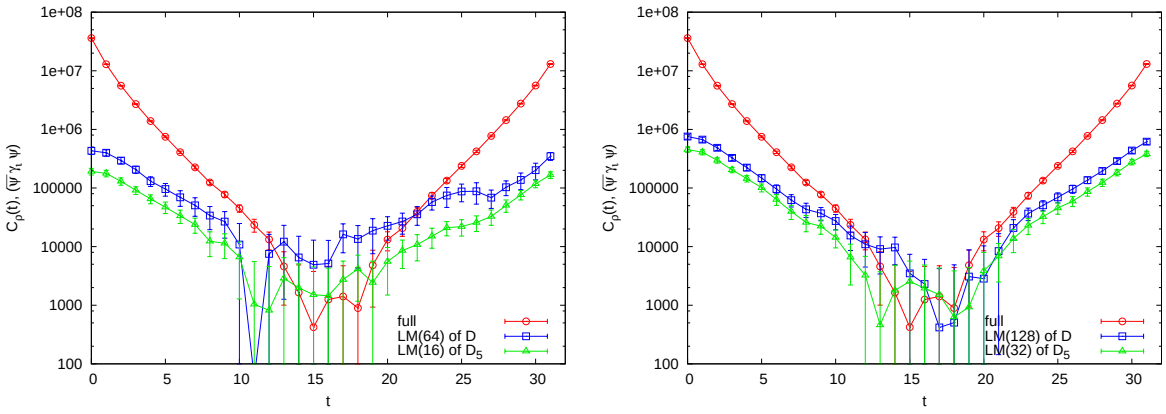

Figure A.9: Low-mode contribution to the $J^{PC} = 1^{--}$ correlator using interpolator $\overline{\psi}\gamma_i\psi$.

slopes for D and D_5. In contrast, the exponential decay of the pion from the pseudoscalar interpolator (top row of Fig. A.10) ceases when excluding the lowest eigenmodes of D_5, and even more severe when subtracting eigenmodes of D. This can be attributed to the fact that the pion, interpolated by $\overline{\psi}\gamma_5\psi$, is heavily dominated by the low-modes of the Dirac operator as demonstrated in Fig. A.8.

Another interpolator with the correct quantum numbers of the pion is the temporal part of the axial vector current $\overline{\psi}\gamma_4\gamma_5\psi$. We show the low-mode contribution of the correlator using that interpolator in the bottom row of Fig. A.8, obviously the low-modes are less dominant here. As a result, the truncated version of the pion using interpolator $\overline{\psi}\gamma_4\gamma_5\psi$ retains its exponential decay and thus manifests a clear mass plateau (bottom row of Fig. A.10).

In order to answer the question whether the lower spectrum of D or D_5 is better suited for our work, we stress that in all cases, the truncated rho correlator Fig. A.11 and the truncated pion correlators Fig. A.10, the signal from the correlator that excludes the low-modes of D_5 is much less noisy. Moreover, as we have seen in the above considerations, the real part of the spectrum plays the crucial role in saturating the correlators. As it is evident from the plot in Fig. A.7, in the case of the real part of the spectrum of D the cutoff starts to increase very slowly with the number of modes and suddenly, at the scale of the bare quark mass, it increases very fast. On the contrary, the derivative of the real part of the spectrum of D_5 is much closer to a constant as a function of the number of eigenmodes. Consequently, we decided to adopt the eigenspectrum of the hermitian Dirac operator D_5 for our study.

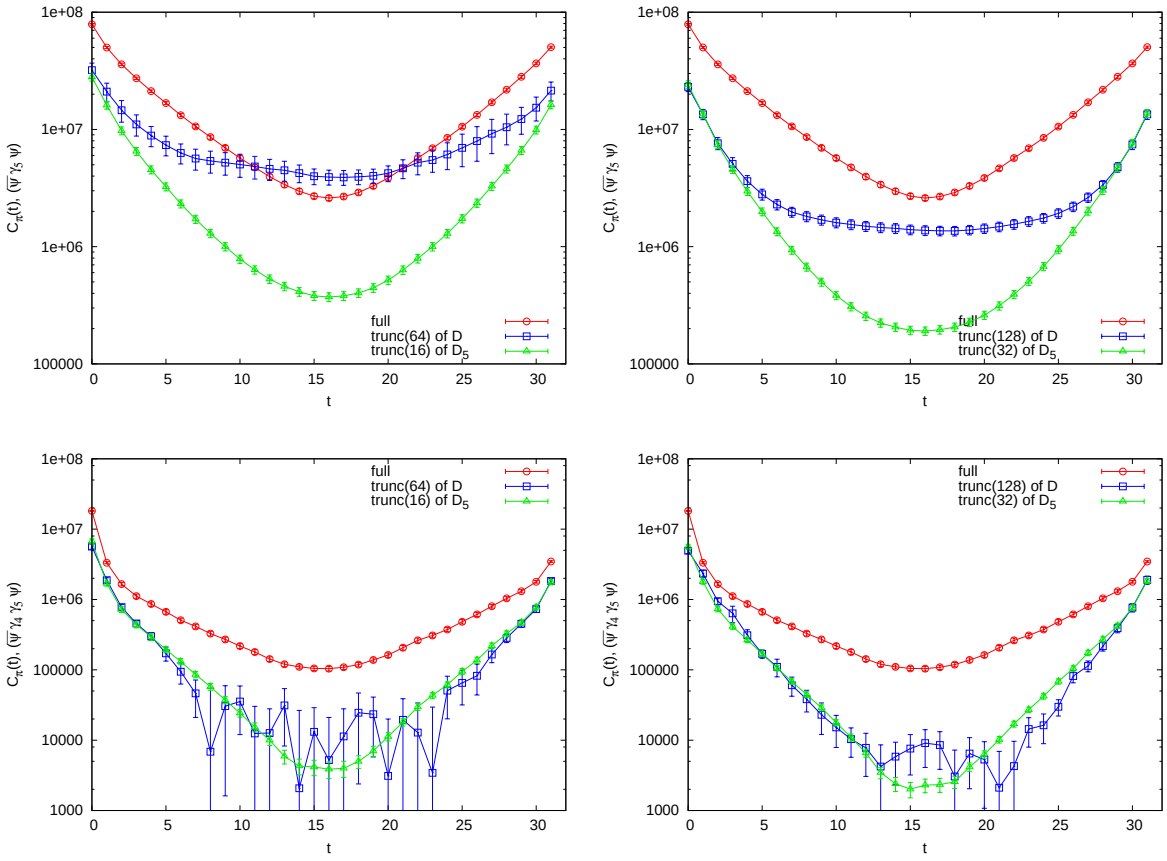

Figure A.10: Truncated $J^{PC} = 0^{-+}$ correlator using interpolator $\overline{\psi}\gamma_5\psi$ (top) and $\overline{\psi}\gamma_4\gamma_5\psi$ (bottom).

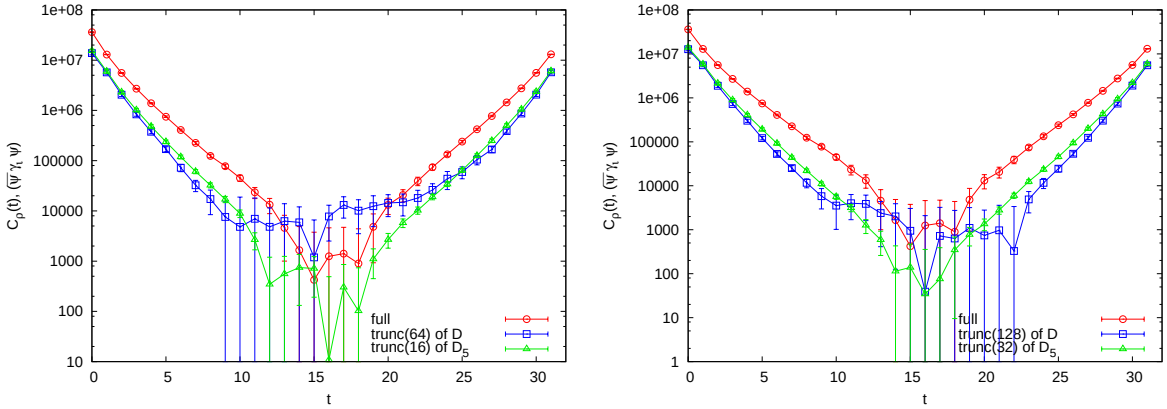

Figure A.11: Truncated $J^{PC} = 1^{--}$ correlator using interpolator $\overline{\psi}\gamma_i\psi$.

A.5 The pion correlator from zero to all Dirac eigenmodes on a small lattice

As a consistency check of our simulation and in order to better understand the convergence behavior of low/high mode correlators to the full correlators, it would be desirable to have all eigenvalues and eigenvectors of the Dirac operator on a given gauge field configuration. Since the cost in computer time and the need of memory are way to high to obtain the whole eigenspectrum for our lattices of size $16^3 \times 32$, we constrained ourselves to an affordable test case: we have calculated all 6144 eigenvalues of D and D_5 on a single quenched ($\beta = 6.0$) configuration of lattice size $4^3 \times 8$ using LAPACK. See Fig. A.12 for the complete eigenspectrum of D.

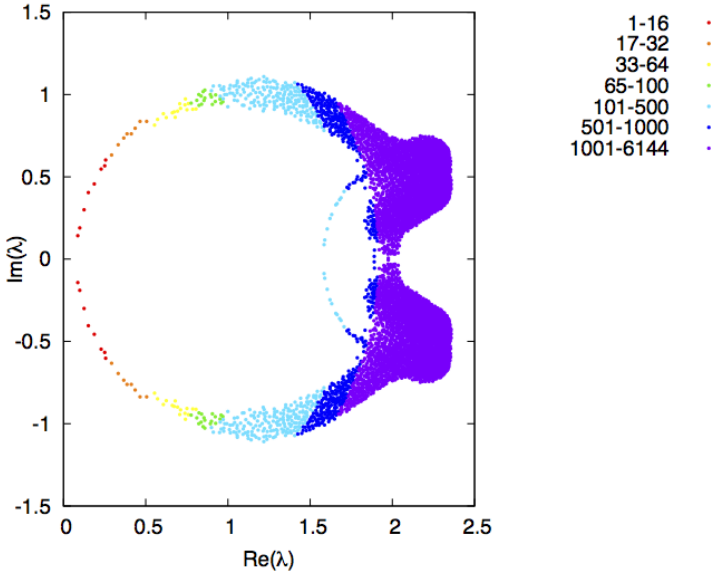

Figure A.12: All eigenvalues of the CI Dirac operator from a $4^3 \times 8$ lattice.

This allows us to build up the pion correlator mode by mode from zero to all modes. The latter can on one hand be done by gradually adding low-modes until all modes are included, see the top row of Fig. A.13 where on the left hand side we show the contributions of the lowest 2 - 6000 eigenmodes of D_5 and on the right hand side the contributions from 6000 modes up to the full case (6144 modes).

On the other hand, we can saturate the pion correlator by starting with the highest modes and piecewise adding more modes until the lowest mode is included, which is shown in the bottom row of Fig. A.13. This choice is of course equivalent to subtracting a given number of low-modes at each step, therefore we use again the notation red(k), which refers to having excluded the lowest k modes or in other words included the highest $12\,|\Lambda| - k$ modes.

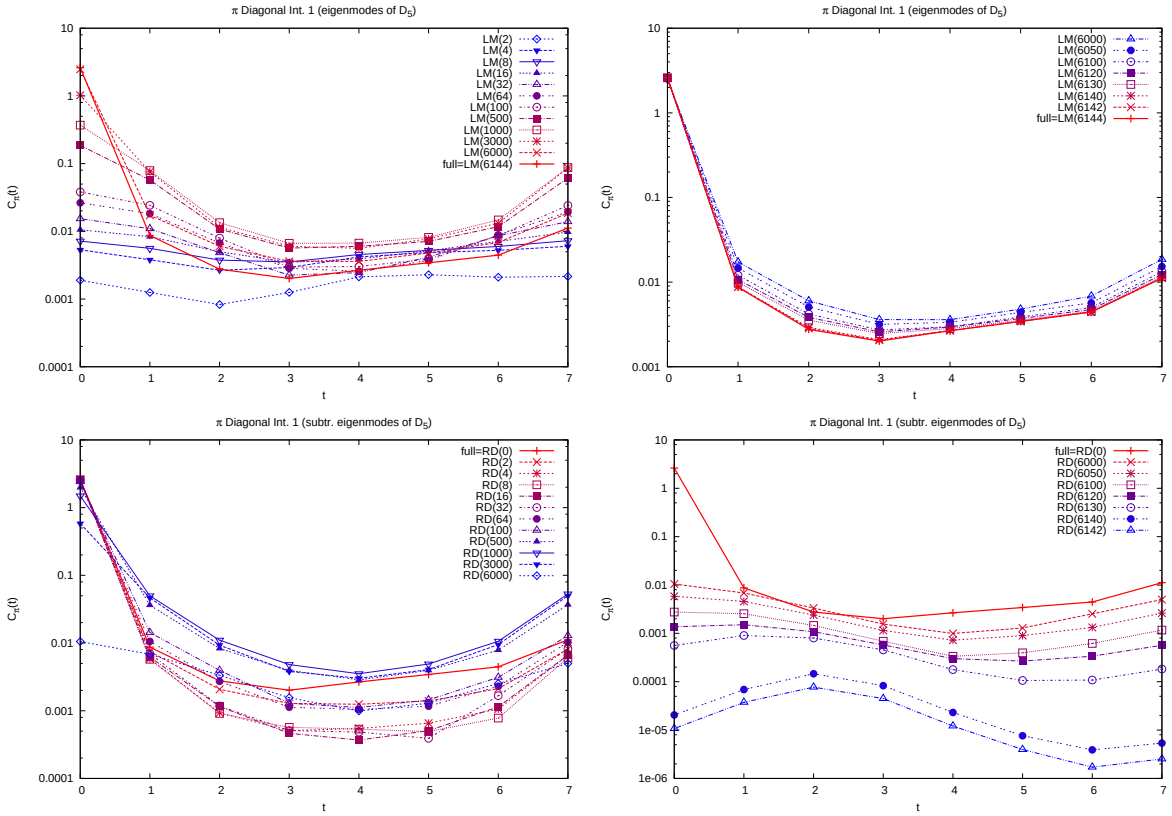

Figure A.13: The eigenmode contribution of the hermitian Dirac operator D_5 to the pion correlator from a single configuration of size $4^3 \times 8$. In the top row the contribution from $2 - 6000$ modes (left) and and from 6000 to all 6144 modes (right) is shown. The bottom row shows the contribution from all modes except the lowest $2 - 6000$ modes (left) and the highest $144 - 2$ modes only (right).

Bibliography

[1] C. B. Lang and M. Schröck, "Unbreaking chiral symmetry," *Phys. Rev. D* **84** (2011) 087704, 1107.5195 [hep-lat].
v, 25, 38, 39, 48, 49, 50, 55, 56, 57, 59, 65, 154

[2] M. Schröck, "The chirally improved quark propagator and restoration of chiral symmetry," *Phys. Lett. B* **711** (2012) 217–224, arXiv:1112.5107 [hep-lat].
v, 37, 55, 81, 123

[3] L. Y. Glozman, C. B. Lang, and M. Schröck, "Symmetries of hadrons after unbreaking the chiral symmetry," *Phys.Rev. D* **86** (2012) 014507, arXiv:1205.4887 [hep-lat].
v, 53

[4] M. Schröck and H. Vogt, "Coulomb, Landau and maximally Abelian gauge fixing in lattice QCD with multi-GPUs," *Comp. Phys. Commun.* **184** (2013) 1907–1919, arXiv:1212.5221 [hep-lat].
v, 40, 77, 123

[5] C. B. Lang and M. Schröck, "Effects of the low lying Dirac modes on the spectrum of ground state mesons," *PoS* **Lattice2011** (2011) 111, arXiv:1110.6149 [hep-lat].
v, 55, 57

[6] L. Y. Glozman, C. B. Lang, and M. Schröck, "Effects of the low lying Dirac modes on excited hadrons in lattice QCD," *Acta Phys. Polon. Supp. B* **5** (2012) 1001–1006, arXiv:1207.7323 [hep-lat].
v

[7] M. Schröck and H. Vogt, "Gauge fixing using overrelaxation and simulated annealing on GPUs," *PoS* **Lattice2012** (2012) 187, arXiv:1209.4008 [hep-lat].
v, 81, 93

[8] M. Schröck, "Chiral restoration of the momentum space quark propagator through Dirac low-mode truncation," *PoS* **ConfinementX** (2013) 080, arXiv:1301.3089 [hep-lat].

v

[9] L. Y. Glozman, "Confinement, chiral symmetry breaking and the mass generation of hadrons," *Acta Phys. Polon. Supp. B* **6** (2013) 245–250, arXiv:1211.7267 [hep-ph].
v

[10] M. Schröck and H. Vogt, "Gauge fixing in lattice QCD with multi-GPUs," arXiv:1305.3440 [hep-lat].
v

[11] H. Fritzsch, M. Gell-Mann, "Current algebra- quarks and what else?," *16. International Conference High energy physics, Cern* (1972) .
1

[12] H. Fritzsch, M. Gell-Mann, H. Leutwyler, "Advantages of the color octet gluon picture," *Physics Letters B* **47** (1973) .
1

[13] K. G. Wilson, "Confinement and quarks," *Phys. Rev. D* **10** (1974) 2445.
2, 7

[14] T. A. DeGrand and A. Hasenfratz, "Low lying fermion modes, topology and light hadrons in quenched QCD," *Phys. Rev. D* **64** (2001) 034512, arXiv:hep-lat/0012021 [hep-lat].
2, 26, 55

[15] T. DeGrand, "Short distance current correlators: Comparing lattice simulations to the instanton liquid," *Phys. Rev. D* **64** (2001) 094508, hep-lat/0106001 [hep-lat].
2, 26, 55

[16] T. A. DeGrand, "Eigenvalue decomposition of meson correlators," *Phys. Rev. D* **69** (2004) 074024, arXiv:hep-ph/0310303 [hep-ph].
2, 26, 29, 54, 55

[17] T. DeGrand and S. Schaefer, "Improving meson two-point functions in lattice QCD," *Comput. Phys. Commun.* **159** (2004) 185–191, hep-lat/0401011.
2, 26, 29, 55

[18] T. DeGrand and S. Schaefer, "Improving meson two-point functions by low-mode averaging," *Nucl. Phys. (Proc. Suppl.)* **140** (2005) 296, hep-lat/0409056.
2, 26, 55

[19] T. D. Cohen, "Effective chiral restoration in the hadronic spectrum and QCD," *Nucl.Phys.* **A775** (2006) 89–101, arXiv:hep-ph/0605206 [hep-ph].
2, 26, 54

[20] H. B. Nielsen and M. Ninomiya, "No-go theorem for regularizing chiral fermions," *Phys. Lett. B* **105** (1981) 219.
5, 15

[21] H. Nielsen and M. Ninomiya, "Absence of Neutrinos on a Lattice. (I). Proof by homotopy theory," *Nucl. Phys. B* **185** (1981) 20.
5, 15

[22] H. Nielsen and M. Ninomiya, "Absence of Neutrinos on a Lattice. (II). Intuitive topological proof," *Nucl. Phys. B* **193** (1981) 173.
5, 15

[23] K. Symanzik, "Continuum Limit and Improved Action in Lattice Theories. 1. Principles and phi**4 Theory," *Nucl. Phys. B* **226** (1983) 187.
7, 43

[24] M. Lüscher and P. Weisz, "On-shell improved lattice gauge theories," *Commun. Math. Phys.* **97** (1985) 59.
7

[25] C. Gattringer and C. B. Lang, "Pure gauge theory on the lattice," *Lect. Notes Phys.* **788** (2010) 43–71.
8

[26] C. Gattringer and C. B. Lang, "Fermions on the lattice," *Lect. Notes Phys.* **788** (2010) 103–122.
8

[27] T. Matthews and A. Salam, "The green's functions of quantized fields," *Nuovo Cim.* **12** (1954) 563.
9

[28] T. Matthews and A. Salam, "Propagators of quantized fields," *Nuovo Cim.* **2** (1955) 120.
9

[29] S. Duane, A. D. Kennedy, B. J. Pendleton, and D. Roweth, "Hybrid Monte Carlo," *Phys. Lett. B* **195** (1987) 216.
10

[30] C. Gattringer and C. B. Lang, "Hadron spectroscopy," *Lect. Notes Phys.* **788** (2010) 123–156.
10

[31] S. Güsken *et al.*, "Nonsinglet axial vector couplings of the baryon octet in lattice QCD," *Phys. Lett. B* **227** (1989) 266.

12, 28, 58

[32] C. Best, M. Göckeler, R. Horsley, E.-M. Ilgenfritz, H. Perlt, P. Rakow, A. Schäfer, G. Schierholz, A. Schiller, and S. Schramm, "Pion and Rho Structure Functions from Lattice QCD," *Phys. Rev. D* **56** (1997) 2743, arXiv:hep-lat/9703014.
12, 28, 58

[33] C. Michael, "Adjoint Sources in Lattice Gauge Theory," *Nucl. Phys. B* **259** (1985) 58.
12, 58

[34] M. Lüscher and U. Wolff, "How to calculate the Elastic Scattering Matrix in 2-Dimensional QuantumField Theories by Numerical Simulation," *Nucl. Phys. B* **339** (1990) 222.
12, 58

[35] B. Blossier, M. DellaMorte, G. von Hippel, T. Mendes, and R. Sommer, "On the generalized eigenvalue method for energies and matrix elements in lattice field theory," *JHEP* **0904** (2009) 094, 0902.1265.
12

[36] L. Y. Glozman, "Lecture on elementary particles." unpublished lecture notes.
12

[37] Y. Nambu, "Quasi-particles and gauge invariance in the theory of superconductivity,"*Phys. Rev.* **117** (Feb, 1960) 648–663. http://link.aps.org/doi/10.1103/PhysRev.117.648.
15

[38] J. Goldstone, "Field theories with «superconductor» solutions," *Il Nuovo Cimento* **19** (1961) no. 1, 154–164. http://dx.doi.org/10.1007/BF02812722.
15

[39] J. Goldstone, A. Salam, and S. Weinberg, "Broken symmetries,"*Phys. Rev.* **127** (Aug, 1962) 965–970. http://link.aps.org/doi/10.1103/PhysRev.127.965.
15

[40] C. Vafa and E. Witten, "Parity conservation in quantum chromodynamics,"*Phys. Rev. Lett.* **53** (Aug, 1984) 535–536. http://link.aps.org/doi/10.1103/PhysRevLett.53.535.
15

[41] P. H. Ginsparg and K. G. Wilson, "A Remnant of Chiral Symmetry on the Lattice," *Phys. Rev. D* **25** (1982) 2649.
15

[42] M. Lüscher, "Exact chiral symmetry on the lattice and the Ginsparg-Wilson relation," *Phys. Lett. B* **428** (1998) 342, arXiv:hep-lat/9802011.
16

[43] H. Neuberger, "Exactly massless quarks on the lattice," *Phys. Lett. B* **417** (1998) 141, arXiv:hep-lat/9707022.
16, 26, 38, 55

[44] H. Neuberger, "More about exactly massless quarks on the lattice," *Phys. Lett. B* **427** (1998) 353, arXiv:hep-lat/9801031.
16, 26, 38, 55

[45] C. Gattringer, "A new approach to Ginsparg-Wilson fermions," *Phys. Rev. D* **63** (2001) 114501, arXiv:hep-lat/0003005.
16, 28, 38, 40, 57, 129

[46] C. Gattringer, I. Hip, and C. B. Lang, "Approximate Ginsparg-Wilson fermions: A first test," *Nucl. Phys. B* **597** (2001) 451, arXiv:hep-lat/0007042.
16, 28, 38, 40, 57, 129

[47] J. Greensite, "An introduction to the confinement problem," *Lect. Notes Phys.* **821** (2011) 1–211.
16

[48] C. Gattringer and C. B. Lang, "Chiral symmetry on the lattice," *Lect. Notes Phys.* **788** (2010) 157–184.
18

[49] M. F. Atiyah and I. M. Singer, "The index of elliptic operators. 5.," *Ann. Math.* **93** (1971) 139.
18, 26, 28

[50] P. Hasenfratz, V. Laliena, and F. Niedermayer, "The index theorem in QCD with a finite cut-off," *Phys. Lett. B* **427** (1998) 125, hep-lat/9801021.
18

[51] T. Banks and A. Casher, "Chiral symmetry breaking in confining theories," *Nucl. Phys. B* **169** (1980) 103.
18, 25, 26, 28, 38, 48, 56

[52] C. B. Lang, "On the spectrum of lattice Dirac operators," in *Mathematical Physics and Stochastic Analysis, Essays in Honour of Ludwig Streit.*
World Scientific, Singapore, 1998.
hep-lat/9907017.

23

[53] T. Schäfer and E. V. Shuryak, "Instantons in QCD," *Rev. Mod. Phys.* **70** (1998) 323, hep-ph/9610451.
26, 54

[54] L. Giusti, P. Hernández, M. Laine, P. Weisz, and H. Wittig, "Low-energy couplings of QCD from current correlators near the chiral limit," *JHEP* **04** (2004) 013, hep-lat/0402002.
26, 55

[55] G. S. Bali, S. Collins, and A. Schaefer, "Effective noise reduction techniques for disconnected loops in Lattice QCD," *Comput. Phys. Commun.* **181** (2010) 1570–1583, 0910.3970.
26, 55

[56] G. Bali, L. Castagnini, and S. Collins, "Meson and baryon masses with low mode averaging," *PoS* **Lattice2010** (2010) 096, arXiv:1011.1353 [hep-lat].
26, 27, 29, 55, 56

[57] L. Y. Glozman, "SU(2)(L) x SU(2)(R) and U(1)(A) restorations high in the hadron spectrum and what it tells us about," *Phys. Lett. B* **539** (2002) 257, arXiv:hep-ph/0205072 [hep-ph].
26, 54, 66

[58] L. Y. Glozman, "Chiral multiplets of excited mesons," *Phys. Lett. B* **587** (2004) 69, arXiv:hep-ph/0312354.
26, 54, 66

[59] C. Gattringer, C. Hagen, C. B. Lang, M. Limmer, D. Mohler, and A. Schäfer, "Hadron spectroscopy with dynamical chirally improved fermions," *Phys. Rev. D* **79** (2009) 054501, arXiv:0812.1681 [hep-lat].
28, 38, 40, 41, 58, 123, 125, 129, 158

[60] **BGR [Bern-Graz-Regensburg]** Collaboration, G. P. Engel, C. B. Lang, M. Limmer, D. Mohler, and A. Schäfer, "Meson and baryon spectrum for QCD with two light dynamical quarks," *Phys. Rev. D* **82** (2010) 034505, arXiv:1005.1748 [hep-lat].
28, 29, 38, 40, 41, 58, 59

[61] R. B. Lehoucq, D. C. Sorensen, and C. Yang, *ARPACK Users' Guide: Solution of large-scale eigenvalue problems with implicitly restarted Arnoldi methods.*
SIAM, New York, 1998.
28, 59, 129

[62] M. Lüscher, "Local coherence and deflation of the low quark modes in lattice QCD," *JHEP* **07** (2007) 081, arXiv:0706.2298 [hep-lat].
29, 57

[63] L. Giusti and M. Lüscher, "Chiral symmetry breaking and the Banks–Casher relation in lattice QCD with Wilson quarks," *JHEP* **0903** (2009) 013, arXiv:0812.3638 [hep-lat].
29, 57

[64] S. Necco and A. Shindler, "Spectral density of the Hermitean Wilson Dirac operator: a NLO computation in chiral perturbation theory," *JHEP* **04** (2011) 031, arXiv:1101.1778 [hep-lat].
29, 57

[65] K. Splittorff and J. Verbaarschot, "The Wilson Dirac Spectrum for QCD with Dynamical Quarks," *Phys. Rev. D* **84** (2011) 065031, arXiv:1105.6229 [hep-lat].
29, 57

[66] L. Y. Glozman, "Restoration of chiral and $U(1)_A$ symmetries in excited hadrons," *Phys. Rep.* **444** (2007) 1, hep-ph/0701081.
30, 31, 38, 54, 66

[67] J. I. Skullerud and A. G. Williams, "Quark propagator in Landau gauge," *Phys. Rev. D* **63** (2001) 054508, arXiv:hep-lat/0007028 [hep-lat].
38, 42, 45

[68] J. Skullerud, D. B. Leinweber, and A. G. Williams, "Nonperturbative improvement and tree level correction of the quark propagator," *Phys. Rev. D* **64** (2001) 074508, arXiv:hep-lat/0102013 [hep-lat].
38, 45, 46

[69] J. B. Kogut and L. Susskind, "Hamiltonian Formulation of Wilson's Lattice Gauge Theories," *Phys. Rev. D* **11** (1975) 395.
38

[70] **MILC** Collaboration, K. Orginos, D. Touissant, and R. Sugar, "Variants of fattening and flavor symmetry restoration," *Phys. Rev. D* **60** (1999) 054503, arXiv:hep-lat/9903032.
38

[71] P. O. Bowman, U. M. Heller, and A. G. Williams, "Lattice quark propagator with staggered quarks in Landau and Laplacian gauges," *Phys. Rev. D* **66** (2002) 014505, arXiv:hep-lat/0203001 [hep-lat].
38

[72] M. B. Parappilly *et al.*, "Scaling behavior of quark propagator in full QCD," *Phys. Rev. D* **73** (2006) 054504, hep-lat/0511007.
38

[73] P. O. Bowman, U. M. Heller, and A. G. Williams, "Lattice quark propagator in Landau and Laplacian gauges," *Nucl.Phys.Proc.Suppl.* **106** (2002) 820–822, arXiv:hep-lat/0110081 [hep-lat].
38

[74] P. O. Bowman, U. M. Heller, D. B. Leinweber, and A. G. Williams, "Modeling the quark propagator," *Nucl.Phys.Proc.Suppl.* **119** (2003) 323–325, arXiv:hep-lat/0209129 [hep-lat].
38

[75] P. O. Bowman, U. M. Heller, D. B. Leinweber, M. B. Parappilly, A. G. Williams, *et al.*, "Unquenched quark propagator in Landau gauge," *Phys. Rev. D* **71** (2005) 054507, arXiv:hep-lat/0501019 [hep-lat].
38

[76] S. Furui and H. Nakajima, "Unqueched Kogut-Susskind quark propagator in lattice Landau gauge QCD," arXiv:hep-lat/0511045 [hep-lat].
38

[77] **CSSM Lattice collaboration** Collaboration, F. D. Bonnet, P. O. Bowman, D. B. Leinweber, A. G. Williams, and J.-b. Zhang, "Overlap quark propagator in Landau gauge," *Phys. Rev. D* **65** (2002) 114503, arXiv:hep-lat/0202003 [hep-lat].
38, 47

[78] **CSSM Lattice collaboration** Collaboration, J. Zhang, P. O. Bowman, D. B. Leinweber, A. G. Williams, and F. D. Bonnet, "Scaling behavior of the overlap quark propagator in Landau gauge," *Phys. Rev. D* **70** (2004) 034505, arXiv:hep-lat/0301018 [hep-lat].
38, 47

[79] J. Zhang, P. O. Bowman, R. J. Coad, U. M. Heller, D. B. Leinweber, *et al.*, "Quark propagator in Landau and Laplacian gauges with overlap fermions," *Phys. Rev. D* **71** (2005) 014501, arXiv:hep-lat/0410045 [hep-lat].
38, 47

[80] W. Kamleh, P. O. Bowman, D. B. Leinweber, A. G. Williams, and J. Zhang, "The fat link irrelevant clover overlap quark propagator," *Phys. Rev. D* **71** (2005) 094507, arXiv:hep-lat/0412022 [hep-lat].
38, 47

[81] W. Kamleh, P. O. Bowman, D. B. Leinweber, A. G. Williams, and J. Zhang, "Unquenching effects in the quark and gluon propagator," *Phys. Rev. D* **76** (2007) 094501, arXiv:0705.4129 [hep-lat].
38, 47

[82] P. O. Bowman, U. M. Heller, D. B. Leinweber, A. G. Williams, and J. B. Zhang, "Quark propagator from LQCD and its physical implications," *Lect. Notes Phys.* **663** (2005) 17–63.
38, 47

[83] P. O. Bowman, U. M. Heller, D. B. Leinweber, A. G. Williams, and J.-b. Zhang, "Infrared and ultraviolet properties of the Landau gauge quark propagator," *Nucl. Phys. Proc. Suppl.* **128** (2004) 23–29, arXiv:hep-lat/0403002.
38, 47

[84] H. Suganuma, S. Gongyo, T. Iritani, and A. Yamamoto, "Relevant Gluonic Momentum for Confinement and Gauge-Invariant Formalism with Dirac-mode Expansion," *PoS* **QCD-TNT-II** (2011) 044, arXiv:1112.1962 [hep-lat].
38, 55

[85] L. Giusti, M. Paciello, C. Parrinello, S. Petrarca, and B. Taglienti, "Problems on lattice gauge fixing," *Int. J. Mod. Phys. A* **16** (2001) 3487–3534, arXiv:hep-lat/0104012 [hep-lat].
40, 81

[86] C. Gattringer, M. Göckeler, P. Hasenfratz, S. Hauswirth, K. Holland, T. Jörg, K. J. Juge, C. B. Lang, F. Niedermayer, P. E. L. Rakow, S. Schaefer, and A. Schäfer, "Quenched spectroscopy with fixed-point and chirally improved fermions," *Nucl. Phys. B* **677** (2004) 3, arXiv:hep-lat/0307013.
40

[87] C. B. Lang, P. Majumdar, and W. Ortner, "QCD with two dynamical flavors of chirally improved quarks," *Phys. Rev. D* **73** (2006) 034507, arXiv:hep-lat/0512014.
40

[88] G. P. Engel, C. B. Lang, M. Limmer, D. Mohler, and A. Schäfer, "QCD with two light dynamical chirally improved quarks: Mesons," *Phys. Rev. D* **85** (2012) 034508, arXiv:1112.1601 [hep-lat].
40, 59, 61, 64, 157

[89] C. Gattringer, M. Göckeler, P. Huber, and C. B. Lang, "Renormalization of bilinear quark operators for the chirally improved lattice Dirac operator," *Nucl. Phys. B* **694** (2004) 170, hep-lat/0404006.

40

[90] P. Huber, "Renormalization factors of quark bilinears using the DCI operator with dynamical quarks," *JHEP* **11** (2010) 107, arXiv:1003.3496 [hep-lat].
40

[91] B. Sheikholeslami and R. Wohlert *Nucl. Phys. B* **259** (1985) 572.
41

[92] J. I. Skullerud and A. G. Williams, "The Quark propagator in momentum space," *Nucl.Phys.Proc.Suppl.* **83** (2000) 209–211, arXiv:hep-lat/9909142 [hep-lat].
42

[93] R. Alkofer and L. von Smekal, "The Infrared behavior of QCD Green's functions: Confinement dynamical symmetry breaking, and hadrons as relativistic bound states," *Phys.Rept.* **353** (2001) 281, arXiv:hep-ph/0007355 [hep-ph].
43

[94] M. Lüscher, S. Sint, R. Sommer, and P. Weisz, "Chiral symmetry and O(a) improvement in lattice QCD," *Nucl. Phys. B* **478** (1996) 365–400, arXiv:hep-lat/9605038 [hep-lat].
44

[95] B. Sheikholeslami and R. Wohlert, "Improved Continuum Limit Lattice Action for QCD with Wilson Fermions," *Nucl. Phys. B* **259** (1985) 572.
44

[96] G. Heatlie, G. Martinelli, C. Pittori, G. Rossi, and C. T. Sachrajda, "The improvement of hadronic matrix elements in lattice QCD," *Nucl. Phys. B* **352** (1991) 266–288.
44

[97] C. Dawson, G. Martinelli, G. Rossi, C. T. Sachrajda, S. R. Sharpe, *et al.*, "Nonperturbative improvement of operators with Wilson fermions," *Nucl.Phys.Proc.Suppl.* **63** (1998) 877–879, arXiv:hep-lat/9710027 [hep-lat].
45

[98] L. Y. Glozman, "Parity doublets and chiral symmetry restoration in baryon spectrum," *Phys. Lett. B* **475** (2000) 329–334, arXiv:hep-ph/9908207.
54

[99] T. D. Cohen and L. Y. Glozman, "Chiral multiplets versus parity doublets in highly excited baryons," *Phys. Rev. D* **65** (2001) 016006, arXiv:hep-ph/0102206.
54, 66

[100] T. D. Cohen and L. Y. Glozman, "Does one observe chiral symmetry restoration in baryon spectrum?," *Int. J. Mod. Phys.* **A17** (2002) 1327–1354, arXiv:hep-ph/0201242.
54, 66

[101] R. L. Jaffe, D. Pirjol, and A. Scardicchio, "Pion decoupling and SU(2)L x SU(2)R restoration in the hadron spectrum," *Phys. Rev. D* **74** (2006) 057901.
54

[102] R. L. Jaffe, D. Pirjol, and A. Scardicchio, "Why massless pions preclude SU(2)L x SU(2)R restoration in the hadron spectrum," *Phys. Rev. Lett.* **96** (2006) 121601, arXiv:hep-ph/0511081.
54

[103] R. L. Jaffe, D. Pirjol, and A. Scardicchio, "Parity doubling among the baryons," *Phys. Rept.* **435** (2006) 157, arXiv:hep-ph/0602010.
54

[104] M. Shifman and A. Vainshtein, "Highly Excited Mesons, Linear Regge Trajectories and the Pattern of the Chiral Symmetry Realization," *Phys. Rev. D* **77** (2008) 034002, arXiv:0710.0863 [hep-ph].
54

[105] A. Anisovich, E. Klempt, V. Nikonov, A. Sarantsev, H. Schmieden, *et al.*, "Evidence for a negative-parity spin-doublet of nucleon resonances at 1.88 GeV," *Phys. Lett. B* **711** (2012) 162, arXiv:1111.6151 [nucl-ex].
54

[106] H. Neff, N. Eicker, T. Lippert, J. W. Negele, and K. Schilling, "On the low fermionic eigenmode dominance in QCD on the lattice," *Phys.Rev.* **D64** (2001) 114509, arXiv:hep-lat/0106016 [hep-lat].
55

[107] S. Gongyo, T. Iritani, and H. Suganuma, "Gauge-Invariant Formalism with a Dirac-mode Expansion for Confinement and Chiral Symmetry Breaking," *Phys. Rev. D* **86** (2012) 034510, arXiv:1202.4130 [hep-lat].
55

[108] G. E. Brown and M. Rho, "Scaling effective Lagrangians in a dense medium," *Phys. Rev. Lett.* **66** (1991) 2720.
55

[109] L. Y. Glozman and R. F. Wagenbrunn, "Chirally symmetric but confining dense and cold matter," *Phys. Rev. D* **77** (2008) 054027, arXiv:0709.3080 [hep-ph].

55

[110] L. Y. Glozman, "Infrared stability of quarkyonic matter with the $1/p^4$ confinement," *Phys. Rev. D* **79** (2009) 037504, arXiv:0812.1101 [hep-ph].
55

[111] L. Y. Glozman, "Confined but chirally symmetric hadrons at large density and the Casher's argument," *Phys. Rev. D* **80** (2009) 037701, arXiv:0907.1473 [hep-ph].
55

[112] L. Y. Glozman, V. K. Sazonov, and R. F. Wagenbrunn, "Chirally symmetric and confining dense matter with a diffused quark Fermi surface," *Phys. Rev. D* **84** (2011) 095009, arXiv:1108.1681 [hep-ph].
55

[113] J. Osborn and J. Verbaarschot, "Thouless energy and correlations of QCD Dirac eigenvalues," *Phys. Rev. Lett.* **81** (1998) 268–271, arXiv:hep-ph/9807490 [hep-ph].
56

[114] T. Burch, C. Gattringer, L. Y. Glozman, R. Kleindl, C. B. Lang, and A. Schäfer, "Spatially improved operators for excited hadrons on the lattice," *Phys. Rev. D* **70** (2004) 054502, arXiv:hep-lat/0405006.
58

[115] C. Gattringer, L. Y. Glozman, C. B. Lang, D. Mohler, and S. Prelovsek, "Derivative sources in lattice spectroscopy of excited mesons," *Phys. Rev. D* **78** (2008) 034501, arXiv:0802.2020 [hep-lat].
59

[116] A. De Rujula, H. Georgi, and S. L. Glashow, "Hadron Masses in a Gauge Theory," *Phys. Rev. D* **12** (1975) 147.
72

[117] N. Isgur and G. Karl, "P Wave Baryons in the Quark Model," *Phys. Rev. D* **18** (1978) 4187.
72

[118] L. Y. Glozman and D. O. Riska, "The Spectrum of the nucleons and the strange hyperons and chiral dynamics," *Phys. Rept.* **268** (1996) 263, arXiv:hep-ph/9505422.
72

[119] H. Neuberger, "Nonperturbative BRS Invariance and the Gribov Problem," *Phys. Lett. B* **183** (1987) 337.
79

[120] L. von Smekal, D. Mehta, A. Sternbeck, and A. G. Williams, "Modified Lattice Landau Gauge," *PoS* **Lattice2007** (2007) 382, arXiv:0710.2410 [hep-lat].
79

[121] L. von Smekal, A. Jorkowski, D. Mehta, and A. Sternbeck, "Lattice Landau gauge via Stereographic Projection," *PoS* **Confinement8** (2008) 048, arXiv:0812.2992 [hep-th].
79

[122] S. Catterall, R. Galvez, A. Joseph, and D. Mehta, "On the sign problem in 2D lattice super Yang-Mills," *JHEP* **1201** (2012) 108, arXiv:1112.3588 [hep-lat].
80

[123] D. Mehta, S. Catterall, R. Galvez, and A. Joseph, "Supersymmetric gauge theories on the lattice: Pfaffian phases and the Neuberger 0/0 problem," *PoS* **Lattice2011** (2011) 078, arXiv:1112.5413 [hep-lat].
80

[124] D. Zwanziger, "Renormalization in the Coulomb gauge and order parameter for confinement in QCD," *Nucl. Phys. B* **518** (1998) 237–272.
80

[125] S. Kirkpatrick, C. D. Gelatt Jr., and M. P. Vecchi, "Optimization by Simulated Annealing," *Science* **330** (1983) 671.
80, 86

[126] G. Bali, V. Bornyakov, M. Müller-Preussker, and K. Schilling, "Dual superconductor scenario of confinement: A Systematic study of Gribov copy effects," *Phys. Rev. D* **54** (1996) 2863–2875, arXiv:hep-lat/9603012 [hep-lat].
80

[127] D. Mehta and M. Kastner, "Stationary point analysis of the one-dimensional lattice Landau gauge fixing functional, aka random phase XY Hamiltonian," *Annals Phys.* **326** (2011) 1425–1440, arXiv:1010.5335 [cond-mat.stat-mech].
80

[128] D. Mehta, A. Sternbeck, L. von Smekal, and A. G. Williams, "Lattice Landau Gauge and Algebraic Geometry," *PoS* **QCD-TNT09** (2009) 025, arXiv:0912.0450 [hep-lat].
80

[129] C. Hughes, D. Mehta, and J.-I. Skullerud, "Enumerating Gribov copies on the lattice," *Annals Phys.* **331** (2013) 188–215, arXiv:1203.4847 [hep-lat].
80

[130] D. Mehta, "Finding All the Stationary Points of a Potential Energy Landscape via Numerical Polynomial Homotopy Continuation Method," *Phys. Rev. E* **84** (2011) 025702, arXiv:1104.5497 [cond-mat.stat-mech].
80

[131] D. Mehta, "Numerical Polynomial Homotopy Continuation Method and String Vacua," *Adv.High Energy Phys.* **2011** (2011) 263937, arXiv:1108.1201 [hep-th].
80

[132] D. Mehta, Y.-H. He, and J. D. Hauenstein, "Numerical Algebraic Geometry: A New Perspective on String and Gauge Theories," *JHEP* **1207** (2012) 018, arXiv:1203.4235 [hep-th].
80

[133] J. E. Mandula and M. Ogilvie, "The Gluon Is Massive: A Lattice Calculation of the Gluon Propagator in the Landau Gauge," *Phys. Lett. B* **185** (1987) 127–132.
80

[134] J. E. Mandula and M. Ogilvie, "Efficient gauge fixing via overrelaxation," *Phys. Lett. B* **248** (1990) 156–158.
80, 86

[135] P. de Forcrand, "Multigrid techniques for quark propagator," *Nucl.Phys.Proc.Suppl.* **9** (1989) 516–520.
80

[136] M. A. Clark, R. Babich, K. Barros, R. C. Brower, and C. Rebbi, "Solving Lattice QCD systems of equations using mixed precision solvers on GPUs," *Comput. Phys. Commun.* **181** (2010) 1517–1528, arXiv:0911.3191 [hep-lat].
81, 90

[137] A. Alexandru, C. Pelissier, B. Gamari, and F. Lee, "Multi-mass solvers for lattice QCD on GPUs," *J.Comput.Phys.* **231** (2012) 1866–1878, arXiv:1103.5103 [hep-lat].
81

[138] N. Cardoso, P. J. Silva, P. Bicudo, and O. Oliveira, "Landau Gauge Fixing on GPUs," *Comput.Phys.Commun.* **184** (2013) 124–129, arXiv:1206.0675 [hep-lat].
81, 91

[139] J. Stack, W. Tucker, and R. Wensley, "The maximal abelian gauge, monopoles, and vortices in SU(3) lattice gauge theory," *Nucl. Phys. B* **639** (2002) 203–222.
83, 86

[140] N. Cabibbo and E. Marinari, "A New Method for Updating SU(N) Matrices in Computer

Simulations of Gauge Theories," *Phys. Lett. B* **119** (1982) 387. http://www.slac.stanford.edu/spires/find/hep/www?j=PHLTA,B119,387.
84

[141] J. K. Salmon, M. A. Moraes, R. O. Dror, and D. E. Shaw, "Parallel random numbers: as easy as 1, 2, 3," in *Proceedings of 2011 International Conference for High Performance Computing, Networking, Storage and Analysis*, SC '11, pp. 16:1–16:12. ACM, New York, NY, USA, 2011.
87

[142] P. De Forcrand, D. Lellouch, and C. Roiesnel, "Optimizing a lattice QCD simulation program," *J.Comput.Phys.* **59** (1985) 324–330.
90

[143] **FermiQCD** Collaboration, M. Di Pierro *et al.*, "www.fermiqcd.net," *Nucl. Phys. Proc. Suppl.* **129** (2004) 832–834, arXiv:hep-lat/0311027.
102

[144] I. Horvath, "Ginsparg-Wilson relation and ultralocality," *Phys.Rev.Lett.* **81** (1998) 4063–4066, arXiv:hep-lat/9808002 [hep-lat].
107

[145] P. Hernandez, K. Jansen, and M. Luscher, "Locality properties of Neuberger's lattice Dirac operator," *Nucl. Phys. B* **552** (1999) 363–378, arXiv:hep-lat/9808010 [hep-lat].
107

[146] M. C. Birse, T. D. Cohen, and J. A. McGovern, "U(1)-A symmetry and correlation functions in the high temperature phase of QCD," *Phys. Lett. B* **388** (1996) 137–140, arXiv:hep-ph/9608255 [hep-ph].
120

[147] S. H. Lee and T. Hatsuda, "U-a(1) symmetry restoration in QCD with N(f) flavors," *Phys. Rev. D* **54** (1996) 1871–1873, arXiv:hep-ph/9601373 [hep-ph].
120

[148] N. J. Evans, S. D. Hsu, and M. Schwetz, "Topological charge and U(1)-A symmetry in the high temperature phase of QCD," *Phys. Lett. B* **375** (1996) 262–266, arXiv:hep-ph/9601361 [hep-ph].
120

[149] G. Cossu, S. Aoki, H. Fukaya, S. Hashimoto, T. Kaneko, *et al.*, "Finite temperature study of the axial U(1) symmetry on the lattice with overlap fermion formulation," arXiv:1304.6145 [hep-lat].

122

[150] Z. Lin, "The QCD Phase Transition Region with Domain Wall Quarks," *AIP Conf.Proc.* **1441** (2012) 904–906, arXiv:1110.6870 [hep-lat].
122

[151] H. Ohno, U. Heller, F. Karsch, and S. Mukherjee, "Eigenvalue distribution of the Dirac operator at finite temperature with (2+1)-flavor dynamical quarks using the HISQ action," *PoS* **Lattice2011** (2011) 210, arXiv:1111.1939 [hep-lat].
122

Lists

List of Figures

List of Tables

Acknowledgments

Many thanks are due to my advisor Prof. Christian B. Lang: firstly, for this very exciting research project, but most importantly for always rendering assistance and giving advice when necessary, while at the same time leaving me the freedom to develop my own ideas.

I am very grateful to Prof. Mike Peardon for hosting me at the Trinity College Dublin during Spring 2012 and especially for helping me out as external referee for this thesis.

I express gratitude to all my collaborators, in particular, Christian Lang, Leonid Glozman, Hannes Vogt, Giuseppe Burgio, Markus Pak and Mikhail Denissenya and, moreover, to Georg Engel and Markus Limmer who helped me a lot getting started with my thesis' project. The very enlightening discussion with Prof. Pedro Bicudo in Schladming 2013 deserves special thanks. I want to acknowledge the computer related assistance by Martin Volk and Ursula Winkler. Thank you, Claudia Spidla, for the help with all the bureaucracy.

Furthermore, thanks to all my past and current colleagues in Graz for interesting discussions and for the nice and warm working atmosphere.

I thank STRONGnet for the funding and my colleagues and friends from STRONGnet for the joint trips to various conferences and workshops.